

---

FOUR-DIMENSIONAL VARIATIONAL ASSIMILATION  
OF AEROSOL DATA FROM IN-SITU AND  
REMOTE SENSING PLATFORMS

---

I N A U G U R A L – D I S S E R T A T I O N  
ZUR  
ERLANGUNG DES DOKTORGRADES  
DER MATHEMATISCH-NATURWISSENSCHAFTLICHEN FAKULTÄT  
DER UNIVERSITÄT ZU KÖLN

vorgelegt von

Lars Peter Nieradzik

aus Siegen

KÖLN, 2011

Berichterstatter: Prof. Dr. Dr. h.c. A. Ebel  
Prof. Dr. A. Wahner

Tag der letzten mündlichen Prüfung: 18.10.2011

---

## Abstract

Aerosol data assimilation is mainly restricted to the ingestion of particulate matter measurements up to  $10\ \mu\text{m}$  particle size or aerosol optical depths. The chemistry transport model EURAD-IM of the Rhenish Institute of Environmental Research (RIU) containing a sophisticated 4D-var assimilation scheme for gas-phase constituents has been expanded by a partial adjoint of the aerosol module MADE to enable the assimilation of species resolved aerosols data in space and time. To set the stage for four dimensional aerosol data assimilation, the I/O-mapping technique HDMR (High Dimensional Model Representation) had been applied to replace the computationally demanding chemistry mechanism for secondary inorganic aerosols within MADE. An adjoint of the HDMR was constructed and the inverse transport was ensured to allow the optimisation of aerosol initial values. Furthermore, several observation operators and their respective adjoints were built to make the processing of various types of measurements feasible. This set of operators includes integrators for in-situ measured  $PM_x$  as well as particle number densities. Within the scope of the AERO-SAM project a radiative transfer model, part of a satellite retrieval system SYNAER, was implemented. Its prominent feature is to provide type resolved aerosol optical thicknesses. With construction and implementation of the adjoint radiative transfer model, EURAD-IM is able to assimilate species resolved aerosol information. The newly formed aerosol assimilation scheme has been applied to two dedicated episodes. First, July of 2003 was selected when an enduring high pressure area lasted over Europe. The very dry period allowed excessive aerosol concentrations in the troposphere. This particular timeframe was taken to evaluate the functionality of the aerosol assimilation system and to validate the benefit of assimilating  $PM_{10}$  and especially species resolved satellite retrievals. Further, the airborne measurement campaign ZEPTEP-2 in autumn 2008 was chosen. A Zeppelin equipped with a condensation particle counter (CPC) delivered particle number densities with high spatial and temporal resolution. Here, the focus was set on the validation of the assimilation system of particle number densities and its performance on high resolved grids. In both cases initial value optimisation has been conducted and performance of the assimilation system and its impact on the forecast have been investigated. The studies demonstrate a considerable improvement of the forecast quality regardless of grid resolution. Moreover, making use of aerosol type resolved retrievals and particle number densities adds valuable information on the aerosol properties to the model.

## Kurzzusammenfassung

Die Assimilation von Aerosoldaten war bisher im Wesentlichen auf die Verwendung von Messungen der Gesamtmassenkonzentrationen von Partikeln bis zu einer bestimmten Größe und Messungen von optischer Tiefe beschränkt. Das Chemie-Transport-Modell EURAD-IM des Rheinischen Instituts für Umweltforschung (RIU) enthält ein hochentwickeltes vierdimensionales variationales (4D-var) Assimilationssystem für Gasphasenspezies, das nun um eine teilweise adjungierte Version des Aerosol-modells MADE erweitert wurde, um spezieaufgelöste Aerosolmessungen assimilieren zu können. Vorbereitend wurde bereits der äusserst rechenzeitaufwendige Mechanismus zur Lösung der Chemie der sekundären anorganischen Aerosole innerhalb des MADE mithilfe eines I/O-mapping-Verfahrens ersetzt. Der resultierende Algorithmus wurde nun adjungiert und die Funktionalität des adjungierten Aerosoltransportes sichergestellt. Desweiteren wurden verschiedene Beobachtungsoperatoren entwickelt und gleichzeitig adjungiert. Dazu gehören Integrationsroutinen für Massenkonzentrationen und Anzahldichten. Im Rahmen des AERO-SAM Projektes wurde ein Strahlungstransportmodell, Teil eines Satelliten-Retrieval-Systems, in das Modell eingebaut. Die Besonderheit liegt darin, dass das Modell spezieaufgelöste aerosoloptische Tiefen liefert. Das so konstruierte Aerosolassimilationssystem ist auf zwei Episoden angewandt worden. Als erstes auf den Sommer 2003, als ein langanhaltendes Hochdruckgebiet über Europa lag. Diese Wetterlage begünstigte Waldbrände und brachte stark erhöhte Feinstaubbelastung mit sich. In diesem Zeitraum wurde das neue Assimilationssystem getestet und der Nutzen der Assimilation von  $PM_{10}$  insbesondere von spezieaufgelösten Satellitendaten untersucht. Außerdem wurde die ZEPTER-2 Messkampagne aus dem Herbst 2008 ausgewählt. Ein zur Messplattform umgebauter Zeppelin, der mit einem CPC (Condensation Particle Counter) ausgestattet war, hat räumlich und zeitlich hochaufgelöste Partikelanzahldichten gemessen. In dieser Episode wurde der Fokus auf die Assimilation der Anzahldichten sowie der Leistung des Systems auf Modellgittern mit hoher Auflösung gerichtet. In beiden Fällen wurde Anfangswertoptimierung durchgeführt und das System selbst, sowie das Vermögen, die Vorhersage von Aerosolen zu verbessern, untersucht. Es hat sich herausgestellt, dass sich durch Assimilation von Aerosolen eine deutliche Verbesserung der Vorhersage insgesamt erzielen lässt, während durch die Assimilation spezieaufgelöster Retrievals zusätzlich die Zusammensetzung der Aerosole angepasst werden kann.

---

# Contents

---

|          |  |           |
|----------|--|-----------|
| <b>1</b> | <b>Introduction</b>  | <b>1</b>  |
| <b>2</b> | <b>Data Assimilation</b>                                     | <b>5</b>  |
| 2.1      | Bayes' Probability . . . . .                                 | 6         |
| 2.2      | Maximum Likelihood and Minimum Variance . . . . .            | 6         |
| 2.3      | Variational data assimilation . . . . .                      | 8         |
| 2.4      | 4-dimensional variational data assimilation . . . . .        | 8         |
| 2.5      | Kalman Filtering . . . . .                                   | 10        |
| 2.6      | Summary . . . . .  | 11        |
| <b>3</b> | <b>The model system EURAD-IM</b>                             | <b>13</b> |
| 3.1      | The EURAD-CTM . . . . .                                      | 15        |
| 3.1.1    | Functional principle . . . . .                               | 15        |
| 3.1.2    | Grid specifications . . . . .                                | 17        |
| 3.1.3    | Initialisation . . . . .                                     | 18        |
| 3.2      | The aerosol model MADE . . . . .                             | 18        |
| 3.2.1    | Size distribution . . . . .                                  | 20        |
| 3.2.2    | Aerosol dynamics . . . . .                                   | 21        |
| 3.2.3    | Aerosol chemistry . . . . .                                  | 23        |
| 3.2.4    | Emissions . . . . .  | 24        |
| 3.2.5    | Adjoint chemistry for secondary inorganic aerosols . . . . . | 24        |

---

|          |   |           |
|----------|---|-----------|
| 3.3      | Nesting . . . . .   | 27        |
| 3.4      | Observation operators . . . . .                           | 28        |
| 3.4.1    | Size integrated observations . . . . .                    | 29        |
| 3.4.2    | SYNAER - SYNergetic AErosol Retrieval . . . . .           | 31        |
| <b>4</b> | <b>Background Error Covariance Modeling</b>               | <b>39</b> |
| 4.1      | Processing of Background Error Covariances . . . . .      | 40        |
| 4.1.1    | The incremental formulation of the costfunction . . . . . | 40        |
| 4.1.2    | The diffusion approach . . . . .                          | 41        |
| 4.2      | Obtaining B . . . . .                                     | 42        |
| 4.2.1    | Isotropic and homogeneous . . . . .                       | 42        |
| 4.2.2    | Ensemble calculations . . . . .                           | 43        |
| 4.2.3    | The NMC - method . . . . .                                | 43        |
| 4.3      | Current setup . . . . .                                   | 45        |
| <b>5</b> | <b>Episode and Campaign Simulations</b>                   | <b>47</b> |
| 5.1      | July 2003 . . . . .                                       | 48        |
| 5.1.1    | Episode configuration . . . . .                           | 49        |
| 5.1.2    | Assimilation performance . . . . .                        | 51        |
| 5.1.3    | Forecast performance . . . . .                            | 54        |
| 5.1.4    | Optimised Initial Values . . . . .                        | 61        |
| 5.1.5    | Summary . . . . .   | 66        |
| 5.2      | ZEPTEr-2 Campaign 2008 . . . . .                          | 68        |
| 5.2.1    | Model configuration . . . . .                             | 70        |
| 5.2.2    | Assimilation configuration . . . . .                      | 70        |
| 5.2.3    | Available observations . . . . .                          | 72        |
| 5.2.4    | Assimilation performance . . . . .                        | 74        |
| 5.2.5    | Forecast performance . . . . .                            | 78        |
| 5.2.6    | Optimised Particle Number Densities . . . . .             | 82        |
| 5.2.7    | Summary . . . . .   | 86        |
| <b>6</b> | <b>Conclusions and Outlook</b>                            | <b>87</b> |
| <b>A</b> | <b>Vertical Grid Structure</b>                            | <b>91</b> |
| <b>B</b> | <b>Available ZEPTEr-2 Measurements</b>                    | <b>93</b> |

---

|                           |            |
|---------------------------|------------|
| <b>C ZEPTEP-2 Flights</b> | <b>97</b>  |
| <b>Bibliography</b>       | <b>109</b> |
| <b>Acknowledgements</b>   | <b>117</b> |



---

## List of Figures

---

|      |   |    |
|------|---|----|
| 3.1  | Schematic survey of the EURAD-IM model system . . . . .                                       | 14 |
| 3.2  | Schematic survey of the MADE . . . . .  | 19 |
| 3.3  | Log-normal distribution of number and volume density . . . . .                                | 30 |
| 3.4  | Footprint-H-Operator . . . . .  | 37 |
| 4.1  | Schematic overview of the NMC method . . . . .  | 44 |
| 4.2  | Horizontal diffusion coefficients for $PM_{10}$ . . . . .                                     | 45 |
| 5.1  | MODIS thermal anomalies July 2003 . . . . .   | 48 |
| 5.2  | Schematic overview of model runs . . . . .  | 50 |
| 5.3  | Available Measurements July 2003 . . . . .  | 53 |
| 5.4  | Specieswise minimisation performance July 2003 . . . . .                                      | 55 |
| 5.5  | Relative reduction of total costs 2003 . . . . .  | 56 |
| 5.6  | Overall relative cost reduction 2003 . . . . .  | 57 |
| 5.7  | Specieswise daily forecast performance July 2003 . . . . .                                    | 58 |
| 5.8  | In-situ $PM_{10}$ Bias and RMSE 2003 . . . . .  | 59 |
| 5.9  | Error statistics for in-situ $PM_{10}$ . . . . .  | 60 |
| 5.10 | Analysis and increments of accumulation mode $SO_4^{2-}$ ( <i>WASO</i> ) .                    | 62 |
| 5.11 | Analysis field and increments of coarse mode anthropogenic aerosols ( <i>INSO</i> ) . . . . . | 63 |
| 5.12 | Analysis field and increments of accumulation mode elemental carbon ( <i>SOOT</i> ) . . . . . | 64 |

---

|      |   |     |
|------|---|-----|
| 5.13 | Analysis field and increments of coarse mode sea salt ( <i>SEAS</i> ) . . . . . | 65  |
| 5.14 | Analysis field and increments of mineral dust <i>VSOILA</i> . . . . .           | 66  |
| 5.15 | Analysis field and increments of $PM_{10}$ . . . . .                            | 67  |
| 5.16 | Assimilation schedule . . . . .   | 72  |
| 5.17 | Domains and in-situ measurements ZEPTEP-2 . . . . .                             | 73  |
| 5.18 | Assimilation performance, ground and satellite observations . . . . .           | 75  |
| 5.19 | Assimilation performance, airborne and total . . . . .                          | 76  |
| 5.20 | Comparison of $PM_{2.5}$ and $PM_{10}$ . . . . .                                | 77  |
| 5.21 | Time series of $PM_{2.5}$ and $PM_{10}$ . . . . .                               | 78  |
| 5.22 | Forecast performance of $PM_{10}$ on nested grids . . . . .                     | 79  |
| 5.23 | Bias reduction on nested grids . . . . .  | 80  |
| 5.24 | Munich-Stachus vs. Istanbul-Aksaray . . . . .                                   | 81  |
| 5.25 | Measured $PND_3$ along track of flight 14 . . . . .                             | 82  |
| 5.26 | $PND_3$ assimilation of Flight F14 . . . . .                                    | 83  |
| 5.27 | $PND_3$ analysis increments for flight F14 . . . . .                            | 84  |
| 5.28 | $PND_3$ analysis increments for flight F14 (vertical cross section) . . . . .   | 85  |
|      |   |     |
| C.1  | $PND$ assimilation of Flight F13 . . . . .                                      | 98  |
| C.2  | $PND$ assimilation of Flight F15 . . . . .                                      | 99  |
| C.3  | $PND$ assimilation of Flight F16 . . . . .                                      | 100 |
| C.4  | $PND$ assimilation of Flight F17 . . . . .                                      | 101 |
| C.5  | $PND$ assimilation of Flight F18 . . . . .                                      | 102 |
| C.6  | $PND$ assimilation of Flight F19 . . . . .                                      | 103 |
| C.7  | $PND$ assimilation of Flight F20 . . . . .                                      | 104 |
| C.8  | $PND$ assimilation of Flight F21 . . . . .                                      | 105 |
| C.9  | $PND$ assimilation of Flight F22 . . . . .                                      | 106 |
| C.10 | $PND$ assimilation of Flight F23 . . . . .                                      | 107 |

---

## List of Tables

---

|     |  |    |
|-----|--|----|
| 3.1 | Standard deviations and initial diameters of the modes in MADE.  | 21 |
| 3.2 | Aerosol species and number concentration processed in MADE and their modal assignment. Species denominations are taken from MADE source code. . . . .  | 22 |
| 3.3 | Input and output parameter and their relation to the model species . . . . .   | 26 |
| 3.4 | List of satellite instruments the SYNAER retrieval has been adapted to. Operational cycles taken from <a href="http://earth.esa.int">http://earth.esa.int</a> .  | 32 |
| 3.5 | SYNAER AOT types as used within retrieval and as delivered in data product according to <i>Holzer-Popp et al.</i> [2008] . . . . .   | 33 |
| 3.6 | Predefined mixtures within the SYNAER retrieval. . . . .   | 34 |
| 3.7 | Mapping of the SYNAER AOT types onto a reduced set of EURAD-IM SYNAER-H-Operator AOT types for the use in data assimilation. Tolerances are maximum values for which the H-Operator is valid . . . . .                                       | 35 |
| 3.8 | List of types of SYNAER aerosol optical thicknesses and the EURAD-IM contributing species separated by mode. See Table 3.2 for a detailed description of EURAD-IM Species . . . . .  | 36 |
| 5.1 | Assimilation schedule for the episode of July 2003. Assimilation specifications and the number of available observations for each day of the episode. While EEA stations deliver hourly values, each single SYNAER pixel is counted. . . . . | 52 |

---

|     |   |    |
|-----|---|----|
| 5.2 | List of ZEPTEP-2-flights . . . . .  | 69 |
| 5.3 | Configuration of the Zepter-2 nested grids. Computing time refers to a 72-hour forecast. . . . .                                | 70 |
| 5.4 | Data assimilation configuration used on the nested grids during the ZEPTEP-2 campaign . . . . .                                 | 71 |
| A.1 | Vertical structure of the model grid . . . . .  | 91 |
| B.1 | Number of available EEA in-situ stations and total number of $PND_3$ and SYNAER AOT observations for the 45 km <i>EUR</i> grid. | 94 |
| B.2 | Number of available EEA in-situ stations and total number of $PND_3$ and SYNAER AOT observations for the 15 km <i>CEN</i> grid. | 95 |
| B.3 | Number of available EEA in-situ stations and total number of $PND_3$ and SYNAER AOT observations for the 5 km <i>ZP2</i> grid.  | 96 |

---

## List of Acronyms

---

|                 |  |
|-----------------|--|
| <b>AATSR</b>    | Advanced ATSR  |
| <b>3D-var</b>   | Three-Dimensional Variational  |
| <b>4D-var</b>   | Four-Dimensional Variational   |
| <b>AERONET</b>  | AERosol RObotic NETwork  |
| <b>AERO-SAM</b> | AEROSol characterization from Space by advanced data<br>Assimilation into a tropospheric chemistry Model |
| <b>AOD</b>      | Aerosol Optical Depth  |
| <b>AOT</b>      | Aerosol Optical Thickness  |
| <b>AVHRR</b>    | Advanced Very High Resolution Radiometer   |
| <b>BECM</b>     | Background Error Covariance Matrix   |
| <b>BLAOT</b>    | Boundary Layer Aerosol Optical Thickness   |
| <b>BLUE</b>     | Best Linear Unbiased Estimate  |
| <b>CPC</b>      | Condensation Particle Counter  |
| <b>CTM</b>      | Chemistry Transport Model  |
| <b>DFD</b>      | Deutsches Fernerkundungsdatenzentrum   |
| <b>DFG</b>      | Deutsche Forschungsgemeinschaft German Science Foun-<br>dation   |
| <b>DLR</b>      | Deutsches Zentrum für Luft- und Raumfahrt  |
| <b>ECMWF</b>    | European Centre for Medium-Range Weather Forecast  |
| <b>EEA</b>      | European Environment Agency  |
| <b>EEM</b>      | EURAD Emission Model   |
| <b>EnKF</b>     | Ensemble Kalman Filter   |

---

|                  |   |
|------------------|---|
| <b>ENVISAT</b>   | ENVIronmental SATellite   |
| <b>ERS-1/2</b>   | European Remote sensing Satellite 1 and 2                                   |
| <b>EURAD-IM</b>  | European Air Pollution Dispersion - Inverse Model                           |
| <b>FEOM</b>      | Fully Equivalent Operational Model  |
| <b>GOME</b>      | Global Ozone Mapping Experiment   |
| <b>GOME-2</b>    | second Global Ozone Monitoring Experiment                                   |
| <b>GPS</b>       | Global Positioning System   |
| <b>HDMR</b>      | High Dimensional Model Representation                                       |
| <b>KF</b>        | Kalman Filter   |
| <b>L-BFGS</b>    | Limited-Memory Broyden Fletcher Goldfarb Shanno                             |
| <b>MADE</b>      | Modal Aerodol Dynamics model for Europe                                     |
| <b>MetOp-A</b>   | METEorological OPERational satellite-A                                      |
| <b>MIM</b>       | Mainz Isoprene Mechanism  |
| <b>MM5</b>       | Fifth-Generation NCAR / Penn State Mesoscale Model                          |
| <b>MODIS</b>     | MODERate-resolution Imaging Spectroradiometer                               |
| <b>NASA</b>      | National Aeronautics and Space Administration                               |
| <b>NCAR</b>      | National Center for Atmospheric Research                                    |
| <b>NCEP</b>      | National Center for Environmental Prediction                                |
| <b>NMC</b>       | National Meteorological Center  |
| <b>RACM</b>      | Regional Atmospheric Chemistry Mechanism                                    |
| <b>RADM</b>      | Regional Acid Deposition Model  |
| <b>RIU</b>       | Rheinisches Institut für Umweltforschung                                    |
| <b>RPM</b>       | Regional Particulate Model  |
| <b>RPMARES</b>   | Regional Particulate Model Aerosol REacting System                          |
| <b>SCIAMACHY</b> | Scanning Imaging Absorption Spectrometer for Atmospheric Chartography       |
| <b>SORGAM</b>    | Secondary ORGanic Aerosol Model   |
| <b>SPRINTARS</b> | Spectral Radiation-Transport Model for Aerosol Species                      |
| <b>SYNAER</b>    | SYNergistic AErosol Retrieval   |
| <b>UTC</b>       | Coordinated Universal Time  |
| <b>VOC</b>       | Volatile Organic Compounds  |
| <b>WRF-chem</b>  | Weather Research and Forecast (WRF) model coupled with CHEMistry (WRF-Chem) |
| <b>ZEPTER-2</b>  | second ZEPpelin based Tropospheric photochemical chemistry expERiment       |

# CHAPTER 1

---

## Introduction

---

Since the advent of numerical atmospheric modeling in the 1950ies there has been an endeavor to enhance the models' prediction skills and to process a maximum of available information to achieve a representation of the state of the atmosphere that is as accurate as possible. The complexity of models has been rising with the increase of computational power. The spatial and temporal resolution of model grids has become increasingly finer, the representation of physical processes has become more elaborate, and, in terms of chemistry transport modeling, the number of chemical compounds and, hence, reactions has become larger. But still, it is apparent that a good prediction does need a reasonable estimate to start from, a set of optimum initial values. The provision of initial values by employing as much available information as possible is the traditional goal of data assimilation. It combines the new, yet mostly sparse information from observations with the physical and chemical knowledge of atmospheric processes encoded in the numerical models.

From numerical weather simulations (see for example *Lorenc* [1986]) the various techniques consequently found their way to chemistry transport modeling. Here, the works of *Elbern et al.* [1997] and *Elbern and Schmidt* [2001] showed the usefulness of a four dimensional variational data assimilation (4D-var) system applied to provide both, optimised initial values as well as optimised emission factors, with EURAD-IM (EURopean Air pollution Dispersion - Inverse Model, *Ebel et al.* [1993], *Ebel et al.* [1997]). In 1997 the ECMWF (European Centre for Medium-Range Weather Forecast) developed the first meteorologi-

cal 4D-var system for operational use (*Rabier et al.* [2000]).

In the recent decade aerosols more and more came into the view of science and politics. Their impact on human health has been investigated largely, as shown by *Brimblecombe and Maynard* [2001] or the CAFE report by *European Commission* [2005]. Furthermore, the significance of aerosols concerning the earth's radiative budget and, hence, influencing the global climate (*Intergovernmental Panel on Climate Change* [2001]) motivates efforts to get a best possible estimate of the atmospheric aerosol burden. Their impact can be direct, in terms of scattering, reflection, and absorption of solar light as well as the earth's long wave radiation, the so called "direct forcing". On the other side, aerosols act as cloud condensation nuclei (CCN) with the effect of an increased rate of cloud formation leading to an enhanced albedo. This effect is called "indirect forcing".

Various effects of aerosols do not only depend on their physical properties but also on their composition. Salt aerosol mainly found in coastal areas but also induced deliberately in health resorts is said to have a positive effect on the respiratory system. On the other side mineral dust from volcanic eruptions may cause serious damage to aircrafts. These very distinct effects of the different substances an aerosol can be composed of brings up the necessity for differentiated aerosol simulations. While this is already standard in many aerosol models, there still is a lack of type resolved aerosol measurements to either evaluate the models or to assimilate them. The first steps in 3D-var assimilation of AOT into a model with evolving aerosols were accomplished by *Collins et al.* [2001] using four species, sulfate, carbonaceous, mineral dust, and sea salt. More recently, *Kahnert* [2009] showed the beneficial impact on aerosol forecast by applying 3D-var on AOT in a model using seven species in four size bins. Also, *Pagowski et al.* [2010] showed the valuable impact of optimised initial values by 3D-var of ground based  $PM_{2.5}$ . This study was conducted with MADE. Another approach with Ensemble Kalman Filtering (EnKF) was made by *Schutgens et al.* [2010] using a two species parameterisation (fine and coarse mode particles) for the assimilation of AERONET AOD (AErosol RObotic NETwork) in the SPRINTARS model (Spectral Radiation-Transport Model for Aerosol Species). The ECMWF is currently operating a 4D-var-scheme with three size bins each for dust and sea salt and one size bin each for organics, black carbon, and sulfate assimilating unspecified MODIS (MODERate-resolution Imaging Spectroradiometer) AOD (*Benedetti et al.* [2009]). All of the studies mentioned above use bulk measurements for assimilation, i.e. integrated values like  $PM_x$  or AOT that give no information on the aerosol composition. Even more, these model setups are bound to their modeled aerosol

---

compositions, since all of them use the technique of repartitioning (reassigning the analysis to the *a priori* composition of aerosols). While 4D-var is able to assimilate measurements “where and when they are”, the EnKF needs to accumulate the measurement into several assimilation windows. The 3D-var approach generates new model states at one point in time. Except for the study presented by *Pagowski et al.* [2010] whose model has a resolution of 12 km, all simulations have been accomplished on rather coarse grids with spacings of 25 km and more.

So far, the inverse modeling of the physical properties of aerosols in a box model was given by *Sandu et al.* [2005], who presented an adjoint of the coagulation scheme, and *Henze et al.* [2004] who introduced an inverse mechanism for condensational growth.

Addressing the above characteristics this study presents an assimilation system, that

- is capable of ingesting type resolved observations,
- can process particle properties, namely particle number densities,
- is applicable on highly resolved grids,
- and delivers smooth and timely coherent analysis fields as an intrinsic property of the 4D-var approach..

First of all, the proper observations need to be at hand. Besides the few so called super sites which measure separate aerosol components like sulphate, nitrate, or chloride most of the available aerosol in-situ observations deliver lump measurements that contain only the overall mass concentration of particles up to a certain diameter, like  $PM_{10}$ . Another important source of information on atmospheric aerosols are remote sensing instruments aboard several satellites which in general deliver overall aerosol optical thicknesses. Here, again, no information on the composition of the aerosol is contained. However, the SYNAER retrieval system (*Holzer-Popp et al.* [2002b]) developed at DLR-DFD offers type resolved aerosol optical thicknesses and, thus, the opportunity to assimilate not only AOT, but also assign it to certain species contained in the model. Finally, this leads to a more comprehensive representation of the atmosphere’s aerosols. As another novelty, particle number densities with a high temporal resolution gathered during an airborne measurement campaign were at hand.

The four dimensional variational data assimilation system for aerosols was added to the already existing foundation of a sophisticated gas-phase 4D-var system. The aerosol model MADE (Modal Aerodol Dynamics model for Europe, *Ackermann* [1997], *Ackermann et al.* [1998]) was expanded by an adjoint condensation scheme. Therefore, the original condensation scheme (*Friese and Ebel* [2010]) was replaced by a FEOM (Fully Equivalent Operational Model, *Nieradzik* [2005]) based on the principle of HDMR (High Dimensional Model Representation, see *Rabitz and Alis* [1999]). This FEOM consists of a set of multidimensional multivariate functions which, besides being much faster in computation than its predecessor, facilitates the building of an adjoint. Furthermore, the respective observation operators for the various observations have been built. Altogether, it proves to be a skillful tool to improve mesoscale simulation of tropospheric aerosols.

This study is organised as follows: In chapter 2 an overview is given on four dimensional variational data assimilation including a comparison with the most common data assimilation techniques. Subsequently the EURAD-IM model system and its aerosol model MADE are introduced in chapter 3 along with the newly implemented algorithms. Chapter 4 addresses the various types of aerosol related measurements which the EURAD-IM is now able to assimilate. Furthermore, the observation-operators necessary to map from model space to observation space and their adjoints are presented here. The application of the aerosol assimilation system on two selected episodes is illustrated in chapter 5, along with validation results of the system and an evaluation of the impact of optimised aerosol initial values on the forecast quality. This thesis finally concludes in chapter 6 where a summary and an outlook on future research options is given.

## CHAPTER 2

---

### Data Assimilation

---

Numerical models used in atmospheric sciences are always a simplified reproduction of the real atmosphere. They are limited in terms of their spatial and temporal resolution and to a restrictive selection of physical and chemical processes. This is a necessary trade off between accuracy and diversity (e.g. the number of species treated) on one side and computational power limitations on the other. Numerical modeling is an initial value/boundary conditions problem. Hence, the model performance will be aligned to the grade of knowledge of these. Since these conditions themselves are only modeled, i.e. the outcome of a preceding simulation, or a fixed set of climatological average values based on long term observations or investigation of relevant data sets, they are generally far from ideal. Altogether, numerical models are limited to the knowledge encoded by their programmers in form of physical laws, chemical reactions, orographic information, and the like.

Another source of information on the state of the atmosphere are measurements. They can provide a detailed insight into the atmosphere's current condition, be it on a large scale in form of satellite retrievals or be it in-situ measurements from ground based or airborne instruments. Unfortunately, this multitude of information does not directly provide the necessary initial conditions to the model, since they themselves underlay a variety of limitations. First of all, their spatial distribution tends to be rather inhomogeneous and many measurement sites are not representative for an area of the size of a model grid cell. Often the desired species are not measured directly, e.g. satellite retrievals of aerosol optical thicknesses instead of aerosol concentrations,

and, finally, they are afflicted with errors.

The techniques summarised under the concept of *Data Assimilation* have evolved from the desire of "using all available information, to determine as accurately as possible the atmospheric (or oceanic) flow" as defined by *Talagrand* [1997]. Data assimilation acts as an interface between the various types of information on the state of the atmosphere on one side and the knowledge of the physical and chemical processes in the atmosphere on the other. While observations of the atmosphere's state and composition can be very exact they are limited in time and space. Models, on the other hand, deliver a continuous and smooth image of the atmosphere but are restricted to discretisation and a limited set of equations describing the major processes. To retrieve a maximum gain of information from both these scientific tools is the goal of data assimilation.

This chapter outlines the theory of data assimilation. Furthermore, a rough survey of the various methods will be given before the variational approach, which has been applied in this work, will be described in detail. For a more comprehensive comparison of these methods see e.g. *Kalnay* [2003], *Lahoz et al.* [2010].

## 2.1 Bayes' Probability

Assume, that there is a probability density function (PDF)  $p(x)$  for the state of the atmosphere  $x$  which can be derived, e.g. from an ensemble simulation or climatology. This is the *a priori* probability to simulate  $x$ . Furthermore, if an information  $y$  on the condition is known - a measurement - and its error characteristics are available, a PDF  $p(y|x)$  can be formulated. It describes the probability of taking a measurement  $y$  when condition  $x$  holds.

Following Bayes' theorem, the *a posteriori* probability  $p(x|y)$  can be derived by

$$p(x | y) = \frac{p(y | x) p(x)}{p(y)} = \frac{p(y | x) p(x)}{\int p(y | x') p(x') dx'} \quad (2.1)$$

## 2.2 Maximum Likelihood and Minimum Variance

With the further assumption that these PDFs are of Gaussian character and  $\sigma_y$  being the standard deviation of  $y$ , the probability of measuring  $y$  when the

true state  $x$  is given can be expressed as

$$p_{\sigma_y}(y | x) = \frac{1}{\sqrt{2\pi}\sigma_y} \cdot e^{-\frac{(y-x)^2}{2\sigma_y^2}}. \quad (2.2)$$

On the other side, the likelihood of  $x$  as the true state given  $y$  is simply

$$L_{\sigma_y}(x | y) = p_{\sigma_y}(y | x) \quad (2.3)$$

In the presence of a multitude of  $N$  measurements the overall likelihood becomes

$$\begin{aligned} L_{\sigma_{y_1}, \dots, \sigma_{y_N}}(x | y_1, \dots, y_N) &= \prod_{i=1}^N \left( \frac{1}{\sqrt{2\pi}\sigma_{y_i}^2} \cdot e^{-\frac{(y_i-x)^2}{2\sigma_{y_i}^2}} \right) \\ &= \frac{1}{\sqrt{2\pi}^N \sigma_{y_1}^2 \cdots \sigma_{y_N}^2} \cdot e^{-\frac{(y_1-x)^2}{2\sigma_1^2} - \dots - \frac{(y_N-x)^2}{2\sigma_N^2}}, \end{aligned} \quad (2.4)$$

the joint probability. Consequently, the maximum of 2.4 is most likely to be true value of  $x$ . Neglecting the constant factor and taking into account that the logarithm is a monotonous function yields

$$\begin{aligned} \max(L_{\sigma_{y_1}, \dots, \sigma_{y_N}}(x | y_1, \dots, y_N)) &= \\ \max \left( \text{const.} - \frac{(y_1-x)^2}{2\sigma_{y_1}^2} - \dots - \frac{(y_N-x)^2}{2\sigma_{y_N}^2} \right). \end{aligned} \quad (2.5)$$

Taking another look at Bayes' Theorem and assuming that  $p(x)$  can be considered a prior PDF of the true state in the presence of an information  $x_0$  (the background information, also referred to as the *first guess*) that also yields a Gaussian probability in the form of  $p_{x_0, \sigma_0}(x) = (1/\sqrt{2\pi}\sigma_0) \cdot e^{-(x_0-x)^2/2\sigma_0^2}$  one can write the *a posteriori* probability of 2.2 as

$$p(x | y) = \frac{p_{\sigma_y}(y | x) p_{x_0, \sigma_0}(x)}{p_{\sigma_y}(y)} = \prod_{i=1}^N \left( \frac{1}{\sqrt{2\pi}\sigma_{y_i}} \cdot e^{-\frac{(y_i-x)^2}{2\sigma_{y_i}^2}} \right) \cdot \frac{1}{\sqrt{2\pi}\sigma_{x_0}} \cdot e^{-\frac{(x_0-x)^2}{2\sigma_{x_0}^2}} \quad (2.6)$$

The right term in 2.2 shows that the denominator is independent of  $x$ , and thus, its maximum can be obtained by maximising the numerator in an analogous manner as in 2.5.

## 2.3 Variational data assimilation

Maximising 2.5 delivers the most likely state of the atmosphere  $x^a$ , the so called *Analysis*. In data assimilation this is technically done by minimising a *Cost Function*  $J(x)$ . It is gained by multiplying 2.5 by  $-1$  and it contains the sum of the squares of the misfit of each of the observations and the background field to the state vector  $x$  weighted by their individual variance:

$$J(x) = \frac{1}{2} \left[ \frac{(y - x)^2}{2\sigma_y^2} + \frac{(x - x_b)^2}{2\sigma_{x_b}^2} \right] \quad (2.7)$$

or, as it is generally written in data assimilation:

$$J(x) = \frac{1}{2} \left[ (H(x) - y)^T \mathbf{R}^{-1} (H(x) - y) + (x - x^b)^T \mathbf{B}^{-1} (x - x^b) \right] \quad (2.8)$$

with the superscript  $T$  indicating the transposed of a vector,  $\mathbf{R}$  the *observation* or *measurement error covariance matrix*, and  $\mathbf{B}$  the *background error covariance matrix*.  $H(x)$  is called the *observation* or *forward operator*. It is a mapping from the model space into the space of the observation. This can be a simple multilinear interpolation from the model grid to the location of the measurement, but might as well be as complex as a full radiative transfer model. Different types of H-operators and their properties will be discussed in section 3.4. An important property of this formulation of the cost function is, that it is minimised with respect to  $x$ . The calculus described above is stationary in time, i.e. it delivers a BLUE (Best Linear Unbiased Estimate) of the model state for one point in time. It is therefore referred to as Three Dimensional variational data assimilation (3D-var).

## 2.4 4-dimensional variational data assimilation

It is desirable to make use of as many measurements as possible. But these are generally distributed not only in space but also in time. To find an optimum for the state of the atmosphere at a time  $t_0$  (henceforth referred to as *initial time*) taking into account all measurements within a certain temporal interval the costfunction 2.8 has to be modified to

$$J(x_0) = J^b + J^O = \frac{1}{2} (x_0 - x^b)^T \mathbf{B}^{-1} (x_0 - x^b) + \frac{1}{2} \sum_{i=1}^N \left( [H(M_i(x_0) - y_i)]^T \mathbf{R}^{-1} [H(M_i(x_0) - y_i)] \right) \quad (2.9)$$

where  $M$  is the *model operator* generating the state  $x_i$  at timestep  $i$  from the initial conditions  $x_0$ ,  $\mathbf{y}_i$  is a vector containing all observations at timestep  $i$ . The costfunction  $J(x_0)$  is now minimised to gain an optimum state  $x_0^a$ , the analysis, i.e. a BLUE of the initial conditions of the assimilation interval with respect to all observations within this interval. Minimisation is done by numerical methods, like a Conjugate Gradient or a quasi-Newton algorithm. It is accomplished by building the gradient of  $J(x_0)$  and approaching its zero. One constraint that is made in 4D-var is that the model is assumed to be errorless over the whole interval. Only the initial values are afflicted with errors. The gradient of  $J(x_0)$  with respect to  $x^b$  can easily be derived from Equation 2.9 resulting in

$$\nabla_{x_0} J^b = \mathbf{B}^{-1} (x_0 - x^b) \quad (2.10)$$

Quite similarly, the gradient of the observational part of the costfunction can be calculated

$$\nabla_{x_i} J^o = \mathbf{H}^T \mathbf{R}^{-1} (H(x_i) - y_i) \quad (2.11)$$

here, the gradient is valid at time  $t_i$  but the gradient is needed for  $t_0$ . Now, let  $\delta x_0$  be a perturbation at  $t = 0$ , then, using the model operator  $M$  from Equation 2.9 the perturbation at  $t = i$  can be defined as

$$\delta x_i := \mathbf{M}_i (x_0 + \delta x_0) - \mathbf{M}_i (x_0) \quad (2.12)$$

The tangent linear model  $\mathbf{M}'$  is a linear approximation of the model operator  $M$ , its Jacobian. It can thus be stated that

$$\delta x_i \approx \mathbf{M}'_i (\delta x_0) \quad (2.13)$$

Making use of the canonical scalar product  $\langle u, v \rangle = \sum_i u_i \cdot v_i$  one can write a variation of  $J(x)$  as a result of  $\delta x_i$  as

$$\delta J \approx \langle \nabla_{x_i} J, \delta x_i \rangle$$

This way, the term of observation costs in 2.9 can be written as

$$\delta J^o = \sum_{i=0}^N \langle \nabla_{x_i} J^o, \delta x_i \rangle$$

and with the assumption that 2.13 holds this transforms to

$$\delta J^o = \sum_{i=0}^N \langle \nabla_{x_i} J^o, \mathbf{M}'_i (\delta x_0) \rangle \quad (2.14)$$

Now, using the property  $\langle u, Cv \rangle = \langle C^T u, v \rangle$  the variation of  $J^o$  turns to

$$\delta J^o = \sum_{i=0}^N \langle \mathbf{M}^*_i \nabla_{x_i} J^o, \delta x_0 \rangle \quad (2.15)$$

where,  $\mathbf{M}^* := \mathbf{M}'^T$  is the transpose of the tangent linear, the adjoint model. The gradient of the observation costfunction can now be derived for  $t = 0$  recalling 2.11

$$\nabla_{x_0} J^o = \sum_{i=0}^N \mathbf{M}^*_i \nabla_{x_i} J^o = \sum_{i=0}^N \mathbf{M}^*_i \mathbf{H}^T \mathbf{R}^{-1} (H(x_i) - y_i) \quad (2.16)$$

Now, the whole costfunction with respect to the gradients at  $t = 0$  can be summed up to

$$\begin{aligned} \nabla_{x_0} J &= \nabla_{x_0} J^b + \nabla_{x_0} J^o = \\ &\mathbf{B}^{-1} (x_0 - x^b) + \sum_{i=0}^N \mathbf{M}^*_i \mathbf{H}^T \mathbf{R}^{-1} (H(x_i) - y_i) \end{aligned} \quad (2.17)$$

## 2.5 Kalman Filtering

The most sophisticated yet complex method is the *Extended Kalman Filter*, often referred to as the "Gold Standard of data assimilation" (*Kalnay* [2003]) in contrast to the 4D-var method it delivers the *analysis error covariance matrix*  $\mathbf{P}_i^a$  at every timestep  $i$  and does take into account the error produced by the model while propagating in time. According to *Kalnay* [2003] this can be summarised as follows: Let  $x_i^f$  be the forecasted model state at  $t = i$  propagated by the Model  $M$  from the analysis  $x_{i-1}^a$  at the preceding time-step  $t = i - 1$  then the forecast can be described as

$$x_i^f = M_{i-1} (x_{i-1}^a) \quad (2.18)$$

and a *forecast error covariance matrix*  $\mathbf{P}_i^f$  gained by propagation of  $\mathbf{P}_{i-1}^a$  via

$$\mathbf{P}_i^f = \mathbf{L}_{i-1} \mathbf{P}_{i-1}^a \mathbf{L}_{i-1}^T + \mathbf{Q}_{i-1} \quad (2.19)$$

where  $\mathbf{L}_i$  is the *Tangent Linear Model*, a linear approximation of the model  $M$  at timestep  $i$  under the condition of  $x_i^a$ , and  $\mathbf{L}_i^T$  its transposed or so called *adjoint*.  $\mathbf{Q}_i$  is a matrix representing the noise of the model, i.e. the error inflicted by the model itself. Furthermore,  $\mathbf{H}_i$  is used in the following being

the linearisation of the forward operator  $H$  at the state  $x_i^f$ . Now, the analysis for timestep  $i$  can be computed by first minimising  $\mathbf{P}^a(t_i)$  in

$$\mathbf{P}_i^a = (\mathbf{I} - \mathbf{K}_i \mathbf{H}_i) \mathbf{P}_i^f \quad (2.20)$$

and finally updating  $x_i^a$

$$x_i^a = x_i^f + \mathbf{K}_i \left( \mathbf{y}_i - H(\mathbf{x}_i^f) \right) \quad (2.21)$$

with  $\mathbf{K}$  being the so called *Kalman gain matrix* that is set up after the forecast steps as

$$\mathbf{K}_i = \mathbf{P}_i^f \mathbf{H}_i^T \left[ \mathbf{R}_i + \mathbf{H}_i \mathbf{P}_i^f \mathbf{H}_i^T \right]^{-1} \quad (2.22)$$

Equation 2.19 describes the crucial step in extended Kalman Filtering. With  $\mathbf{L}$  being of the size of the degrees of freedom of the model (which can easily be of the order of  $10^7$  or more), the step of propagating  $\mathbf{P}^a$  in time is as costly as the same number of model forward integrations. This prohibits the use of extended Kalman Filters for common problems. Several techniques have been developed, to enhance performance by reducing model size or making reasonable assumptions, like e.g. the ensemble Kalman filter, which are described in detail in *Kalnay* [2003], *Lahoz et al.* [2010] or *Daley* [1991].

## 2.6 Summary

In operational model set-ups it is common to apply pseudo-4D data assimilation. That is, applying a 3D-var scheme at, for example, every full hour. This is due to computational demands of a full 4D-var system on one hand but, above all, because no adjoint model needs to be constructed or maintained. In 4D-var assumptions have to be made about the background error covariance matrix  $\mathbf{B}$  while the extended Kalman Filter propagates the model error in time and, thus, delivers the more complete description of the state of the atmosphere. This is, on the other hand, not feasible for standard models due to the immense computational effort. Also, does the 4D-var analysis deliver a smooth and physically and chemically consistent state within the assimilation window, while Kalman filtering produces perturbations through jumps whenever an analysis step is performed.



## CHAPTER 3

---

### The model system EURAD-IM

---

The EURAD-IM model system has been developed on the base of the EURAD-CTM (EUROpean Air pollution Dispersion - Chemistry Transport Model). The suffix IM (Inverse Model) indicates that EURAD-CTM has been expanded by an inverse part for data assimilation purposes. The forward part of the model system - the standard forecast system - consists of three major models:

- **MM5**

The Mesoscale Meteorological model 5 (*Grell et al.* [1994]) acts as meteorological driver for the CTM, i.e. it delivers the meteorological fields needed like, for example, wind, relative humidity, and temperature.

- **EEM**

The EURAD-Emission-Model (*Memmesheimer et al.* [1991]) delivers emission fields tailored for the specific grid used considering diurnal cycle, day of the week, international holidays, and season.

- **CTM**

The chemistry transport model (*Hass* [1991]; *Hass et al.* [1995]; *Ebel et al.* [1997]) computes transport, chemical transformation, and deposition of gas-phase and aerosol-phase species.

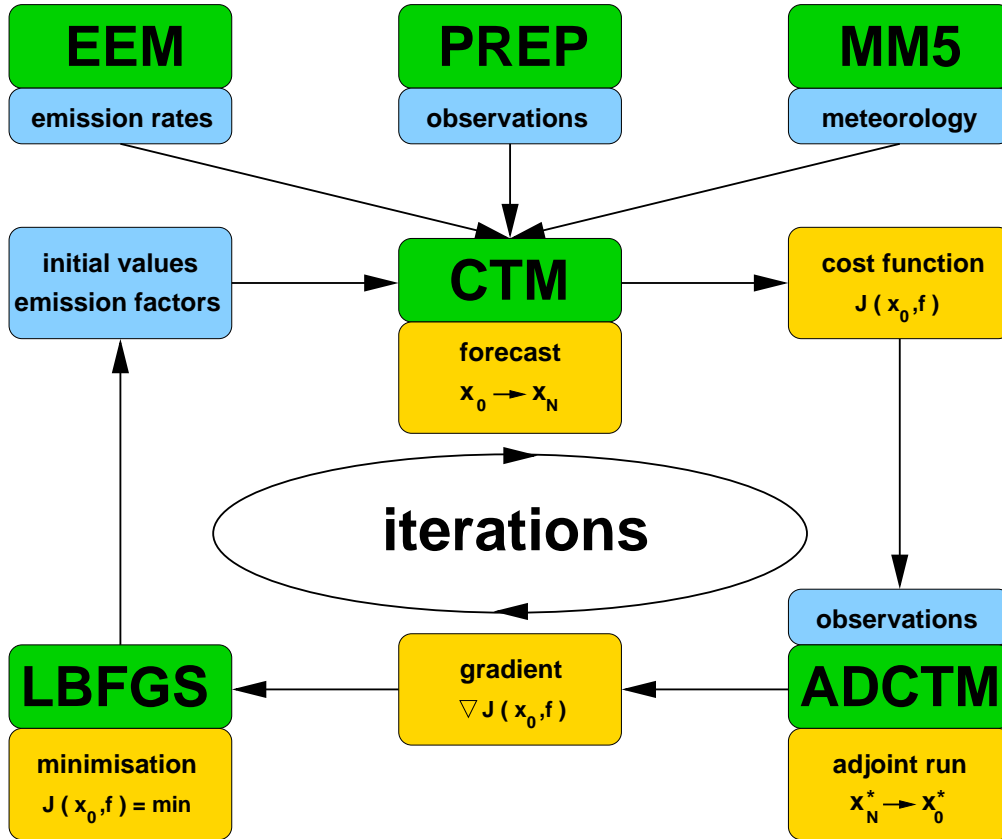


*Figure 3.1: Schematic survey of the EURAD-IM model system. Explanation in the text.*

The inverse model system contains three additional parts.

- **PREP**

The data PREProcessor provides desired measurement data from any kind of available measurement.

- **ADCTM**

Adjoints of many of the forward routines (in 4Dvar only), H-operators for the mapping between model and observation space.

- **LBFGS**

The implemented minimisation algorithm that evaluates gradient and costfunction is the Limited-memory Broyden-Fletcher-Goldfarb-Shanno algorithm (*Liu and Nocedal [1989]*).

The EURAD-IM is a Eulerian model system. The chemistry is calculated on a fixed three dimensional grid and transport is simulated as fluxes through the boundaries of each grid cell. The meteorological driver MM5 and the EEM are run offline, thus, there is no feedback from the CTM. Figure 3.1 displays the calling sequence of the particular model components and the data flow within a model simulation. A standard forecast simulation is composed of the sequential call of MM5, EEM, and CTM, though in a newer version, an online-version of the EEM is available, where emissions are calculated within the CTM. Four dimensional fields of concentrations of gas-phase and aerosol phase species are delivered as output.

An assimilation run is setup with additional features. First, another offline process, the PREP is run offline to provide desired observations in a proper way. Then, the *CTM* is run forward as in a standard forecast with the exception, that the cost function is summed up over all time steps from the beginning to the end of the simulation and that the model state is stored for each time step to be recalled in the backward run. Then, a backward or adjoint run is accomplished from the ending point to the beginning. Here, on each time step the gradients are propagated backward in time via the adjoint parts of the CTM. Here, the stored fields are used to reproduce the state of the model during the forward run. Finally, the L-BFGS minimisation algorithm receives a set of gradients and the scalar value of the cost function and delivers a vector of increments (this is explained in the context of the diffusion paradigm in Chapter 4). These are then added to the background values and a new iteration is started. This is repeated until either a break off criterion is met or a maximum number of iterations is reached.

The components relevant for the work presented in this thesis are explained in more detail in the following.

## 3.1 The EURAD-CTM

The core of the system, the CTM, simulates advection and diffusion, chemical conversion, and deposition of trace gases and aerosols in the atmosphere.

### 3.1.1 Functional principle

Basically, the CTM solves the following equation (*Hass* [1991]):

$$\frac{\partial c_i}{\partial t} = -\nabla(\mathbf{u}c_i) + \nabla(\mathbf{K}\nabla c_i) + \frac{\partial c_i}{\partial t}|_{chem} + E_i + F_i + \frac{\partial c_i}{\partial t}|_{cloud} + \frac{\partial c_i}{\partial t}|_{aerosol} \quad (3.1)$$

Here,  $c_i$  indicates the mean concentration of the species  $i$ . The terms on the right hand side of Equation (3.1) represent changes of concentration due to the following processes:

- $\nabla(\mathbf{u}c_i)$ : Advection, that is transport by wind, where  $\mathbf{u}$  is the vector of wind velocity
- $\nabla(\mathbf{K}\nabla c_i)$ : Turbulent diffusion, with the tensor of turbulent diffusion  $K$
- $\frac{\partial c_i}{\partial t}|_{chem}$ : Chemical conversion in the gas phase
- $E_i$ : Emission rates
- $F_i$ : Sum of the following fluxes:
  - $F_{i,emis}$ : Flux by emissions from the surface
  - $F_{i,dep}$ : Flux by dry deposition to the surface
- $\frac{\partial c_i}{\partial t}|_{cloud}$ : Aqueous chemistry, transport in clouds and wet deposition
- $\frac{\partial c_i}{\partial t}|_{aerosol}$ : Aerosol chemistry processed in MADE

A so called *operator splitting* is applied (see *McRae et al.* [1982]) on the processes of dynamics. The processes of advection and diffusion are split and symmetrically arranged around the solver modules for gas-phase chemistry and aerosol dynamics following

$$x_i(t + \Delta t) = \mathcal{T}_h \mathcal{T}_v \mathcal{D}_v \mathcal{C} \mathcal{M} \mathcal{D}_v \mathcal{T}_v \mathcal{T}_h x_i(t) \quad (3.2)$$

with  $x_i$  denoting the model state, that is a concentration or mixing ratio, of species  $i$ ,  $t$  the time step,  $\Delta t$  length of a time step,  $\mathcal{T}_{h/v}$  the advection module in horizontal and vertical direction, respectively,  $\mathcal{D}_v$  the vertical diffusion,  $\mathcal{C}$  the gas-phase chemistry solver, and  $\mathcal{M}$  the aerosol dynamics module MADE. Here, the  $\mathcal{T}$  and  $\mathcal{D}$  are applied for one half of the model's timestep before and one half after chemistry and aerosol dynamics (see *Hass* [1991]).

The current EURAD-CTM uses the Bott upstream advection-scheme *Bott* [1989] of fourth order in both, vertical and horizontal direction. An adjoint of this advection-scheme is available. The inverse model integration of the gradient is then represented by

$$x_i^*(t - \Delta t) = \mathcal{T}_h^T \mathcal{T}_v^T \mathcal{D}_v^T \mathcal{M}^T \mathcal{C}^T \mathcal{D}_v^T \mathcal{T}_v^T \mathcal{T}_h^T x_i^*(t) \quad (3.3)$$

where  $x_i^*(t)$  is the adjoint variable  $i$  at time  $t$ , as denoted in chapter 2.4. The superscript  $T$  denotes the adjoint of the affected operator.

Originally, the EURAD-CTM was built up around the RADM (Regional Acid Deposition Model, *Chang et al.* [1987]). In these studies the Chemistry is represented by the RACM (Regional Atmospheric Chemistry Mechanism, *Stockwell et al.* [1997]) and an extension based on the MIM (Mainz Isoprene Mechanism, *Geiger et al.* [2003]). Moreover, it contains the sophisticated aerosol model MADE described in more detail later in this chapter. The description of the adjoint model concerning gas-phase has already been described in detail in *Elbern and Schmidt* [1999], *Elbern et al.* [2000], and *Elbern and Schmidt* [2001] and emission factor optimisation has been accomplished and analysed in *Strunk* [2006] and *Elbern et al.* [2007]. Therefore, these parts will not be treated here.

### 3.1.2 Grid specifications

The grid of EURAD-CTM is a Lambert conformal conic projection with an equidistant rectangular horizontal spacing. The state variables are represented in a way following the Arakawa C-Grid definition (*Arakawa and Lamb* [1977]) and the layers are determined by terrain following sigma coordinates that are defined as

$$\sigma_k = \frac{p_k - p_{top}}{p_{bot} - p_{top}} \quad (3.4)$$

with  $k$  being the layer number and  $p_{bot,k,top}$  the pressure at the surface, layer  $k$ , and the top of the model, respectively. An overview of the constitution of the vertical layers is given in appendix A.

#### Lateral boundary conditions

The vertical grid defined by Equation 3.4 are also used to represent the conditions at the lateral boundaries, the ring of the outermost grid cells of the model's mother domain. From measurements and climatological information a fixed set of boundary values has been derived depending on layer and latitude. In the case of inflow the flux into the model domain is given by

$$F_b = \mathbf{u}^\perp C_{i,b} \quad (3.5)$$

where  $\mathbf{u}^\perp$  is the wind velocity perpendicular to the boundary. On out flowing conditions a constant advection through the two two grid boxes is applied, i.e. fluxes into and out of the boundary grid cell are equal. This is done to avoid reflection of out flowing waves. The lateral boundaries are located in regions of low pollution. The area of interest should be chosen in a certain distance to

the boundaries to avoid a strong influence on the simulation (see *Schell* [1996] for a detailed description).

### Vertical boundary conditions

The top boundary of the CTM is set fix at 100 *hPa*. The diffusive vertical fluxes at the top of the top layer are set to zero. Thus, it functions as a lid. The bottom boundary is the earth's surface and here the boundary conditions are represented by deposition and emission, the terms  $F_{i,emis}$  and  $F_{i,dep}$  of Equation 3.1.

#### 3.1.3 Initialisation

From available measurements of the transported species latitude-dependent vertical profiles are derived (*Chang et al.* [1987]) and equally distributed over the whole model domain. Values of short-lived species are set to zero. With these conditions a spin up run of four or five days is computed to provide realistic three dimensional fields of initial values for the desired episode (see *Schell* [1996]). If available, a simulation can be set up on existing restart files from previous simulations or on interpolated fields from a mother domain. Best, of course, would be optimised initial values from data assimilation.

## 3.2 The aerosol model MADE

The MADE (Modal Aerosol Dynamics module for Europe (*Ackermann* [1997], *Ackermann et al.* [1998])) simulates the physical and chemical processes concerning particles within the EURAD-IM, based on gas-phase concentrations provided by the CTM, meteorological values from the MM5, and emissions. By simulating gas-to-particle conversion (the bidirectional transfer between gas and aerosol phase) there is a direct coupling between aerosol and gas-phase in the EURAD-CTM. With the SORGAM (Secondary ORGANIC Aerosol Model, *Schell et al.* [2001]) a sophisticated model for secondary organic aerosols is implemented in the core of MADE. As displayed in Equations 3.2 and 3.3, the physical transport and the diffusion of aerosols are treated along with the gas-phase species. The MADE has its origin in the Regional Particulate Model (RPM, *Binkowski and Shankar* [1995]). This section shall give an overview of the different processes involved in aerosol modeling and presents the modifications that were made to facilitate aerosol data assimilation.

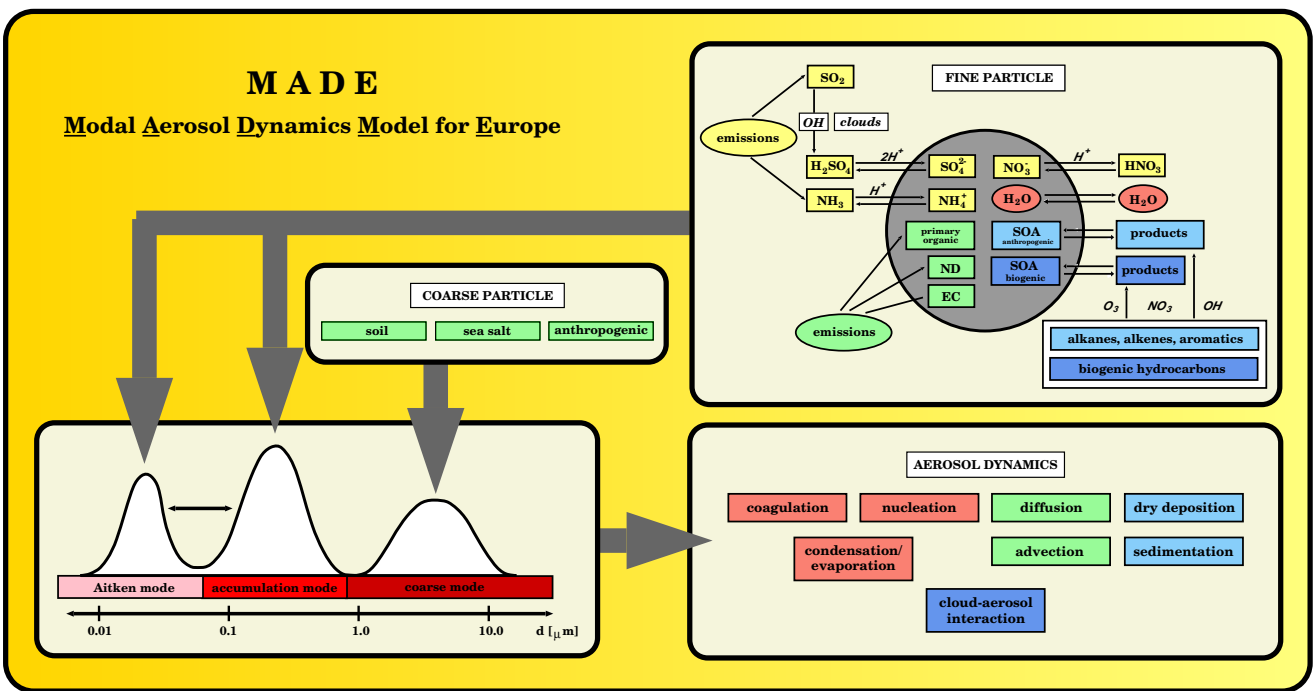


Figure 3.2: Schematic survey of the MADE (Schell et al. [2001]).

### 3.2.1 Size distribution

First of all, the particles in MADE are separated into two groups: Fine and coarse particles. In the overview given in Figure 3.2 these are represented by the respective boxes (fine particles in the upper right and coarse particles in the small box in the center). As depicted, these groups undergo different processes and have different sources. The coarse particles, namely sea salt, mineral dust, and coarse particles with anthropogenic origin, are primary aerosols with no exception. This means they are emitted as they are. The group of fine particles encompasses smaller primary aerosols like elemental carbon, smaller sea salt particles, and unspecified anthropogenic particles as well as secondary aerosols. Secondary aerosols are formed from gaseous precursors by gas-to-particle conversion. These precursors can be products of combustion processes, emitted compounds of production processes, or of biogenic origin. The aerosol phase is indicated by the circle in the upper right box of Figure 3.2 representing a particle. The single processes are explained in more detail in the following subsections. Following *Whitby* [1978], a trimodal log-normal representation for the size distribution within MADE is chosen. Here, a separation of the group of fine particles into two modes has been made. The Aitken mode represents freshly emerged, very small aerosols while the accumulation mode contains the aged aerosols. Coarse particles are assigned to the coarse mode. The modes are defined as a Gaussian distribution around a median diameter with a fixed standard deviation each, so that for the full description of one mode only its particle number concentration and the mass concentrations of its components need to be known and, thus, simulated. First, the two moments  $\mathcal{M}_{0,i}$  and  $\mathcal{M}_{3,i}$  are introduced via an integration over the particle diameter  $D_p$

$$\mathcal{M}_{0,i} = \int_0^{\infty} D_p^0 n_i(D_p) dD_p = N_i \quad (3.6)$$

$$\mathcal{M}_{3,i} = \int_0^{\infty} D_p^3 n_i(D_p) dD_p = \frac{6}{\pi} V_i = \frac{6}{\pi} \sum_m \frac{c_{m,i}}{\rho_m} \quad (3.7)$$

Here,  $N_i$  [ $1/m^3$ ] is the number concentration and  $V_i$  [ $m^3/m^3$ ] the volume concentration of mode  $i$ ,  $c_{m,i}$  the mass concentration and  $\rho_m$  the density of species  $m$  in mode  $i$ . With the log-normal distribution function being defined as

$$n_i(\ln D_p) = \frac{N_i}{\sqrt{2\pi} \ln \sigma_{g,i}} \exp \left[ -\frac{(\ln D_p - \ln D_{g,i})^2}{2 \ln^2 \sigma_{g,i}} \right] \quad (3.8)$$

where  $D_{g,i}$  denotes the median diameter and  $\sigma_{g,i}$  the standard deviation of the distribution. The standard deviations are set to fixed values as listed in Table

3.1. With this information and the knowledge of number density and mass concentrations of a mode  $i$  its whole size distribution is known at any time via

$$D_{g,i} = \sqrt[3]{\frac{\mathcal{M}_{3,i}}{\mathcal{M}_{0,i}} \exp\left(-\frac{9}{2} \ln^2 \sigma_{g,i}\right)}. \quad (3.9)$$

The median diameters given in Table 3.1 are used to calculate initial number

**Table 3.1:** Standard deviations and initial diameters of the modes in MADE.

|                   | $\sigma_{g,i}$ | $D_{g,i}^{init}$ |
|-------------------|----------------|------------------|
| Aitken mode       | 1.7            | 0.01             |
| accumulation mode | 2.0            | 0.07             |
| coarse mode       | 2.2            | 1.0              |

concentrations from given mass concentrations and act as minimum median diameters. Currently, there are 37 independent aerosol variables, including the particle numbers for each mode, simulated by MADE that are distributed over the three modes as described in Table 3.2.

### 3.2.2 Aerosol dynamics

Aerosols undergo several physical processes which will shortly be explained in here. The transport of aerosols is covered along with the gas-phase species as displayed in Equation 3.2. Each of the following processes acts on the aerosol of a mode as a whole. This means that the composition of the aerosol remains unchanged, only the moments  $\mathcal{M}_0$  and  $\mathcal{M}_3$  are affected.

#### Nucleation

The generation of fresh very small particles by formation of molecular clusters is called nucleation. In MADE, binary homogeneous nucleation of sulfuric acid and water is simulated. Homogeneous indicates that no preexisting surface is involved (see *Kulmala et al.* [1998]).

#### Condensation

Condensation represents particle growth by transfer of volume from gas-phase or vapor into the aerosol phase. The condensation of sulfuric acid and condensation/evaporation of low volatile vapors is implemented in MADE. Con-

**Table 3.2:** Aerosol species and number concentration processed in MADE and their modal assignment. Species denominations are taken from MADE source code.

|                                    | Aitken   | Accumulation | Coarse |
|------------------------------------|----------|--------------|--------|
| Primary aerosols                   |          |              |        |
| Elemental carbon                   | ECI      | ECJ          | -      |
| Primary organic                    | ORGPAI   | ORGPAJ       | -      |
| Primary anthropogenic              | P25AI    | P25AJ        | ANTHA  |
| Marine (sea salt)                  | -        | SEASAJ       | SEAS   |
| Soil derived mineral dust          | -        | -            | SOILA  |
| Secondary inorganic aerosols (SIA) |          |              |        |
| Sulfate $SO_4^{2-}$                | SO4AI    | SO4AJ        | -      |
| Ammonium $NH_4^+$                  | NH4AI    | NH4AJ        | -      |
| Nitrate $NO_3^-$                   | NO3AI    | NO3AJ        | -      |
| Aerosol liquid water $H_2O$        | H2OAI    | H2OAJ        | -      |
| Secondary organic aerosols (SOA)   |          |              |        |
| Anthropogenic from aromatic 1      | SOAARO1I | SOAARO1J     | -      |
| Anthropogenic from aromatic 2      | SOAARO2I | SOAARO2J     | -      |
| Anthropogenic from alkenes         | SOAALK1I | SOAALK1J     | -      |
| Anthropogenic from olefines        | SOAOLE1I | SOAOLE1J     | -      |
| Biogenic from $\alpha$ -pinene 1   | SOAAPI1I | SOAAPI1J     | -      |
| Biogenic from $\alpha$ -pinene 2   | SOAAPI2I | SOAAPI2J     | -      |
| Biogenic from limonene 1           | SOALIM1I | SOALIM1J     | -      |
| Biogenic from limonene 2           | SOALIM2I | SOALIM2J     | -      |
| Particle number                    | NU0      | AC0          | CORN   |

densation is considered an aerosol aging effect. This process only affects fine particles.

### Coagulation

This process describes the fusion of two particles by collision. This has two important effects. First, by intramodal coagulation the particle number concentration of a mode is being reduced while its volume remains constant, i.e. the particles of a mode become less but larger. Secondly, by intermodal coagulation, the resulting particle is assigned to the bigger one of the modes. This results in a reduction of both, particle number and volume for the smaller mode and an increase of volume for the bigger mode. Both these effects contribute to aerosol aging. The process of coagulation is only applied to Aitken and accumulation mode in MADE.

### Wet/Dry deposition and sedimentation

These are the processes in MADE that remove aerosols from the model. Sedimentation describes the settling of particles driven by gravitation. It is treated as a downward advection process of particles to the surface layer. The process of dry deposition describes the ad- or absorption of particles by the surface. This process only takes place in the surface layer of the model. Wet deposition describes the removal of particles by coagulation with rain or cloud droplets.

### 3.2.3 Aerosol chemistry

The aerosol chemistry is of great importance for aerosols modeling. It encompasses the transfer of liquid water from vapor to aqueous phase and the formation of secondary aerosols, i.e. aerosols that are formed by gas-to-particle conversion of inorganic and organic precursors. These processes have a large impact on aerosol development. The mass proportion of secondary aerosols in the overall aerosol amount in the model varies between 40% and 90%, where a large amount of the primary aerosols is assigned to the coarse mode species *ANTHA* and *SOILA*. Thus, it can be stated that most of the fine aerosols (Aitken and accumulation mode) are of secondary nature and these predominantly consist of secondary inorganics.

#### Secondary inorganic aerosols

The most important mechanism for fine particles is the solution of the equilibrium of the system  $H^+ - NH_4^+ - SO_4^{2-} - NO_3^- - H_2O$ , the secondary inorganic aerosols (SIA). The original solver for this system in MADE was the RPMARES (Regional Particulate Model Aerosol REacting System, *Binkowski and Shankar* [1995]) based on the MARS(*Saxena et al.* [1986]) and SCAPE (*Kim et al.* [1993]) models, in which activity coefficients were considered as temperature independent. Furthermore, the assumptions made for the a priori determination of the composition of SIA produced mathematical discontinuities, which prohibited building an adjoint of it. The state-of-the-art mechanism, the PSC/APC developed and implemented by *Friese and Ebel* [2010], solves this system using an iterative approach with temperature depending activity coefficients (PSC: Pitzer-Simonson-Clegg model, e.g. *Clegg et al.* [1992]; APC: Analytical Predictor for Condensation, *Jacobson* [1997]). This mechanism is more accurate, has a much wider range of validity in terms of temperature, and its output is continuous. Unfortunately, this mechanism is computationally very demanding due to its iterative nature. As a remedy, a

HDMM (High Dimensional Model Representation, *Rabitz and Alis* [1999], an IO mapping technique) was built of the PSC/APC to replace it for operational purposes and to get an algorithm of which an adjoint could be built (*Nieradzik* [2005]). A description is given in section 3.2.5.

### Secondary organic aerosols

The formation and partitioning of secondary organic aerosols (SOA) is simulated by the SORGAM (Secondary ORGanic Aerosol Model) implemented in MADE. SOA account for up to 10 % of the fine particles in EURAD-IM. SOA are formed from gaseous organic precursors in the presence of oxidising compounds like  $O_3$  or the radicals  $OH$  or  $NO_3$ . The partitioning between gas and aqueous phase is determined by a thermodynamic equilibrium. A detailed description is given in *Schell et al.* [2001].

### 3.2.4 Emissions

Primary aerosols, as defined in Table 3.2, are emitted directly from a source and do not undergo any chemical conversion. In the case of elemental carbon, organic carbon, and other fine particles of anthropogenic origin emissions are provided by the EEM. These emissions are compiled from land-use characteristics and emission inventories and delivered for each model grid. They are subject to seasonal, weekly, and diurnal variations. Additionally, the EURAD-IM contains online emission models for mineral dust and marine sea salt, that simulate wind driven aerosol uptake.

### 3.2.5 Adjoint chemistry for secondary inorganic aerosols

Being the core of the MADE some efforts have been made to enhance and expand the chemistry of secondary inorganic aerosols (SIA). A survey of the approaches in the EURAD-IM has been given in 3.2.3. The most recent one was the replacement of the PSC/APC mechanism by a High Dimensional Model Representation (HDMM) already with the intention to build an adjoint. This subsection shall give a rough survey over the functional principles of HDMM and a glimpse onto its adjoint. The idea of the high dimensional model representation, as its name implies, was to find a replacement for computationally demanding models with many input parameters (e.g. *Shorter et al.* [1999] and *Shorter et al.* [2000]). HDMM is an IO-mapping technique, a learning algorithm that aims to represent the output of a model by a set of multidimensional multivariate functions. A stand alone Fully Equivalent Operational

Model (FEOM) shall then be able to replace the original model for operational purposes. Furthermore, it is based on the assumption that in models that follow physical laws the degree of nonlinearity is rather low. In other words, a change in result after a variation of one input-parameter plus the change by varying another will generally resemble the change resulting from a combined variation of both.

### Principles of HDMR

The foundations of HDMR are represented in *Rabitz and Alis* [1999]. There are a few variations of HDMR. The type implemented in the EURAD-IM is called cut-HDMR, as described in *Rabitz et al.* [1999]. The resulting FEOM is an interpolating FEOM. Generation and evaluation of the FEOM and the settings chosen are explicitly described in *Nieradzik* [2005] and therefore left aside in this context.

The implemented FEOM evaluates the general HDMR expansion

$$f(\mathbf{x}) = f_0 + \sum_{i=1}^n f_i(x_i) + \sum_{1 \leq i < j \leq n} f_{ij}(x_i, x_j) + \dots + f_{1,\dots,n}(x_1, \dots, x_n) \quad (3.10)$$

where  $f(\mathbf{x}) \equiv f(x_1, \dots, x_n)$  is the function of the input-output mapping depending on the  $n$  input values  $x_i$ . The single functions are derived after having defined a set of non-zero so called *nominal values*  $\mathbf{x}_0 = (\bar{x}_1, \dots, \bar{x}_n)$ , with these  $f^0 := f(\mathbf{x}_0)$  (the *cut-center*) is calculated. Then, a set of monovariate functions for each nominal value is generated, by varying the  $i^{\text{th}}$  input parameter while keeping the others at their nominal values such that  $f^i$  can be evaluated along the so called *cut*  $\mathbf{x}_i = (\bar{x}_1, \dots, \bar{x}_{i-1}, x_i, \bar{x}_{i+1}, \dots, \bar{x}_n)$ . Cuts of higher order then represent planes and hyperplanes in the domain of definition. The model behavior is measured order by order along these cuts by variation of the respective variables, leading to the representations

$$\begin{aligned} f^0 &= f(\mathbf{x}_0) \\ f^i &= f(\mathbf{x}_i) \\ f^{i,j} &= f(\mathbf{x}_i, \mathbf{x}_j) \\ &\vdots \\ f^{i_1, \dots, i_n} &= f(\mathbf{x}_{i_1}, \dots, \mathbf{x}_{i_n}) \end{aligned} \quad (3.11)$$

These functions  $f$  all have the dimension of the number of output-parameters of the basic model (the PSC/APC).  $f^0$  is a vector, the mapping of the cut-center,  $f^i$  represents a set of curves, and the functions of higher orders are

**Table 3.3:** Input and output parameter and their relation to the model species

| Input       |                          | model species        |
|-------------|--------------------------|----------------------|
| T           | Temperature              | -                    |
| RH          | Relative humidity        | -                    |
| TA          | Total Ammonia            | NH4AI + NH4AJ + NH3  |
| TN          | Total Nitrate            | NO3AI + NO3AJ + HNO3 |
| TS          | Total Sulfate            | SO4AI + SO4AJ        |
| Output      |                          |                      |
| $NH_4^+$    | aqueous ammonia          |                      |
| $NO_3^-$    | aqueous nitrate          |                      |
| $H^+$       | aqueous $H^+$            |                      |
| $SO_4^{2-}$ | aqueous sulfate          |                      |
| $HSO_4^-$   | aqueous hydrogen sulfate |                      |
| $H_2O$      | aqueous liquid water     |                      |
| $NH_3$      | gas-phase ammonium       |                      |
| $HNO_3$     | gas-phase nitric acid    |                      |

surfaces and hyper surfaces. To arrive at Equation (3.10) the following is defined:

$$\begin{aligned}
f_0 &= f^0(\mathbf{x}_0) = f(\mathbf{x}_0) \\
f_i(\mathbf{x}_i) &= f^i(\mathbf{x}_i) - f_0 \\
f_{i,j}(\mathbf{x}_i, \mathbf{x}_j) &= f^{i,j}(\mathbf{x}_i, \mathbf{x}_j) - f_i(\mathbf{x}_i) - f_j(\mathbf{x}_j) - f_0 \\
&\vdots \\
f_{i_1, \dots, i_n}(\mathbf{x}_1, \dots, \mathbf{x}_n) &= f^{i_1, \dots, i_n}(\mathbf{x}_1, \dots, \mathbf{x}_n) - \\
&\quad \sum_{j_1 < \dots < j_{n-1} \subset \{i_1, \dots, i_n\}} f_{j_1, \dots, j_{n-1}}(\mathbf{x}_{j_1}, \dots, \mathbf{x}_{j_{n-1}}) \\
&\quad - \dots - \sum_j f_j(\mathbf{x}_j) - f_0.
\end{aligned} \tag{3.12}$$

With this definition every term of an order greater than one can be considered a refinement of the sum of all terms of lower order. Table 3.3 lists the input and output parameters for the both the FEOM and the PSC/APC.

### Applied HDMR

For the current MADE the maximum order was chosen to be three, that is, the representing functions  $f_0$  to  $f_{i,j,k}$  have been stored and are loaded by the FEOM at the start of a model run. To be more precise, the functions are stored as look-up tables of the sampling points that were chosen for the HDMR along each cut. A multilinear interpolation is used to extract information for every point in the definition domain. The adjoint FEOM has been created from scratch. It solves the following equation for each of the adjoint variables  $x_i^*$ ,  $i \in [3, 4, 5]$  (temperature and humidity are diagnostic):

$$x_i^* = \sum_{z=1}^m \left[ \frac{\partial}{\partial x_i} f_i(y_z^*) + \sum_{j \neq i} \left( \frac{\partial}{\partial x_i} f_{i,j}(y_z^*) + \sum_{i \neq k \neq j} \frac{\partial}{\partial x_i} f_{i,j,k}(y_z^*) \right) \right] \quad (3.13)$$

where  $m$  is the number of adjoint output-parameters and  $y_z^*$  the adjoint output-parameter  $z$ . The gradients are then redistributed onto the gradients of the MADE species. For example for nitrate, this results in:

$$NO3AI^* = NO3AJ^* = HNO3^* = TN^* = x_4^*$$

### 3.3 Nesting

In general, a very close, i.e. high resolved, look at a the chemical state of the atmosphere in a selected region is desired. In daily forecasts these are the surroundings of the national borders of a country or its federal states or, as in the ZEPTEP-2 Campaign (a description is given in Chapter 5.2), the region around Lake Constance in southern Germany. Simulating only the region of interest alone is not useful because information inflow from outside the area can not be considered this way. Since many tropospheric constituents are long-living and can be transported over large distances, this would be a great loss of information. One would have to rely on fixed boundary values only. On the other side, simulating an area that is large enough to comprise all necessary sources with the desired high resolution is not feasible due to computational limitations. To overcome this predicaments, the technique of nesting is applied. Here, simulations are conducted on a grid with large extent but only low horizontal resolution. It is called coarse domain or *Nest 0* (N0) with boundary values as described in 3.1.2. A region around the area of interest is then defined within this mother domain. The boundary values of this daughter domain (N1) are now interpolated from the mother domains respective grid cells. That way, not only reasonable boundary values are provided to the daughter grid, but

also do they have a temporal resolution of that of the mother domain. Initial values for N1 are taken from the preceding N1 simulation to preserve the high resolution information. This domain N1 can now be mother to a nest N2 and so forth. A description of one-way nesting with the EURAD-CTM can be found in *Jakobs et al.* [1995]. Moreover, this technique has proven to be applicable in numerous campaign simulations (especially *Memmesheimer et al.* [2004]) and the application in the context of data assimilation is documented in *Elbern and Strunk* [2007].

### 3.4 Observation operators

In Data Assimilation the model's calculated values - the background field - and its trustworthiness are weighted against the measurements and their errors. In most cases the measured species or their units or even both do not concur. As shown in Table 3.2 there are 37 aerosol species and particle properties in MADE. Concentrations of several different aerosol components are separated into the three modes as well as particle number and volume. Instrumental measurements generally display what they are able to measure in suitable units, e.g.  $PM_{10}$  is the overall sum of aerosol particles of any size smaller than 10  $\mu m$  and its measurement value thus is expressed as overall mass per volume ( $\mu g/m^3$ ). Many satellite instruments, like the passive nadir-radiometers introduced in this chapter measure along a line-of-sight thus gathering information about a column they are focused on without permitting direct conclusions on the vertical distribution within this column. In that way, only two dimensional information can be obtained whereas the model produces three dimensional fields. To be able to compare this kind of information a mapping needs to be introduced into the assimilation system to produce a so called model equivalent, i.e. a pendant to the measurement containing a value of the same unit and the same type resembling what the instrument would have measured if the model background would have been real. This can be done rather easily by simple summation over the aerosol components and their respective diameters, as with  $PM_x$ , or it can require the large effort of operating a radiative transfer model as it is the case with the SYNAER retrieval algorithm. Generally, each different kind of measurement needs its own mapping. In terms of data assimilation these mappings are called *Observation Operator*, *H-Operator*, or *Forward Operator*. This section illuminates the generation of the different H-operators used in this thesis.

### 3.4.1 Size integrated observations

Size integrated observations are observations that deliver a total of number or mass (as  $PM_x$ ) concentrations within a certain range of diameters. In section 3.2 the log-normal trimodal characteristics of the aerosol size-distribution has been introduced. Based on the formulation of the  $0^{th}$  and  $3^{rd}$  moments (equations 3.6 and 3.7) the *number median diameter*  $D_{N,i}$  can be calculated for each mode  $i$  by

$$D_{N,i} = \sqrt[3]{\frac{\mathcal{M}_{3,i}}{\mathcal{M}_{0,i}} e^{-9/2 \ln^2 \sigma_i}} \quad (3.14)$$

As described, the distribution within a single mode is expressed by a Gaussian around the median diameter. To get the fraction of the total of number or mass that is covered by a certain interval of diameters the *Error Function*

$$erf(x) = \frac{2}{\sqrt{\pi}} \int_0^x e^{-t^2} dt \quad (3.15)$$

is applied, which, in its original notation, delivers the integral from 0 to  $x$  of a Gaussian centered at zero with  $\sigma = 1$ . Thus,  $erf(\infty) = 0.5$ . Concerning the aerosol size distribution the *error function* has to be transformed to an arbitrary center and onto a log-normal scale. Following *Seinfeld and Pandis* [1998], the function  $F_i$  yields the desired result for mode  $i$ , from diameter 0 to  $x$ , of a Gaussian centered at  $D_{N,i}$  with a geometric standard deviation of  $\sigma_i$

$$F_{N_i}(x) = \frac{1}{2} \left( 1 + erf \left( \frac{\ln(x/D_{N,i})}{\sqrt{2} \ln(\sigma_i)} \right) \right) \quad (3.16)$$

#### Particle Number Density

Modern instruments used for in-situ campaign measurements are capable of determining the number of particles per volume with a diameter that lies within a specified range. These diameters may range from  $0.005\mu m$  to  $3.0\mu m$ , as for the CPC (Condensation Particle Counter) applied in the ZEPTEP-2 campaign, or there may be a threshold value beyond all particles are counted. Since they don't need long integration or gathering sequences, these measurements can be assigned to a specific point in time, instead of being an average over a certain period.

To calculate the integral from a lower to an upper limit,  $x_l$  and  $x_u$ , respectively, Equation 3.16 simply has to be applied for each mode  $i$  and for both, upper and lower limit, and multiplied with its overall particle number  $N_i$ . The

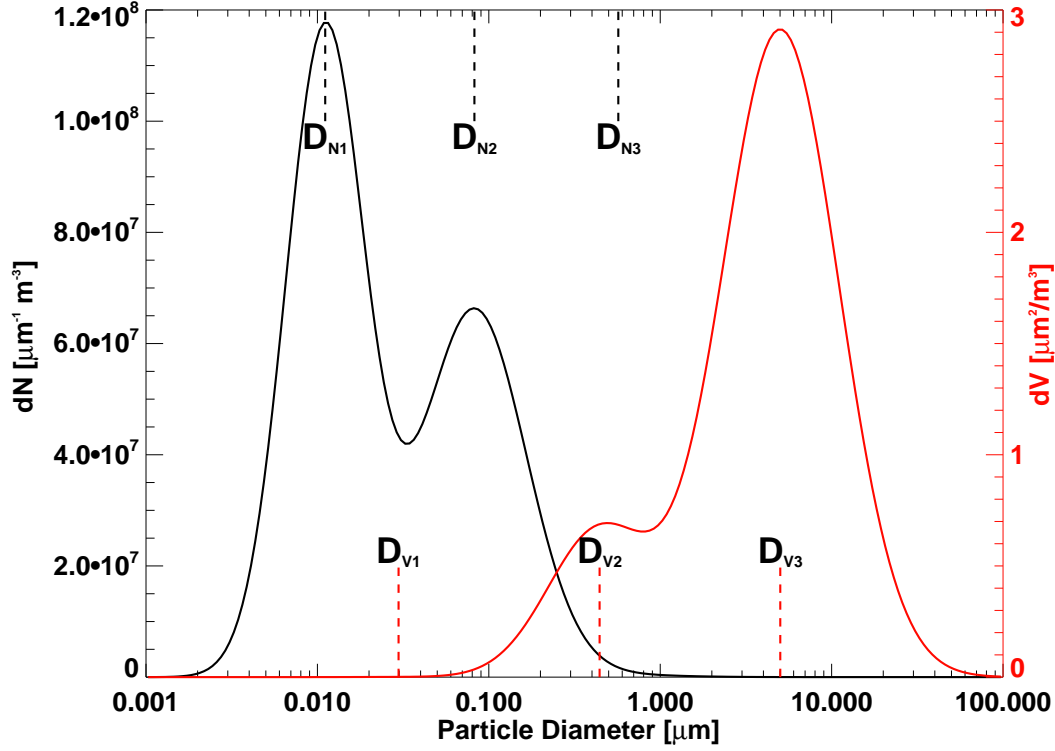


**Figure 3.3:** Log-normal representation of number (black) and volume distribution (red) of an arbitrary set of moments  $\mathcal{M}_{0,i}$  and  $\mathcal{M}_{3,i}$ . Number median diameters are denoted as  $D_{N,i}$ , volume median diameters as  $D_{V,i}$ ,  $i$  indicates the mode.

difference represents the equivalent to the measured *particle number density*  $PND_{x_l, x_u}$

$$PND_{x_l, x_u} = \sum_{i=1}^3 N_i [F_i(x_u) - F_i(x_l)] \quad (3.17)$$

The black line in Figure 3.3 shows the number distribution for an arbitrary but reasonable set of  $\mathcal{M}_{0,i}$  and  $\mathcal{M}_{3,i}$  along with the number median diameters  $D_{N,i}$ . It is obvious that  $PND$  is by the accumulation and, even more, the Aitken mode.

## Particulate Matter

Particulate matter generally is given in values of mass concentration, i.e.  $\mu\text{g}/\text{m}^3$ , referring to a maximum particle's diameter in  $\mu\text{m}$ . That is, a value of

$PM_x$  displays the overall aerosol mass as summation of the components of all particles of a diameter lower than or equal to  $x \mu m$  within a certain volume. This is insensitive to the chemical composition of the aerosols. A calculation of a  $PM_x$  value will thus be the sum of the individual integrations over each of the three modes with an upper limit of  $x \mu m$ . For each mode a volume median diameter can be derived directly from Equations 3.7 and 3.14

$$\ln(D_{V,i}) = \ln(D_{N,i}) + 3\ln^2(\sigma_i) \quad (3.18)$$

with the same geometric standard deviation of  $\sigma_i$  as for the number densities, and  $M_i$  being the overall mass per grid cell in mode  $i$

$$M_i = \sum_{l=1}^L \frac{c_{l,i}}{\rho_l} \quad (3.19)$$

where  $\rho_l$  is the specific density of species  $l$  and  $c_{l,i}$  its current mass concentration in mode  $i$ . Replacing the number median diameter  $D_{N,i}$  by  $D_{V,i}$  in Equation 3.16 yields the fraction of the Gaussian w.r.t.  $D_{V,i}$  for each mode:

$$F_{V_i}(x) = \frac{1}{2} \left( 1 + \operatorname{erf} \left( \frac{\ln(x/D_{V,i})}{\sqrt{2} \ln(\sigma_i)} \right) \right) \quad (3.20)$$

and, thus, an overall  $PM_x$  by

$$PM_x = \sum_{i=1}^3 M_i F_{V_i}(x) \quad (3.21)$$

The red line in Figure 3.3 displays the log-normal volume distribution of an arbitrary set of  $\mathcal{M}_{0,i}$  and  $\mathcal{M}_{3,i}$  along with the volume median diameters  $D_{V,i}$ . Here, the coarse mode is dominating while the Aitken mode is immaterial. This has to be treated with care. The median diameters can vary largely and an observation of  $PM_{0.5}$  for example would predominantly measure the accumulation mode here, because the coarse mode is already out of range.

### 3.4.2 SYNAER - SYNERgetic AEROSOL Retrieval

The SYNAER algorithm (*Holzer-Popp et al. [2002a]* and *Holzer-Popp et al. [2002b]*) is a synergetic retrieval method that makes use of the informations gathered by two instruments to gain information beyond the original purpose of each of the instruments involved. In this case the algorithm is tailored to exploit both an instrument with high spectral resolution and one radiometer

**Table 3.4:** List of satellite instruments the SYNAER retrieval has been adapted to. Operational cycles taken from <http://earth.esa.int>

| Satellite | Instruments  | Resolution<br>[ $km^2$ ]    | Operation<br>Cycle    |
|-----------|--|-----------------------------|-----------------------|
| ERS-2     | GOME (Global Ozone Monitoring Experiment)<br>ATSR-2 (Along Track Scanning Radiometer)                      | 40 to 320 x 40<br><br>1 x 1 | 04/1995 to<br>12/2008 |
| ENVISAT   | SCIAMACHY (Scanning Imaging Absorption Spectrometer for Atmospheric CHartographY)<br>AATSR (Advanced ATSR) | 32 x 215<br><br>1 x 1       | since<br>03/2002      |
| MetOp-A   | GOME-2<br>AVHRR (Advanced Very High Resolution Radiometer)   | 80/160 x 40<br>1 x 1        | since<br>10/2006      |

with high spatial resolution. The radiometer's observations are used for cloud screening, i.e. to determine whether a pixel can be used for AOT-retrieval, in the first place and, if successful, to calculate the pixel's AOT values at a wavelength of 550 nm and spectral surface brightness for a set of 40 predefined aerosol mixtures (see table 3.6 for a detailed list of selected mixtures). Subsequently, a least-square-fit against the spectrometer measurement is conducted for each of these mixtures to determine the most likely composition of the tropospheric aerosols. The retrieval results used in this thesis have a spatial resolution of  $60 \times 30 km^2$ .

The SYNAER retrieval algorithm has been adapted to different combinations of different, yet similar, instruments aboard various satellites. Table 3.4 lists the possible applications.

To avoid confusion, *SYNAER retrieval* always addresses the retrieval algorithm that extracts aerosol optical thicknesses from instrument signals whereas *SYNAER-H-Operator* adverts to the forward operator that generates an equivalent from the model state.

**Table 3.5:** SYNAER AOT types as used within retrieval and as delivered in data product according to Holzer-Popp et al. [2008]

| SYNAER AOT type | Explanation                | Description   |
|-----------------|----------------------------|---|
| WASO            | Water SOLubles             | water solubles                                      |
| INSO            | water INSOLubles           | mineral dust (high hematite content)                |
| INS2            | water INSolubles 2         | mineral dust (low hematite content)                 |
| DISO            | DIEsel SOot                | soot from fossile fuel combustion processes         |
| BISO            | BIomass SOot               | soot from biomass burning                           |
| SSAM            | Sea Salt Acc. Mode         | sea salt from sea spray (accumulation mode)         |
| SSCM            | Sea Salt Coa. Mode         | sea salt from sea spray (coarse mode)               |
| MITR            | MInerals TRans-ported high | transported coarse minerals (high hematite content) |
| MILO            | MInerals transported LOW   | transported coarse minerals (low hematite content)  |

### SYNAER Aerosol Optical Thickness

The SYNAER retrieval delivers BLAOT (Boundary Layer Aerosol Optical Thickness) for 40 predefined combinations of nine intrinsic AOT types, which are explained in table 3.5. The specifications for these intrinsic types are based on the optical properties of aerosols. These do not exactly match the criteria of distinction applied when MADE was created, where species were selected by their chemical properties and their origin. Thus, not all of these nine SYNAER retrieval AOT types can be used for data assimilation in a direct way. For the use with the SYNAER-H-Operator within EURAD-IM the SYNAER AOT types have been reduced to five, summed up in table 3.7. Since the EURAD-IM did not contain sea salt in accumulation mode when the SYNAER-H-Operator was built, there is no adequate forward mapping for SSAM, and, thus, these measurements have to be omitted. The offline data preprocessor *PREP*, which is used to provide observations for the EURAD-IM is performing these mappings. It also splits the measurement values that are delivered as AOT for a certain mixture into the EURAD-IM AOT types. The percentage listed in 3.6 for each SYNAER AOT type refers to the overall AOT, thus, the measurement AOT is the sum over all partial AOTs.

*Table 3.6: Predefined mixtures within the SYNAER retrieval.*

| No. | Name                      | rH<br>[%] | Hght<br>[km] | Composition [%] |      |      |      |      |      |      |      |      |    |
|-----|---------------------------|-----------|--------------|-----------------|------|------|------|------|------|------|------|------|----|
|     |                           |           |              | WASO            | INSO | INS2 | SSAM | SSCM | DISO | BISO | MITR | MILO |    |
| 1   | Pure Watersoluble a       | 50        | 0-2          | 100             |      |      |      |      |      |      |      |      |    |
| 2   | Continental Ia            | 50        | 0-2          | 95              | 5    |      |      |      |      |      |      |      |    |
| 3   | Continental IIa           | 50        | 0-2          | 90              | 10   |      |      |      |      |      |      |      |    |
| 4   | Continental IIIa          | 50        | 0-2          | 85              | 15   |      |      |      |      |      |      |      |    |
| 5   | Maritime Ia               | 50        | 0-2          | 30              |      |      | 70   |      |      |      |      |      |    |
| 6   | Maritime IIa              | 50        | 0-2          | 30              |      |      | 65   | 5    |      |      |      |      |    |
| 7   | Maritime IIIa             | 50        | 0-2          | 15              |      |      | 85   |      |      |      |      |      |    |
| 8   | Maritime IVa              | 50        | 0-2          | 15              |      |      | 75   | 10   |      |      |      |      |    |
| 9   | Polluted Watersoluble I   | 50        | 0-2          | 90              |      |      |      |      |      | 10   |      |      |    |
| 10  | Polluted Watersoluble II  | 50        | 0-2          | 80              |      |      |      |      |      | 20   |      |      |    |
| 11  | Polluted Continental Ia   | 50        | 0-2          | 80              | 10   |      |      |      |      | 10   |      |      |    |
| 12  | Polluted Continental IIa  | 50        | 0-2          | 70              | 10   |      |      |      |      | 20   |      |      |    |
| 13  | Polluted Maritime Ia      | 50        | 0-2          | 40              |      |      | 45   | 5    | 10   |      |      |      |    |
| 14  | Polluted Maritime IIa     | 50        | 0-2          | 30              |      |      | 40   | 10   | 20   |      |      |      |    |
| 15  | Desert Outbreak Ia        | 50        | 2-4          | 25              |      |      |      |      |      |      |      | 75   |    |
| 16  | Desert Outbreak IIa       | 50        | 3-5          | 25              |      |      |      |      |      |      |      | 75   |    |
| 17  | Desert Outbreak IIIa      | 50        | 4-6          | 25              |      |      |      |      |      |      |      | 75   |    |
| 18  | Biomass Burning Ia        | 50        | 0-3          | 85              |      |      |      |      |      | 15   |      |      |    |
| 19  | Biomass Burning IIa       | 50        | 0-3          | 70              |      |      |      |      |      | 30   |      |      |    |
| 20  | Biomass Burning IIIa      | 50        | 0-3          | 55              |      |      |      |      |      | 45   |      |      |    |
| 21  | Pure Watersoluble b       | 80        | 0-2          | 100             |      |      |      |      |      |      |      |      |    |
| 22  | Continental Ib            | 50        | 0-2          | 95              |      | 5    |      |      |      |      |      |      |    |
| 23  | Continental IIb           | 50        | 0-2          | 90              |      | 10   |      |      |      |      |      |      |    |
| 24  | Continental IIIb          | 50        | 0-2          | 85              |      | 15   |      |      |      |      |      |      |    |
| 25  | Maritime Ib               | 80        | 0-2          | 30              |      |      | 70   |      |      |      |      |      |    |
| 26  | Maritime IIb              | 80        | 0-2          | 30              |      |      | 65   | 5    |      |      |      |      |    |
| 27  | Maritime IIIb             | 80        | 0-2          | 15              |      |      | 85   |      |      |      |      |      |    |
| 28  | Maritime IVb              | 80        | 0-2          | 15              |      |      | 75   | 10   |      |      |      |      |    |
| 29  | Polluted Watersoluble Ib  | 80        | 0-2          | 90              |      |      |      |      |      | 10   |      |      |    |
| 30  | Polluted Watersoluble IIb | 80        | 0-2          | 80              |      |      |      |      |      | 20   |      |      |    |
| 31  | Polluted Continental Ib   | 50        | 0-2          | 80              |      | 10   |      |      |      | 10   |      |      |    |
| 32  | Polluted Continental IIb  | 50        | 0-2          | 70              |      | 10   |      |      |      | 20   |      |      |    |
| 33  | Polluted Maritime Ib      | 80        | 0-2          | 40              |      |      | 45   | 5    | 10   |      |      |      |    |
| 34  | Polluted Maritime IIb     | 80        | 0-2          | 30              |      |      | 40   | 10   | 20   |      |      |      |    |
| 35  | Desert Outbreak Ib        | 50        | 2-4          | 25              |      |      |      |      |      |      |      |      | 75 |
| 36  | Desert Outbreak IIb       | 50        | 3-5          | 25              |      |      |      |      |      |      |      |      | 75 |
| 37  | Desert Outbreak IIIb      | 50        | 4-6          | 25              |      |      |      |      |      |      |      |      | 75 |
| 38  | Biomass Burning Ib        | 80        | 0-3          | 85              |      |      |      |      |      | 15   |      |      |    |
| 39  | Biomass Burning IIb       | 80        | 0-3          | 70              |      |      |      |      |      | 30   |      |      |    |
| 40  | Biomass Burning IIIb      | 80        | 0-3          | 55              |      |      |      |      |      | 45   |      |      |    |

**Table 3.7:** Mapping of the SYNAER AOT types onto a reduced set of EURAD-IM SYNAER-H-Operator AOT types for the use in data assimilation. Tolerances are maximum values for which the H-Operator is valid

| EURAD-IM AOT type | SYNAER AOT type | Tolerance |
|-------------------|-----------------|-----------|
| AOTWASO           | WASO            | 0.7       |
| AOTINSO           | INSO + INS2     | 0.7       |
| AOTSOOT           | DISO + BISO     | 2.0       |
| AOTSEAS           | SSCM            | 1.0       |
| AOTDUST           | MITR + MILO     | 2.0       |

For example: A measurement datum contains (among other) the following information:

Mixture No. 14  
AOT 0.1

Using table 3.5 this measurement of mixture 14 (Polluted Maritime IIa) can be translated into four measurements of the contributing SYNAER retrieval AOT types

$$\begin{aligned} \text{AOT(WASO)} &= 0.03 \text{ (30\%)} \\ \text{AOT(SSAM)} &= 0.04 \text{ (40\%)} \\ \text{AOT(SSCM)} &= 0.01 \text{ (10\%)} \\ \text{AOT(DISO)} &= 0.02 \text{ (20\%)} \end{aligned}$$

which in subsequently must be mapped onto the H-Operator's AOT types. According to table 3.7, this leads to three individual measurements of

$$\begin{aligned} \text{AOTWASO (WASO)} &= 0.03 \\ \text{AOTSEAS (SSCM)} &= 0.01 \\ \text{AOTSOOT (DISO+BISO)} &= 0.02 \end{aligned}$$

where, as explained above, accumulation mode sea salt (SSAM) is omitted. These aerosol optical thicknesses are calculated for a layer of a certain thickness also given in the description of the mixtures (table 3.6). This means, that the given AOT value only refers to the model layers involved. The retrieval product has already been corrected for additional contribution of aerosols in higher and lower layers. In the above example the SYNAER-H-Operator has to be applied for three AOT types (AOTWASO, AOTSEAS, AOTSOOT) for all model layers from 0m to 2000m (i.e. level 1 to 15). This is performed taking into account

**Table 3.8:** List of types of SYNAER aerosol optical thicknesses and the EURAD-IM contributing species separated by mode. See Table 3.2 for a detailed description of EURAD-IM Species

| SYNAER<br>AOT type | EURAD-IM    |  |              |
|--------------------|-------------|--|--------------|
|                    | Aitken mode | Accumulation mode  | Coarse mode  |
| AOTWASO            |             | <i>AO4AJ</i><br><i>NH4AJ</i><br><i>NO3AJ</i><br><i>H2OAJ</i><br><i>SOA</i> |              |
| AOTINSO            |             | <i>ORGPAJ</i><br><i>P2.5AJ</i>   | <i>ANTHA</i> |
| AOTSOOT            | <i>ECI</i>  | <i>ECJ</i>   |              |
| AOTSEAS            |             |  | <i>SEAS</i>  |
| AOTDUST            |             |  | <i>SOILA</i> |

the EURAD-IM species concentrations of the relevant layer and the relevant modes. Table 3.8 lists the EURAD-IM aerosol species that contribute to each of the components of the reduced set of AOT types.

### Satellite footprints

In comparison to general in-situ instruments, space borne instruments basically determine optical properties of a column or a cone along the line of sight of the sensor, leaving a footprint as the area of validity of the measurement value. Since their orbits are very high compared to the thickness of the troposphere - e.g. ENVISAT travels at an altitude of about 790 km, while the tropopause lies in the region between 8 and 14 km - these columns are treated as being strictly vertical, i.e. the horizontal area taken as representative for a measurement is the same on the surface as in an altitude of 14 km, and the curvature of the earth and, thus, the atmosphere is neglected. For the SYNAER Retrieval as the only remote sensing dataset in this thesis with a maximum height of 6 km, this results in an error of about 0.25 % of the contributing air volume. This is well below the errors of both, measurement and model background. Figure 3.4 shows a SYNAER retrieved AOT footprint (grey shaded area) on the rectangular horizontal grid of the EURAD-IM. This footprint covers 16

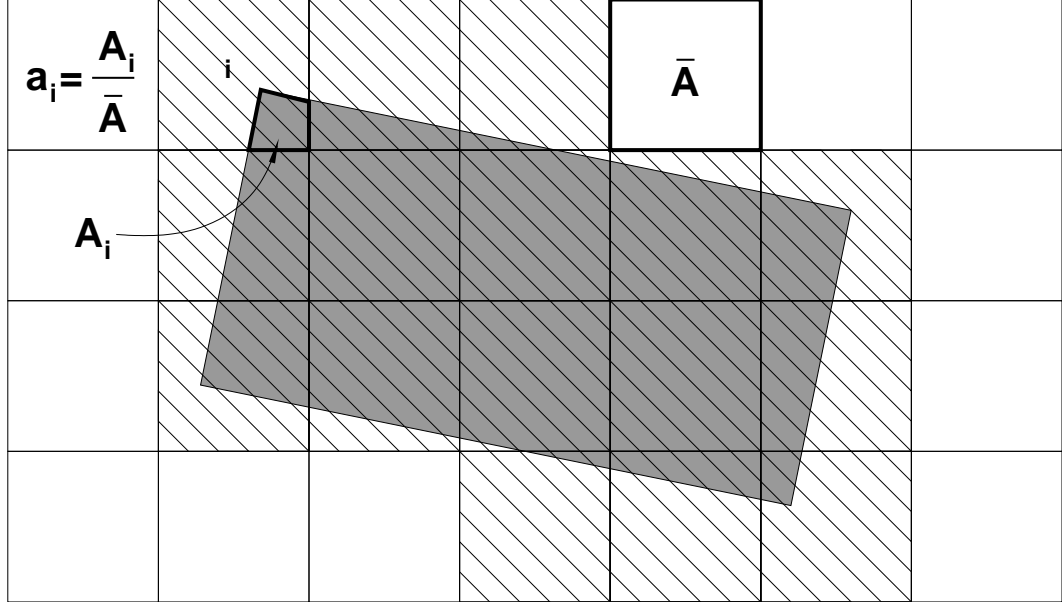


**Figure 3.4:** The Footprint-H-Operator generates a representative column of the size of the satellite footprint (shaded area) by layer and species wise interpolation from all columns involved (pattern filled squares). The EURAD-IM uses equidistant grids, so all cells have a square floor of the same size  $\bar{A}$ .  $a_i$  represents the weight of the concentrations of cell  $i$ . Interpolation is then accomplished as described in equation 3.22.

model grid cells, or rather columns, at least in part (pattern filled cells) and, since the measurement contains the AOT of the whole footprint's area, all grid cells covered have to be taken into account for the calculation of the appropriate model equivalent. For each covered cell  $i$  the fractional coverage  $a_i \in [0, 1]$  by the footprint is calculated. Then, for each layer  $k$  one representative cell of the size of the footprint is calculated containing the weighted mean concentration  $\bar{c}_{k,l}$  for each aerosol species  $l$  as follows

$$\bar{c}_{k,l} = \frac{\sum_i a_i \cdot c_{i,k,l}}{\sum_i a_i} \quad (3.22)$$

This can be considered the *Footprint-H-Operator*. The *SYNAER-H-Operator* now delivers a model equivalent AOT based on the generated weighted mean taking into account the vertical range of validity of the retrieval. Consequently, an *adjoint Footprint-H-Operator* is needed to remap the derived gradient from measurement space to the EURAD-IM species and grid cells. This way, model developed patterns among the affected cells are preserved. Calculating the

AOTs is a very demanding task consuming a lot of CPU time. To first calculate the AOT of each of the model columns covered and then calculate a weighted mean AOT for the footprint, which is more close to the way the retrieval works, would multiply the effort by the number of columns involved. Column model tests have shown, that commutativity of these operators is given with only small aberration. This is an important point, because it also shows that the *SYNAER-H-Operator* is sufficiently linear.

## CHAPTER 4

---

### Background Error Covariance Modeling

---

Taking a look at three dimensional modeled fields of atmospheric constituents they appear to be more or less smooth in terms of the variations of, say, concentrations. Rarely, isolated peaks that differ extremely from the neighboring grid cells will be found. These effects even decrease with higher grid resolution. This reflects the general behavior of atmospheric chemistry, where particles or chemical compounds are emitted or formed over a certain period of time and then undergo aging, chemical alteration, and advection within a coherent area. If there is, for example, a dust outbreak following continuous winds and elevated mineral dust values are observed, then it is very likely that similarly elevated values will be found in the vicinity. Or, the other way around, it is very unlikely, not to find them. This implicates a spatial correlation between the grid cells. Another type of correlation is species to species correlation. This information is encoded in  $\mathbf{B}$ , the Background Error Covariance Matrix (BECM), introduced in Equation 2.8 as a weighting matrix for the trustworthiness of the model. An error covariance matrix  $\mathbf{B}$  can alternatively be written as

$$\mathbf{B} = \mathbf{\Sigma} \mathbf{C} \mathbf{\Sigma} \quad (4.1)$$

where  $\mathbf{\Sigma}$  is a diagonal matrix containing the standard deviations of each species in each grid cell, and  $\mathbf{C}$  denoting the correlation matrix with  $C_{ij} = E[(\epsilon_i - E(\epsilon_i))(\epsilon_j - E(\epsilon_j))]/\sigma_i\sigma_j ; i \neq j$  and  $C_{ii} = 1$ . A complete BECM  $\mathbf{B}$  is of the size of  $(n_{spc} \cdot n_{cells})^2$ , which in terms of the aerosols in MADE and the European domain introduced in the following would lead to  $(37 \cdot 95 \cdot 85 \cdot 23)^2 \approx$

$47 \cdot 10^{12}$ . Taking into account that  $\mathbf{B}$  is symmetrical this would still mean an estimated computer-memory storage-demand of almost  $100 TB$ . Even with the prospect of fast growing storage availability, this will not be feasible.

## 4.1 Processing of Background Error Covariances

Following the diffusion approach by *Weaver and Courtier* [2001] the entries of  $\mathbf{B}$  can be processed in a way that avoids large matrix multiplications to gain  $\nabla_{x_0} J^b$  and that reduces the demand of storage for  $\mathbf{B}$  significantly. The following subsections will give an overview of this concept.

### 4.1.1 The incremental formulation of the costfunction

Essential in this approach is the fact, that the computation of  $\mathbf{B}^{-1}$  as defined in the background part of the cost function (Equation 2.8) and the gradient (Equation 2.10) is not necessary. With  $\mathbf{B}$  being non-singular, a new set of control variables can be defined as

$$\mathbf{v}_0 := \mathbf{B}^{-1/2} \delta \mathbf{x}_0 \quad (4.2)$$

with the *increment*  $\delta \mathbf{x}_0 = \mathbf{x}_0 - \mathbf{x}^b$ , this can be rewritten to

$$\mathbf{x}_0 = \mathbf{B}^{1/2} \mathbf{v}_0 + \mathbf{x}^b. \quad (4.3)$$

This yields a simplified representation of the gradient w.r.t.  $\mathbf{v}_0$  when replacing  $(\mathbf{x}_0 - \mathbf{x}^b)$  by  $\delta x = \mathbf{B}^{1/2} \mathbf{v}_0$

$$\nabla_{\mathbf{v}_0} J^b = \nabla_{\mathbf{v}_0} \frac{1}{2} (\mathbf{B}^{1/2} \mathbf{v}_0)^T \mathbf{B}^{-1} (\mathbf{B}^{1/2} \mathbf{v}_0) = \nabla_{\mathbf{v}_0} \frac{1}{2} (\mathbf{v}_0^T \mathbf{v}_0) = \mathbf{v}_0 \quad (4.4)$$

For the observational part, the canonical scalar product is taken into account, considering  $\delta \mathbf{x}_0$  a small variation, a variation of  $J^O$  can then be transformed as in Equation 2.4 via

$$\begin{aligned} \delta J^O &= \langle \nabla_{\mathbf{x}_0} J^O, \delta \mathbf{x}_0 \rangle = \langle \nabla_{\mathbf{x}_0} J^O, \mathbf{B}^{1/2} \mathbf{v}_0 \rangle \\ &= \langle \mathbf{B}^{T/2} \nabla_{\mathbf{x}_0} J^O, \mathbf{v}_0 \rangle \end{aligned} \quad (4.5)$$

leading to the new formulation of the gradient of  $J^o$  w.r.t.  $\mathbf{v}_0$

$$\nabla_{\mathbf{v}_0} J^o = \mathbf{B}^{T/2} \nabla_{\mathbf{x}_0} J^o \quad (4.6)$$

Remarkably,  $\mathbf{v}_0$  is both, vector of control variables and background gradient. The first iteration of the minimisation algorithm is started from background values resulting in  $\mathbf{v}_0 = 0$  and making the computation of 4.2 obsolete. Moreover, starting values for the next iteration  $it + 1$  are created adding the increment from 4.2 to the background by

$$\mathbf{x}_0^{it+1} = \mathbf{x}^b + \delta x^{it} = \mathbf{x}^b + \mathbf{B}^{1/2} \mathbf{v}_0 \quad (4.7)$$

with  $\mathbf{v}_0 \equiv \mathbf{v}_0^{it}$  being the gradient of the preceding iteration. This way the demanding computation of  $\mathbf{B}^{-1/2}$  is avoided.

### 4.1.2 The diffusion approach

The preceding subsection has shown an elegant way to circumvent the calculation of  $\mathbf{B}^{-1}$ . Now the issue of the size of  $\mathbf{B}$  has to be solved. Still following *Weaver and Courtier* [2001] the diffusion paradigm will be described without going too much into details. They show that the matrix-vector multiplication  $\mathbf{B}^{1/2} \mathbf{x}$  can be replaced by the application of a diffusion operator  $\mathbf{L}(\mathbf{x})$ , under the assumption that the spatial correlations can be described by a Gaussian function. Here,  $\mathbf{L}$  calculates the solution of a two dimensional diffusion equation of the type

$$\frac{\partial \Psi}{\partial t} - \kappa \nabla^2 \Psi = 0. \quad (4.8)$$

For the formulation of the diffusion paradigm, the *correlation length*  $L$  is introduced in dependence of the diffusion coefficient  $\kappa$  as

$$L = \sqrt{2\kappa\tau} \quad (4.9)$$

with  $\tau$  being the diffusion time. The approach rests on a Gaussian model formulation of  $B(r)$  being the covariance in the distance  $r$  from the grid cell at  $r = 0$  taking influence by

$$B(r) = B(0) \cdot e^{-\frac{r^2}{2L^2}} \quad (4.10)$$

and  $B(0)$  the covariance at  $r = 0$  which is the variance. Assuming that  $\mathbf{B}$  is known then  $L_{ij}$  can be calculated as the correlation length between two neighboring grid cells  $i$  and  $j$  at  $r = 0$  and  $r = 1$  (in units of grid spacing) as

$$L_{ij} = \left( 2 \ln \left( \frac{B(0)}{B(1)} \right) \right)^{1/2} \quad (4.11)$$

where  $B(0) = 1/2(B_{ii} + B_{jj})$  to ensure symmetry. With the knowledge of  $L_{ij}$  the diffusion coefficients denoted in Equation 4.9 can be computed acting as diffusion coefficients at the wall between the two grid cells:

$$\kappa_{ij} = \frac{L_{ij}^2}{2\tau} \quad (4.12)$$

where  $\tau$  chosen such, that  $\max(\kappa_{ij}) \leq 0.2$  to ensure stability. An information diffusion is then performed before and after minimisation using these  $\kappa$  using  $\tau/2$  time steps each. This kind of information processing leaves  $\mathbf{B}$  with approximately three times the number of grid cells for each species. One for the neighbors to the north, to the east, and to the top, except for cells at the top layer, or at northern or eastern boundaries. Alternatively, as it is applied in this study, the vertical diffusion coefficients can be taken from the physical vertical diffusion, computed by the meteorological driver MM5. Another advantage of the diffusion approach is that the infrastructure - a numerical diffusion operator - is already existing.

## 4.2 Obtaining $\mathbf{B}$

As described, the BECM can be a huge matrix when fully assigned. First of all, the species to species correlations have been abandoned, to reduce the magnitude of  $\mathbf{B}$ . Most of the measurements affect all aerosol species anyway, as they are bulk measurements like  $PM_{10}$  or overall aerosol optical thicknesses. This leaves a block-diagonal matrix describing the spatial covariances of each single species.

### 4.2.1 Isotropic and homogeneous

The simplest method that can be chosen without much preparations is the isotropic and homogeneous BECM, where

- **isotropic** means, that horizontal correlation length is independent of direction and
- **homogenous** that correlation length is the same for every grid cell.

Then, only one information is needed per species: The horizontal correlation length from which a single diffusion coefficient can be calculated.

### 4.2.2 Ensemble calculations

The most elaborate way to get a reasonable, fully assigned BECM is an ensemble simulation. A careful choice of the parameters perturbed has to be taken in advance and especially their number, since each ensemble member means an additional set of complete forward simulations. The number of simulations  $N_s$  needed can be calculated as

$$N_s = \prod_i^M (P_i + 1) \quad (4.13)$$

Where  $M$  is the number of perturbed parameters and  $P_i$  the number of perturbations of parameter  $i$ . The addend  $+1$  signifies the unperturbed state of each parameter. As indicated in *Evensen* [1994] the entries of  $\mathbf{B}$  for a single species can then be calculated as

$$\mathbf{B}_{ij} = \frac{1}{N_s - 1} \sum_{n=1}^{N_s-1} (x_i^n - \bar{x}_i) (x_j^n - \bar{x}_j) \quad (4.14)$$

where  $i, j$  indicate two grid cells,  $x_i^n$  the species value in  $i$  on the  $n^{\text{th}}$  ensemble simulation, and  $\bar{x}_i$  the value of the simulation free of perturbations. The processing of  $\mathbf{B}$  can then be conducted using the diffusion approach as described above.

### 4.2.3 The NMC - method

Another method to generate  $\mathbf{B}$  is the so called NMC - method, named after the National Meteorological Center of the USA in Washington (now National Center for Environmental Prediction; NCEP), introduced by *Parrish and Derber* [1992], which was originally used in meteorological forecasts. It is closely related to the ensemble method. Due to the high computational demand at that time the BECM was static and it was assumed, that non-diagonal elements could be zeroed, i.e. the matrix only contained the variances. It was built of a set of differences between 24h forecast and analysis-initialised forecast at 0.00 UTC of each day in January 1991. With not much additional effort, the non-diagonal elements of  $\mathbf{B}$  can be obtained from the same dataset using the same method. Its strength compared to the ensemble method is that it is very run time saving. Today's forecast models usually predict the chemical composition of the atmosphere for 72 hours or more. Thus, every point in time is covered by at least three forecasts. One starting at e.g. 0.00 h of the same day, another one 24 hours earlier and so on. These different forecasts are based on

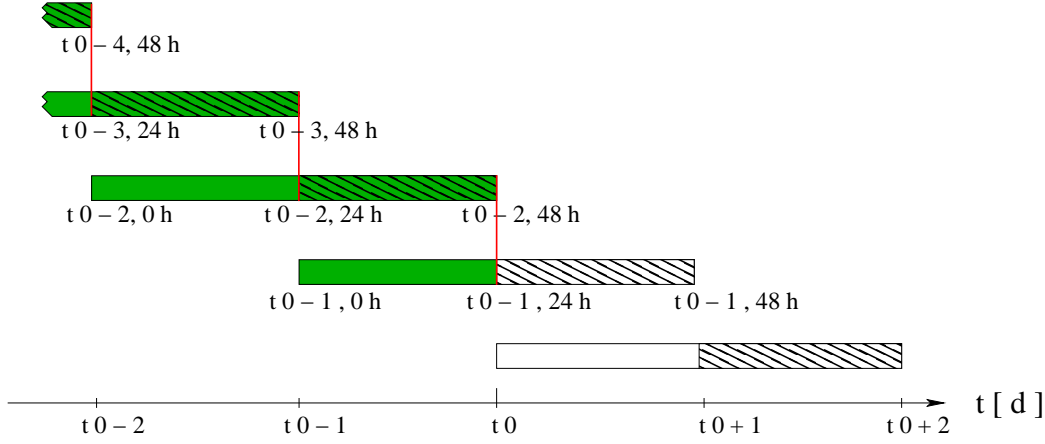


**Figure 4.1:** Schematic overview of the NMC method. Horizontal bars indicate 48 hour simulations that are past (green) and future (colorless). Red vertical bars indicate points in time when the differences are calculated.

different initial fields, i.e. the newest available information at starting time. These different forecasts can be considered to be a very small ensemble where perturbation is arranged by different initial fields. The covariances are then built from the differences of all the preceding forecasts at the same point in time for  $K$  days in the past. Figure 4.1 displays how the differences of the two forecasts are obtained, indicated by the red bars. Here, the differences can be calculated for every hour of the day. A 72 hour forecast produces three different values for each time step and, thus, there will be three differences each. The calculation of the covariances is quite similar to the way in the ensemble method:

$$\mathbf{B}_{i,j} = \frac{1}{K} \sum_{n=1}^K \frac{2}{M(M-1)} \sum_{1 \leq s < t \leq M} \left( x_i^{T(s,n)} - x_i^{T(t,n)} \right) \left( x_j^{T(s,n)} - x_j^{T(t,n)} \right) \quad (4.15)$$

where  $\mathbf{B}_{i,j}$  indicates the covariance of two grid cells ( $i \neq j$ ),  $K$  the number of days accounted for,  $M$  number of forecasts available for point in time, and  $T(u, n)$  indicating starting day of forecast simulation as  $t_s = t_0 - (n + u)$  (see Figure 4.1 as reference) and forecast hour  $(u - 1) \cdot 24 + h_0$  where  $d_o$  is the day and  $h_0$  the hour for the final day for which  $\mathbf{B}$  is generated (which might well be today). There are two major differences to the original use of this method. First, the original  $\mathbf{B}$  by was designed to get an estimate of the model's background error and to be valid for the grid it was used on without any temporal restriction. Here, it can be generated for every single day and for every hour utilising the forecasts of the preceding days. Secondly, as with the ensemble

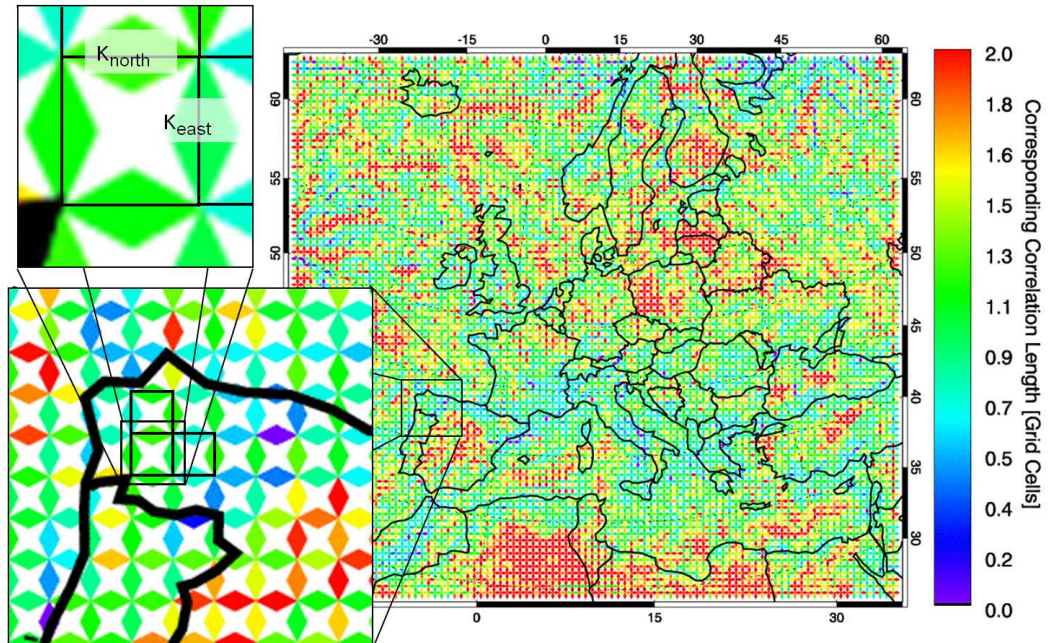


**Figure 4.2:** Horizontal diffusion coefficients for  $PM_{10}$  at July 1, 2003, 10 UTC on the European grid with 45 km resolution. Coefficients were calculated using the NMC method. 14 preceding days were used for generation.

method, the two different forecasts also show the propagation of perturbations and, by using the differences of the forecasts of the  $N$  preceding days, the covariances calculated can be interpreted as being flow dependent, reflecting the early past of the model's current state. Figure 4.2 shows horizontal diffusion coefficients for the surface layer. These were generated from 14 preceding days  $PM_{10}$  output. The big advantages are, that there is no need for additional model runs and that these covariances can be calculated offline from the regular output. Thus, it is a very convenient way for BECM generation in an operational forecast system. An offline generator is now available for the EURAD-IM.

### 4.3 Current setup

The setup used in this thesis, as well as for the operational forecast, uses a part of the variants listed above. While the diffusion algorithm is fully implemented and tested, the BECM for aerosols is restricted to a set of height

dependent, isotropic, and homogeneous correlation lengths for  $PM_{10}$  that will be used for all aerosol species. This set of correlation lengths has been derived analysing a complete years data for  $PM_{10}$  in 2009 for the layers 1 (surface), 15 (approximately the top of the mixing layer), and 23 (top layer of the model). For layers in between, a linear interpolation is applied. The exact values are described in the setup of the simulations in Chapter 5. For the variances species dependent relative and minimum errors are used.

## CHAPTER 5

---

### Episode and Campaign Simulations

---

Two episodes with very different character were chosen for investigation of various aspects of aerosol 4D-var under real-world conditions. Firstly, a very dry and hot episode with numerous wild fires in the southern parts of Europe, especially on the Siberian peninsula occurred in July 2003, resulting in high aerosol loads over parts of Europe. This episode was chosen to test both, the adjoint H-operators and the adjoint aerosol modules, and to evaluate the gain of information obtained by assimilation of ground-based and remote-sensing instruments. The assimilation of ground-based  $PM_{10}$  itself was tested and its value for an improvement of the forecast was investigated. Furthermore, the type resolved SYNAER satellite retrievals have effectively been assimilated into the model. Despite its sparsity useful results could be gathered.

As a second episode the ZEPTEP-2 campaign (second **ZEP**pelin based **Tropo**spheric photochemical chemistry **expE**Riment), October through November 2008, was selected. A Zeppelin-NT prepared as a measurement platform to carry out high resolution in-situ measurements of, among other, aerosol number densities in the PBL (Planetary Boundary Layer) and the lower free troposphere. The campaign took place in the area of Lake Constance, southern Germany. Dedicated nested grids with spatial resolutions down to 1 km were created to provide high resolution forecasts for experiment and flight planning. These were utilized to test the aerosol 4D-var algorithm's performance on small scales and the assimilation of particle number densities.

## 5.1 July 2003

Within the AERO-SAM project (Boundary layer **AERO**sol characterization from **S**pace by advanced data **A**ssimilation into a tropospheric chemistry **M**odel, funded by the German science foundation DFG) in collaboration with the German remote-sensing data center (DLR-DFD) in Oberpfaffenhofen, the summer of 2003 was chosen as a test case for the assimilation of SYNAER retrievals and the aerosol 4D-var algorithm in general.

The timespan from mid June to the end of August 2003 is characterized by a long period of very high temperatures followed by an extreme drought in south-western Europe, especially the Iberian Peninsula. During that time very stable high pressure areas were situated over Europe. Under these conditions large areas of forest and maquis shrub land burst in flames when stricken by lightning or ignited by men, accidentally or intentionally. The resulting wild-fires blew huge amounts of aerosols into the troposphere. Figure 5.1 shows more than 14,000

MODIS Thermal Anomalies 2003 July 1 to 16 : 14751 counts

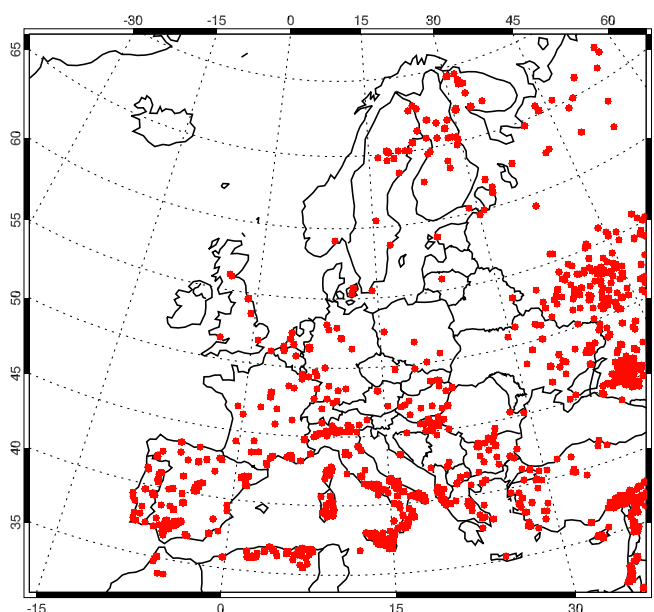


*Figure 5.1: Thermal anomalies as detected by the MODIS instruments aboard NASA's Aqua and Terra satellites from July 1 to 16, 2003.*

thermal anomalies indicating wild fires detected by the MODIS (**M**ODerate-resolution **I**maging **S**pectroradiometer) instruments aboard NASA's research satellites Aqua and Terra for the whole episode. Even more, mineral dust from the dry soil was picked up by the wind and carried over great distances. The stable meteorological conditions also facilitated a great amount of useful SYNAER retrievals due to sparse cloud coverage.

A two week episode was chosen to evaluate the performance of the aerosol data assimilation system in the presence of non periodic events like, in this case, wildfires and to investigate the additional gain of species resolved retrievals concerning aerosol forecast quality.

Three individual assimilation experiments have been accomplished for this episode:

- assimilation of **SYNAER retrievals** only,
- assimilation of **ground-based in-situ PM<sub>10</sub>** only,
- assimilation of **SYNAER retrievals** and **ground-based in-situ PM<sub>10</sub>**.

The schedule summarising the assimilation specifications for each episode day is presented in table 5.1. It is valid for all three experiments.

### 5.1.1 Episode configuration

#### Model geometry and setup

The episode under investigation starts on July 1 and ends on July 15, 2003. Simulations and 4D-var analyses have been conducted on a coarse grid only, because the focus was placed on the influence of biomass burning and dust pickup as well as on effects of long range transport. Furthermore, high resolution information on land-use and emissions has only been available for the area of central Europe and special sections of Germany, where in general there are only few SYNAER retrievals available. A detailed look into nested grids will be given in the following section. The geographical extension of the European Domain with a resolution of 45 km is exactly as displayed in Figure 5.1. This grid has 107 cells in west-east direction, 97 cells in south-north direction and 23 vertical layers. The length for each model time step was set to 600s. Modules simulating emissions for sea salt and mineral dust that are part of the aerosol model have been used in this simulation.

#### Data assimilation specifications

Placing a special focus on SYNAER retrievals in this episode, the data assimilation setup was tuned to fit the ERS-2 flyovers, which lie between 8 and 12 UTC for the European domain. Thus, the assimilation window - the interval in which measurements are assimilated - was set to start at 8 UTC with a standard length of eight hours. For some cases the interval had to be shortened. In other words, all measurements available within the assimilation window are used. After at most ten iterations, which generally was sufficient, an optimised field of initial values - the *analysis* - will be provided for the beginning of the interval, i.e. for 8 UTC. Figure 5.2 gives a schematical survey of the nomenclature and relations of different model runs. The yellow box indicates the

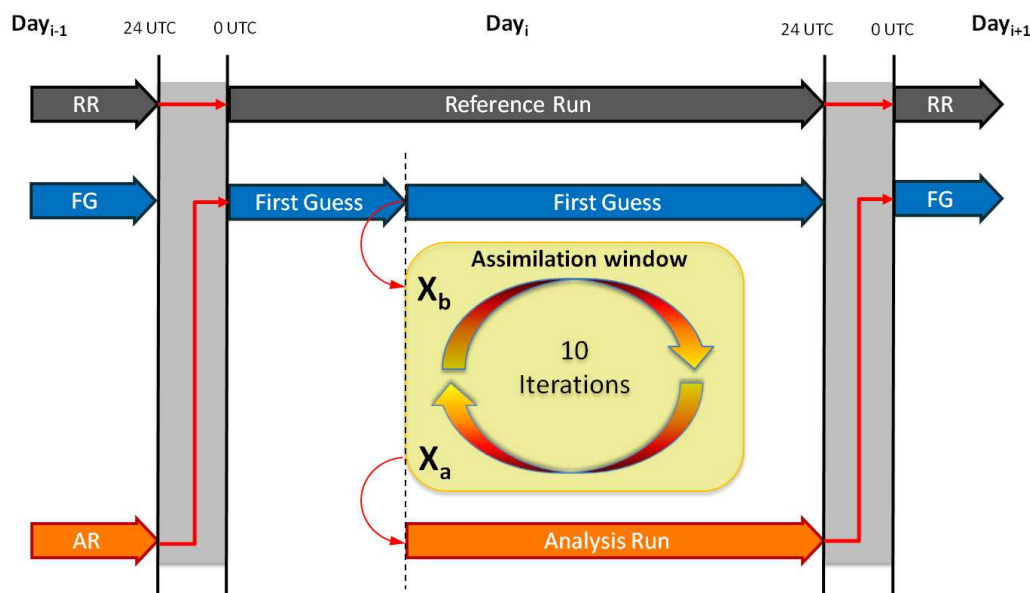


**Figure 5.2:** Schematic overview of the model runs applied in this episode. The Reference Run (black) is decoupled from assimilation. The First Guess Run (blue) provides the background values  $X_b$  at the start of the assimilation window (yellow box). After at most ten iterations an optimised set of initial values  $X_a$  - the analysis, at which costs are at a minimum - is provided to the Analysis Run (orange) that computes the initial values for the succeeding First Guess Run. The whole First Guess Run (0 - 24 UTC) is used to validate the effect of a preceding assimilation against the Reference Run.

assimilation process in which in each iteration one forward and one backward (adjoint) run is accomplished. Table 5.1 shows the settings chosen in detail.

### Available Measurements

A set of all available SYNAER aerosol optical thickness retrievals inside the European domain within the two week episode was chosen. The daily assimilation window was selected such that all possible retrievals could be included. EEA's (European Environmental Agency) Airbase has been another important source of information on aerosol concentrations in 2003. It is an annual collection of daily measurements of several air pollutants, including  $PM_{10}$ , from the member states of the European Union. This dataset contains measurements from stationary in-situ measurement sites, generally observing with an hourly frequency. For 2003 the coverage is still irregular. While there was a com-

prehensive availability of observations of many gas-phase species like ozone or carbon monoxide, there were still only few countries with regular  $PM_{10}$  measurements. Figure 5.3 shows all 714 available EEA stations observing  $PM_{10}$  in July 2003 and, as an example, the SYNAER retrievals for July 1, 2003.

As described above, a dust module is operated within the EURAD-CTM to provide emissions of soil dust and sand from dry surfaces. Unfortunately, the applied grid does not cover the large Saharan areas in northern Africa where huge amounts of dust are taken up, elevated into higher tropospheric regions, and frequently transported over wide areas of Europe. Thus, the model is not capable of simulating mineral dust from sources outside the European domain. Therefore, SYNAER mineral dust observations often differ significantly from the model values. This can be described as a lack of performance of the model which in general is expressed in terms of the respective background error of the dust species *SOILA*. This error reflects the uncertainty to predict a species' concentration assuming the physicochemical processes are covered by the model. In this case, the occurrence of long-range transported mineral dust imported through the grid's lateral boundaries is of rather random nature. As a remedy, the SYNAER measurements of *AOTDUST* get an additional weighting factor of  $10^{-1}$  multiplied to their measurement error - similar to multiplying the model values' error by a factor of 10 - representing the extraordinary uncertainty of the model in these cases. This applies for all SYNAER species *MITR* and *MILO*, whose declared origin is desert (see tables 3.5 and 3.6).

## Initial Conditions and Reference Run

First of all, a forward or forecast run without any assimilation has been accomplished from June 1, 2003 until the end of the episode. The first four weeks were used to spin-up the simulation starting from climatological conditions, i.e. starting from reasonable boundary and initial values as described in 3.1.3. This model run will also be referred to as *reference run*. It acts as a reference to identify and quantify alterations in the model's constituent fields induced by data assimilation.

### 5.1.2 Assimilation performance

As a measure of the performance of the full 4D-var system with *observation operators*, the cost reduction by the minimisation algorithm has been investigated. Fig. 5.4 shows the relative observation cost reduction for each of the SYNAER species and in-situ  $PM_{10}$ . In general it can be stated that all have

**Table 5.1:** Assimilation schedule for the episode of July 2003. Assimilation specifications and the number of available observations for each day of the episode. While EEA stations deliver hourly values, each single SYNAER pixel is counted.

| Day                             | 1      | 2   | 3   | 4   | 5   | 6   | 7   | 8   | 9   | 10  | 11  | 12  | 13  | 14  | 15  |
|---------------------------------|--------|-----|-----|-----|-----|-----|-----|-----|-----|-----|-----|-----|-----|-----|-----|
| Assimilation start              | 8 UTC  |     |     |     |     |     |     |     |     |     |     |     |     |     |     |
| Assimilation duration [hrs]     | 8      | 8   | 8   | 8   | 8   | 6   | 6   | 8   | 6   | 8   | 6   | 8   | 8   | 8   | 6   |
| Correlation lengths             |        |     |     |     |     |     |     |     |     |     |     |     |     |     |     |
| - top (layer 23)                | 150 km |     |     |     |     |     |     |     |     |     |     |     |     |     |     |
| - top of mixing layer(layer 15) | 90 km  |     |     |     |     |     |     |     |     |     |     |     |     |     |     |
| - surface (layer 1)             | 60 km  |     |     |     |     |     |     |     |     |     |     |     |     |     |     |
| No. Normalisation Iterations    | 500    |     |     |     |     |     |     |     |     |     |     |     |     |     |     |
| No. Minimisation Iterations     | 10     |     |     |     |     |     |     |     |     |     |     |     |     |     |     |
| SYNAER pixels                   |        |     |     |     |     |     |     |     |     |     |     |     |     |     |     |
| WASO                            | 205    | 46  | -   | 129 | 48  | 83  | 106 | 54  | 37  | 78  | 139 | 73  | 130 | 61  | -   |
| INSO                            | 98     | 23  | -   | 51  | 18  | 41  | 33  | 18  | 17  | 23  | 51  | 26  | 39  | 16  | -   |
| SOOT                            | 106    | 28  | -   | 61  | 25  | 41  | 56  | 39  | 18  | 42  | 54  | 26  | 62  | 35  | -   |
| SEAS                            | 8      | 3   | -   | 6   | 1   | 3   | 10  | 3   | 1   | 4   | 6   | 7   | 4   | 7   | -   |
| DUST                            | 12     | -   | -   | 12  | 2   | 3   | 9   | 2   | 2   | 6   | 24  | 3   | 14  | 5   | -   |
| Total                           | 429    | 100 | -   | 259 | 94  | 171 | 214 | 116 | 75  | 153 | 274 | 135 | 249 | 124 | -   |
| EEA stations                    | 710    | 714 | 714 | 712 | 712 | 708 | 712 | 708 | 708 | 709 | 709 | 706 | 701 | 702 | 704 |

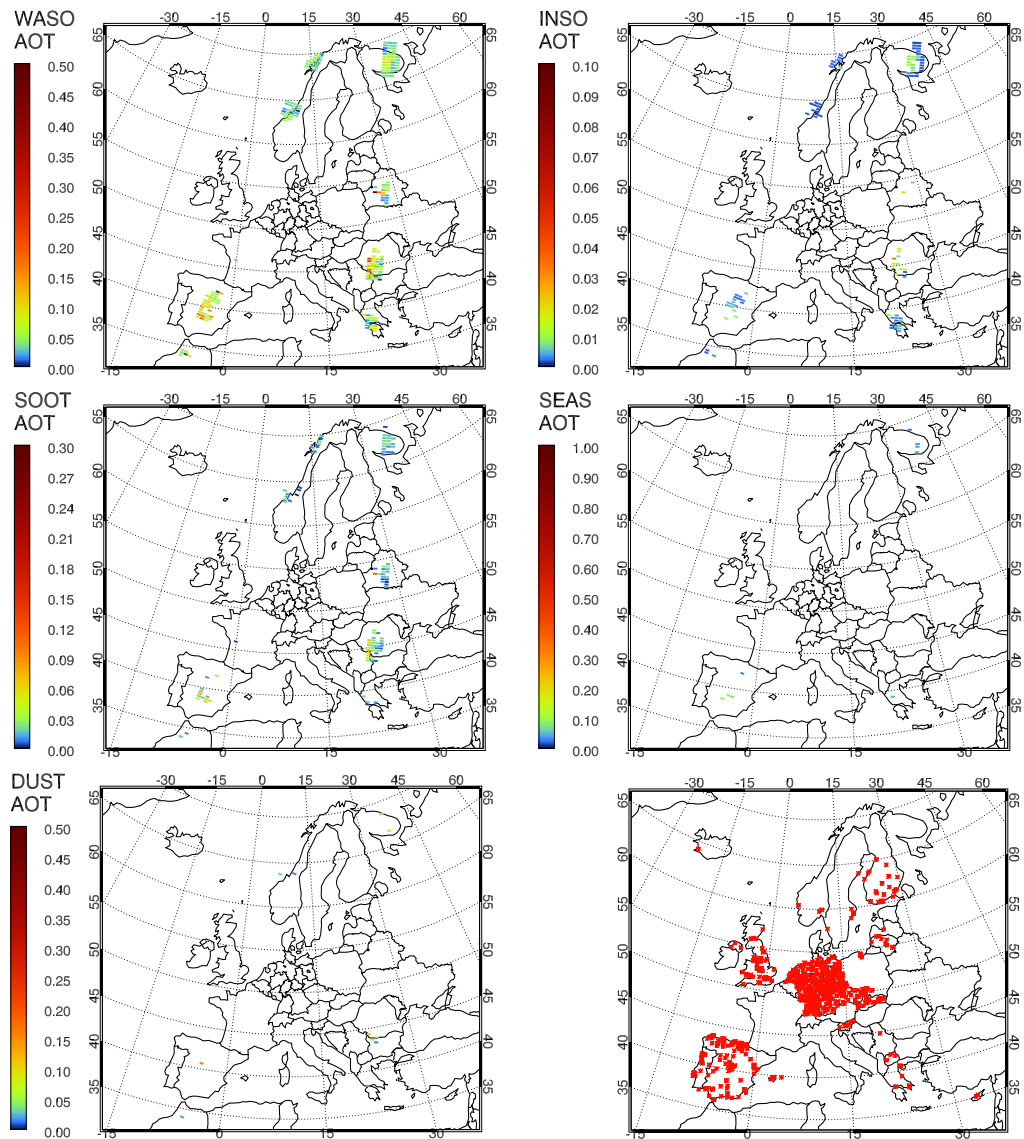


**Figure 5.3:** Example of measurements on the 45 km European domain (EUR). EURAD-IM AOT types from SYNAER retrievals on July 1, 2003. Upper left: AOT WASO. Upper right: AOT INSO. Center left: AOTSOOT. Center right: AOTSEAS. Lower left: AOTDUST. Lower right: EEA stations available for the whole episode.

been assimilated successfully. The assimilation of  $PM_{10}$  shows a very good and constant performance. This indicates that both the adjoint  $H$ -operator and the adjoint HDMR work properly. The costs for WASO and SOOT have also been reduced largely though with an inconstant quality. A significantly

weaker reduction of about only a few per cent has been observed for *INSO*, *SEAS*, and *DUST*. This seemingly low performance of the assimilation of these three species can be explained by a strong underestimation of the involved species by the model. Comparing the model equivalent AOT calculated from the model fields with AOT given by SYNAER retrievals revealed that the measured values of *INSO* are by a factor of approximately 5 – 100 larger than the modeled values. For *SEAS* a factor of about 100 – 500 holds, while for *DUST* a factor of 1000 has been found. In the latter case, the observation weight was increased by a factor of 10, as described above, to mitigate the general incapability of the model to simulate emissions of long range transported mineral dust. In the case of *SEAS* and *INSO* the sources are located inside the model domain but are obviously too weak to reproduce the measured levels. The amounts of *WASO* and *SOOT* components are of the same magnitude as the observed values. Here, it is more likely that the tangent linear approximation holds and the minimisation performs much better, with the exception of the 4<sup>th</sup>, 10<sup>th</sup>, 11<sup>th</sup>, and the 13<sup>th</sup> of July in the *SYNAER only* experiment. In these cases, especially on the 11<sup>th</sup>, the application of the weighting factor for *DUST* resulted in an overweighting of mineral dust in a way that the partial costs of *DUST* summed up to more than 98% of the overall observational costs. When looking at the gradient of the costs, it is found that it is affected in a similar way. Under these conditions the minimising algorithm efficiently reduces the costs in the descent direction of the gradient of the mineral dust (*SOILA*). At the same time the variation of the costs of the other species involved is too low to penalise a misconduct. Due to the limit of minimisation iterations, it is possible that some species end up in a state even further away from the observation than before. Figure 5.5 shows that the total costs have been reduced significantly.

### 5.1.3 Forecast performance

To further investigate the impact of the assimilation of the different datatypes on the forecast performance the observation costs of the subsequent forecast have been compared to the reference run's observation costs. That is, based on the optimised initial values a forward run was started until the end of the subsequent day (between 16 and 40 hours after the analysis) and the costs for all available measurements on that day were calculated (the First Guess Run compared to the Reference Run as described in Figure 5.2). This has been done for all three experiments. Figure 5.6 shows the relative decrease of the overall costs for each individual type of observation over the whole episode and

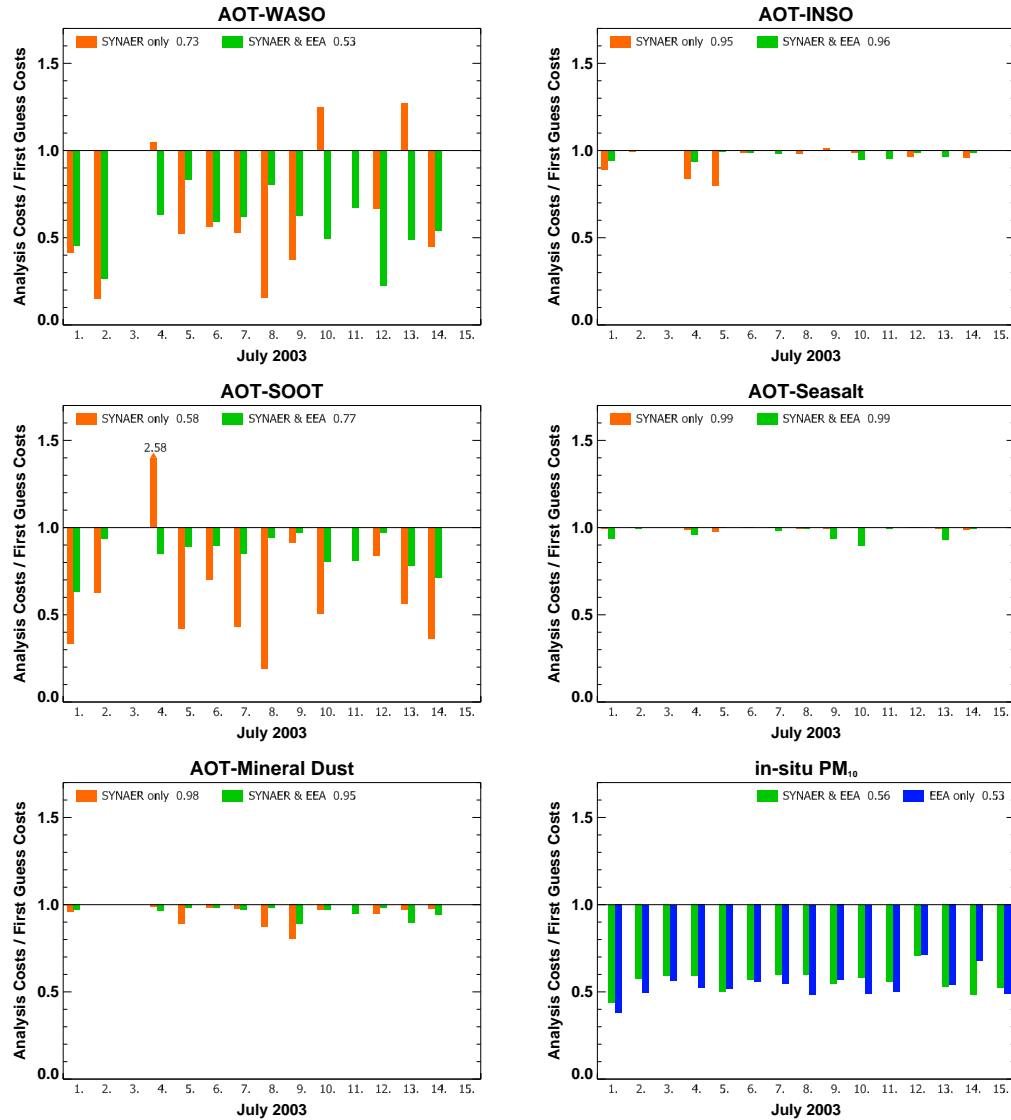


**Figure 5.4:** Minimisation performance for each assimilated species displayed as Analysis Observation Cost / First Guess Observation Cost for the three experiments SYNAER only (orange), SYNAER & EEA (green), and EEA only (blue). Top left) AOT-WASO; top right) AOT-INSO; center left) AOT-SOOT; center right) AOT-SEASALT; bottom left) AOT-DUST; bottom right) in-situ PM<sub>10</sub>. The SYNAER only statistics for July 11 have been removed as an extreme outlier.

for each experiment (right panel). Taking a look at, for example, the far-right bars in the right panel of Figure 5.6 indicating the cost reduction for in-situ

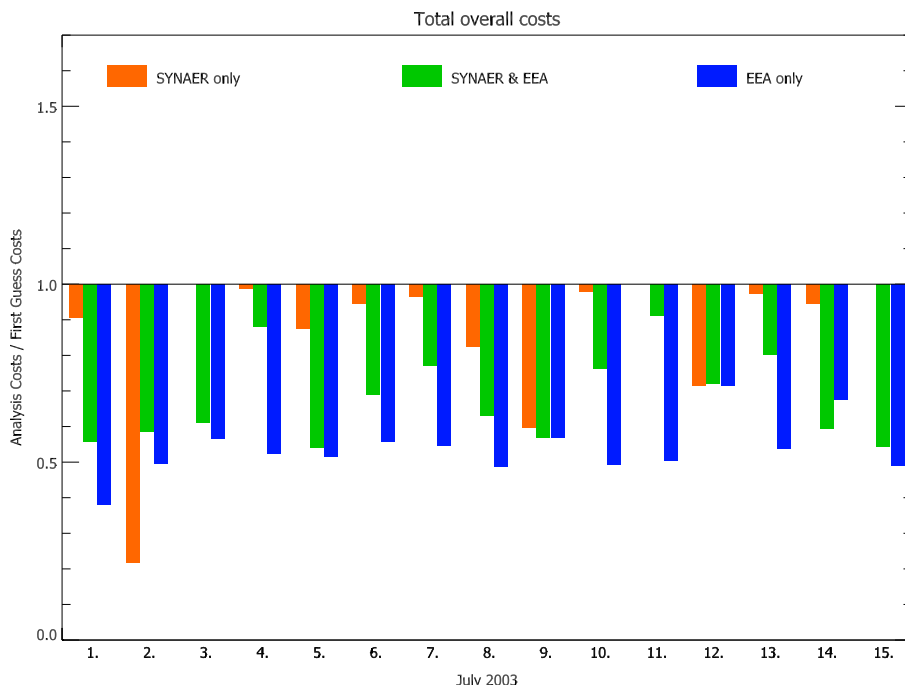


**Figure 5.5:** Overall relative reduction of the total costs by assimilation for the experiments SYNAER only (orange), SYNAER & EEA (green), and EEA only (blue). There are no retrievals available on the 3<sup>rd</sup> and the 15<sup>th</sup> of July. The 11<sup>th</sup> has been removed from the SYNAER only experiment for being an extreme outlier.

$PM_{10}$  observation: Here, the blue bar shows the relative cost reduction of all  $PM_{10}$  observations in the experiment where only  $PM_{10}$  has been assimilated when the First Guess Run's costs are compared to the Reference Run's costs. To achieve a greater comparability, another validation has been made, taking into account only observations where a relative change in costs of at least 1% had occurred (left panel of Figure 5.6). This has been done as a concession to the fact that there are far more in-situ observations available than SYNAER pixels. Even more, for very sparsely measured SYNAER species like sea salt or mineral dust one rarely finds an observation of the same type that is affected by a previous assimilation for validation. The diagram on the right of Figure 5.6 shows a good improvement of the forecast performance for *WASO*, *SOOT*, and in-situ  $PM_{10}$ , a moderate improvement for *INSO*, low for *SEAS*, and no improvement for *DUST*, in the experiments involving the assimilation of *EEA* in-situ  $PM_{10}$ . It also shows that the assimilation of *SYNAER* data alone only bears a low improvement for *WASO*, *SOOT*, and  $PM_{10}$  and almost

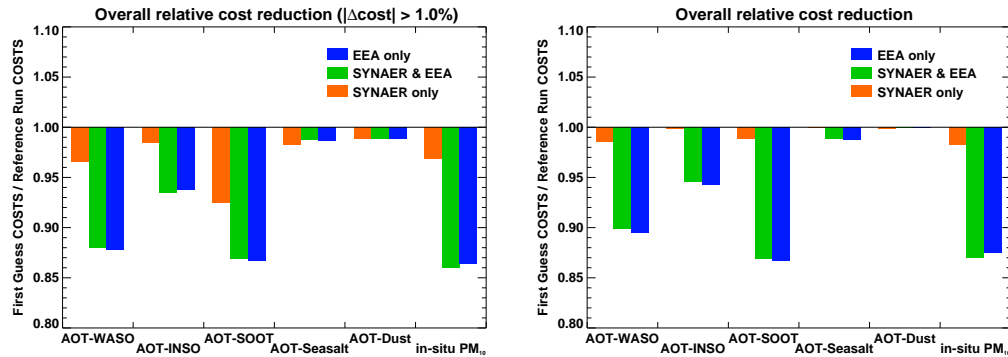


**Figure 5.6:** Forecast Run costs / Reference Run costs for the individual observations integrated over the whole episode displayed for all experiments. Left panel: Only measurements where a relative change of at least 1% occurred were taken into account. Right panel: all measurements.

none for the others. Eliminating the observations which experienced only a slight change in costs from the statistics, as it has been done in the left panel of Figure 5.6, reveals that there is a positive effect though it only affects a few measurements.

First of all, it can be stated that in each of the experiments the use of data assimilation leads to an improvement of the forecast performance on the subsequent days. Figure 5.6 shows a clear reduction of costs in the forecast for all experiments and for all measured species. Once again, the best improvement can be found for *WASO* and *SOOT* which are the species that are conditioned best, i.e. those model values that are of the same magnitude as the respective measurements. The same holds for  $PM_{10}$ .

Figure 5.7 shows both, the alteration of costs on all days of the episode and the number of affected SYNAER pixels (AOT-values) and in-situ observations ( $PM_{10}$ ), respectively. Here, the term “affected” means, again, that there was an assimilation induced difference of at least 1% between the costs in the reference run and the first guess. It can be seen, that *SOOT* is the species which benefits most from the assimilation of *SYNAER* retrievals. *WASO*, *INSO*, and *SEAS* gain their enhancement mainly through the assimilation of  $PM_{10}$ . The reason why it seems as if there is almost no beneficial impact of the assimilation of *SEAS* on itself is, that on most days there is simply no measurement at a location that is affected by assimilated *SEAS*. This is displayed by the *affected pixels* number that shows that there were only four pixels that measured a significant change in the costs. *DUST*, which doesn’t seem to be affected by assimilation at all, is even more difficult to validate because it describes long-

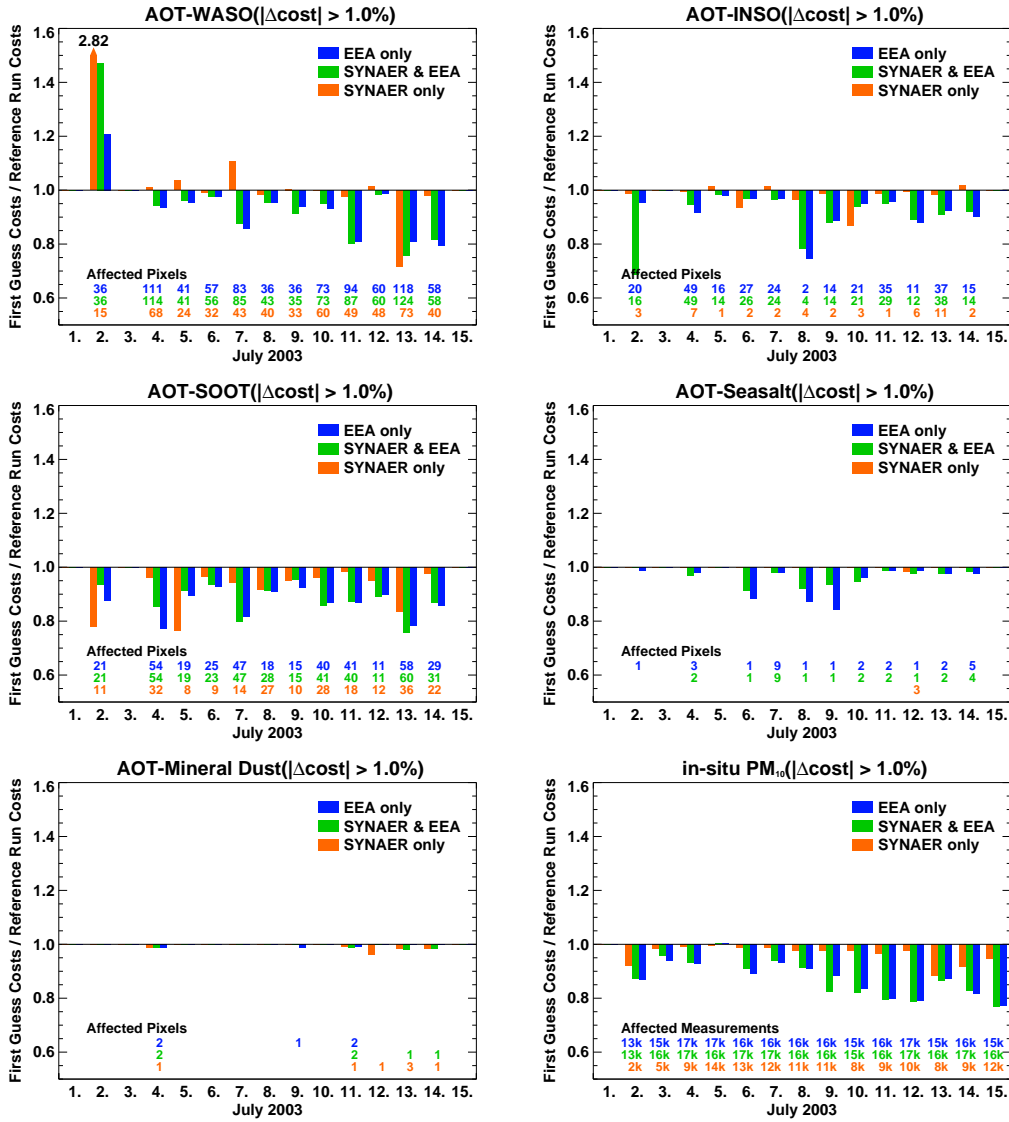


*Figure 5.7: Individual forecast performance displayed as First Guess Observation Cost / Reference Run Observation Cost for the three experiments SYNAER only (orange), SYNAER & EEA (green), and EEA only (blue). Top left) AOT-WASO; top right) AOT-INSO; center left) AOT-SOOT; center right) AOT-SEASALT; bottom left) AOT-DUST; bottom right) in-situ  $\text{PM}_{10}$ . Here, only observation at which forecast and reference Run Costs differ more than 1% are taken into account. The number of thus affected observations in each run is indicated by the same number below the bars in the respective colour.*

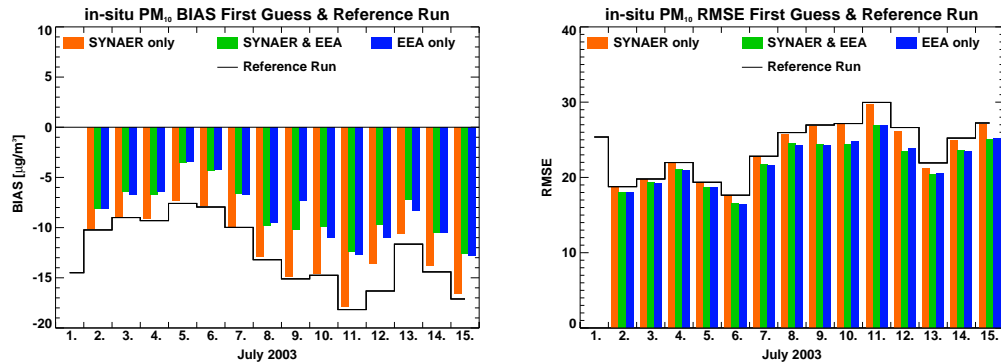


**Figure 5.8:** Daily error statistics for in-situ  $PM_{10}$  measurements in July 2003 of the First Guess for all three experiments and the Reference Run. Left panel: Bias, right panel: RMSE

range transported mineral dust in heights of about 2000  $m$  and more and is therefore almost unaffected by the assimilation of surface layer  $PM_{10}$ . This is also underlined by the low number of affected *DUST* pixels. Due to the wide spatial distribution of the hourly in-situ  $PM_{10}$  values, the effect of *SYNAER* retrieval assimilation has been captured well and can be considered a clear improvement.

An eye catching event can be observed on July 2, where assimilation leads to a significant decrease of forecast performance of *WASO* by up to a factor of 2.82 for all experiments, while the others show a reasonable improvement. This is of special interest, because this event is restricted to *WASO* observations over the Mediterranean Sea south of Spain. The observed air masses just passed the Iberian Peninsula on the preceding day where high loads of both *WASO* and *SOOT* have been successfully assimilated. In this case assimilation has led to a large but reasonable increase of the respective EURAD-IM species. This resulted in a strong overestimation of *WASO* on the subsequent day. The fact, that an overestimation also occurs in the reference run is an indicator that either there was a rain incident that was not simulated by the model, or that there is a systematic difference in the retrieval of *WASO* over land and sea.

The error statistics computed for each episode day as displayed by Figure 5.8 show a very good reduction of Bias of an average of about 30% for both experiments where in-situ  $PM_{10}$  has been assimilated, but also the *SYNAER only* experiment with rather few assimilated observations shows an overall Bias-reduction of 3.5%. Since the model output is biased in one way only, the enhancement can be expressed in per cent. A look at the RMSE reduction reveals a quite similar picture. The *SYNAER only* Run shows an improvement

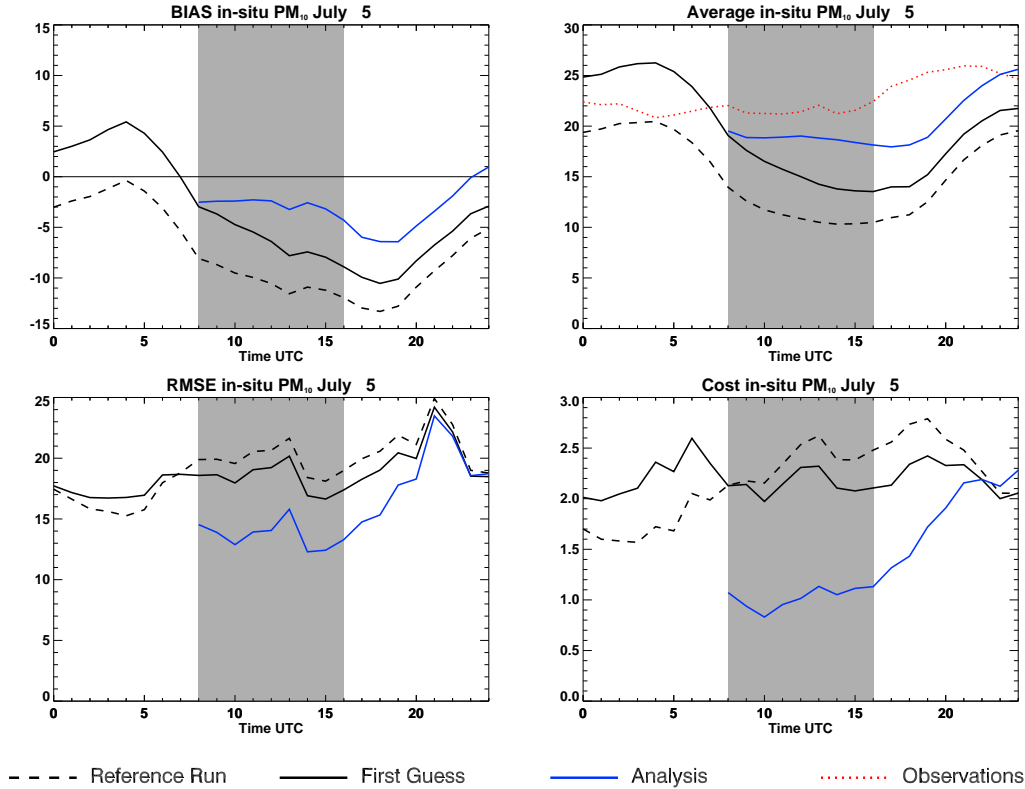


**Figure 5.9:** Error statistics for in-situ  $PM_{10}$  on July 5 2003. Plots show hourly values for available in-situ observations of Bias (upper left), average (upper right), RMSE (lower left), and costs (lower right). The grey shaded area indicates the assimilation window. The First Guess Run is the continued Analysis of the preceding day.

of about 1% while for the others an average of about 6.5% can be found. Recall, upon examination of the results concerning an improvement of the forecast by data assimilation, the window of inspection is the day following the assimilation procedure. Assimilation delivers optimised initial values for 8 UTC. Then a standard forward run is accomplished and statistics are calculated from 0 - 24 UTC on the subsequent day, i.e. between hour 16 and 40 after analysis. Because of the low number of SYNAER observations Bias and RMSE inspection has only been done for  $PM_{10}$ .

To point out how the effects of assimilation propagate in time, Figure 5.9 displays hourly Bias, RMSE, and costs for *Reference Run*, *First Guess*, and *Analysis* as well as the overall average for in-situ  $PM_{10}$ . As an example, this is shown for July 5 for the *SYNAER & EEA* experiment. The error statistics for

the *EEA only* experiment look quite the same while there is only few statistics for the *SYNAER only* Run. The grey shaded area indicates the assimilation interval. In the Bias and average plots the diurnal cycles of both the model (solid and dashed lines) and the observations (red dots) show typical discrepancies in behaviour especially at day-time. Since the assimilation window has been selected to cover the SYNAER retrievals between 8 and 12 UTC, the initial values are optimised with the day-time observations and, thus, often result in a slight overestimation at night-time. This effect can be observed comparing the Reference Run and the First Guess, where there is an overestimation between 0 and 7 UTC of this day but still a reasonable reduction of RMSE during day-time and of Bias from 6 UTC until the end of the day. Taking a look at the analysis (blue line) another phenomenon can be observed very well. Inside the assimilation window the model is forced to converge to the course of the observations, while outside the window it relaxes to the diurnal cycle again but with a certain shift. RMSE and costs seem to have reapproached the values of the Reference Run after a few hours (here at approx. 22 UTC) but the Bias' of First Guess and Reference Run show that the effect of assimilation often lasts longer than 40 hours (8 UTC on preceding day till at least 24 UTC of this day).

#### 5.1.4 Optimised Initial Values

After the statistical evaluation of the assimilation system for the experiments, a closer look at the generated initial fields for selected species is taken to survey the impact and the spatial extensions of the measurements involved. Figures 5.10 through 5.15 all show plots of a EURAD-IM species representative for the respective SYNAER-retrieval. Each Figure is composed of four plots. An analysis field showing mass concentrations of the optimised initial values, that are plotted for the *SYNAER & EEA* experiment, i.e. after assimilation of both, *SYNAER only* and *EEA only* measurements, since this is the desired setup making use of a maximum of information. Furthermore, the analysis-increment (analysis values - background values) is plotted individually for each experiment. While the analysis field gives an overview of current aerosol concentrations in the model, the increments shall emphasise the influences of the different types of observations. The plots show values for July 1, 2003 because it was the first day for all simulations, when the assimilations started with the same background values. Furthermore, on this day a maximum number of SYNAER retrievals was available (as depicted in Figure 5.3).

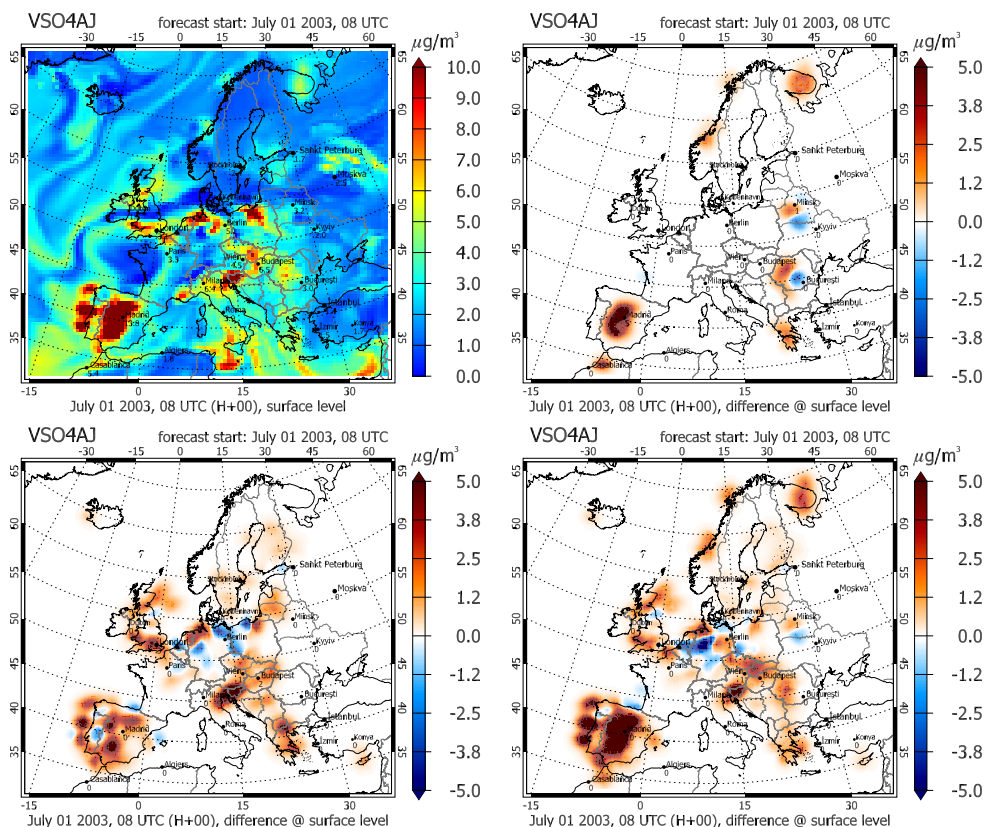


**Figure 5.10:** Surface layer accumulation mode  $SO_4^{2-}$  as a representative for water soluble species on July 1, 2003 at 8 UTC. Analysis field of the SYNAER & EEA experiment (top left), and analysis increments (Analysis - Background) of the SYNAER only (top right), EEA only (bottom left), and SYNAER & EEA (bottom right) experiments.

**Water soluble species:** As the driving force within the in aerosol chemistry sulfate has been chosen to as a representative for the group of water soluble species. Its accumulation mode concentrations are shown in Figure 5.10. Comparing the SYNAER only (upper right) and EEA only (lower left) plots reveals that the increments are of similar magnitude. This is also reflected in the SYNAER & EEA plot (lower right) where the signature of assimilated SYNAER-retrievals can clearly be seen over Scandinavia, the Iberian Peninsula, and from the Kola Peninsula to Greece. The analysis plot (upper left) shows that the impact of data assimilation in the areas observed is rather high in terms of a strong increase, whereas over Central Europe, where there is already a higher sulfate load, an increase as well as a decrease, can be observed.

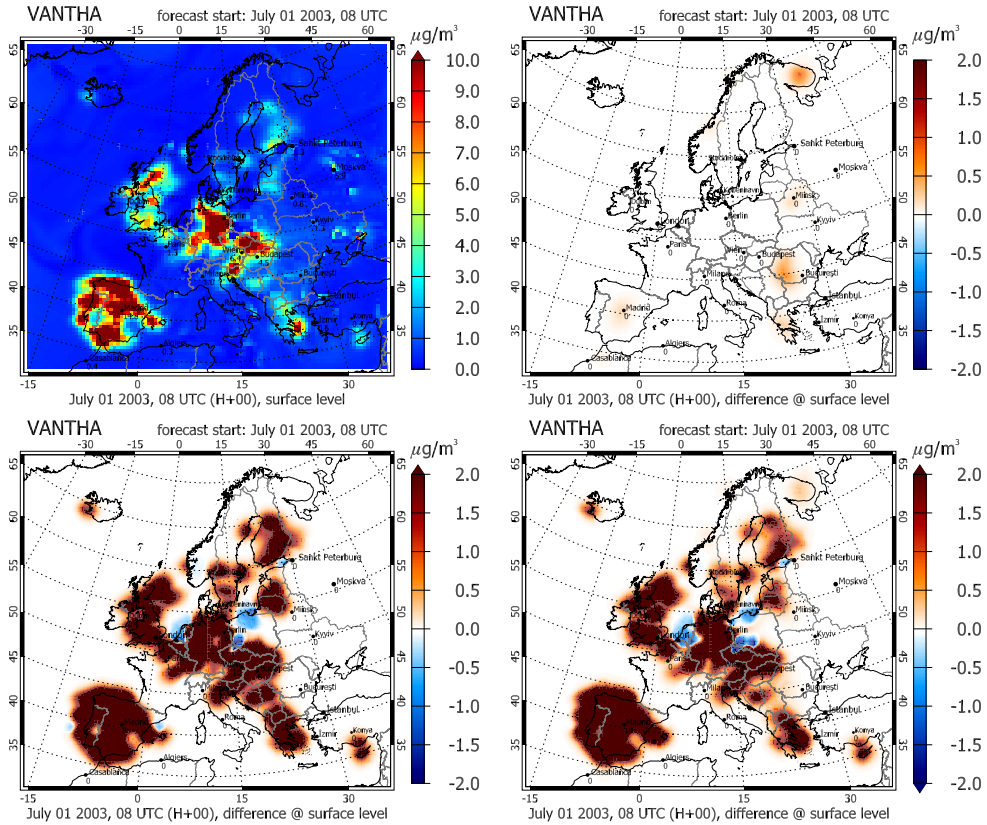


**Figure 5.11:** Surface layer coarse mode anthropogenic aerosols (VANThA) as a representative for water insoluble species on July 1, 2003 at 8 UTC. Analysis field of the SYNAER & EEA experiment (top left), and analysis increments (Analysis - Background) of the SYNAER only (top right), EEA only (bottom left), and SYNAER & EEA (bottom right) experiments.

**Water insoluble species:** In this case, coarse anthropogenic aerosol was chosen to represent *INSO* in Figure 5.11. It is obvious that the analysis of these species is dominated by  $PM_{10}$  assimilation. Only over the Kola Peninsula a common and Romania a noteworthy contribution by *INSO* can be observed.

**Soot:** Soot is represented by accumulation mode Elemental Carbon in Figure 5.12. A pattern very similar to the one observed for *WASO* can be found. The increase is of the scale of  $1\mu g/m^3$  and the analysis plot indicates that this is also the magnitude of the background field.

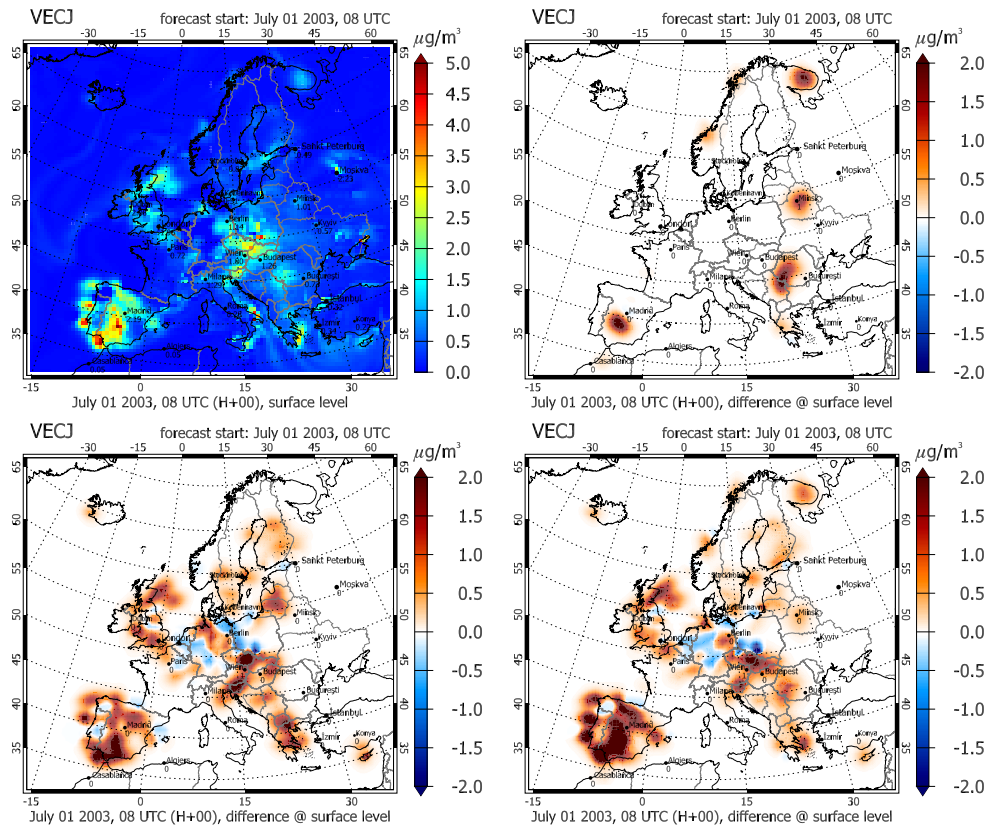


**Figure 5.12:** Surface layer accumulation mode elemental carbon (VECJ) as a representative for SOOT species on July 1, 2003 at 8 UTC. Analysis field of the SYNAER & EEA experiment (top left), and analysis increments (Analysis - Background) of the SYNAER only (top right), EEA only (bottom left), and SYNAER & EEA (bottom right) experiments.

**Sea Salt:** Sea Salt is only being assimilated as coarse mode Sea Salt and, displayed in Figure 5.13. The analysis field closely resembles the analysis field of *INSO* as could be expected. The influence of *SEAS* retrieval is also limited since there were only eight observations available on that day.

**Mineral Dust:** Figure 5.14 shows the analysis fields and increments for mineral dust in model at approximately 3000 m above ground, because this is the region where the SYNAER retrieval detects long range transported minerals with desert origin. Here, both in-situ and retrieval have an impact of about the same order of magnitude. The analysis field also shows that it is not exceptional to the model to simulate aerosol loads of this magnitude, since the two

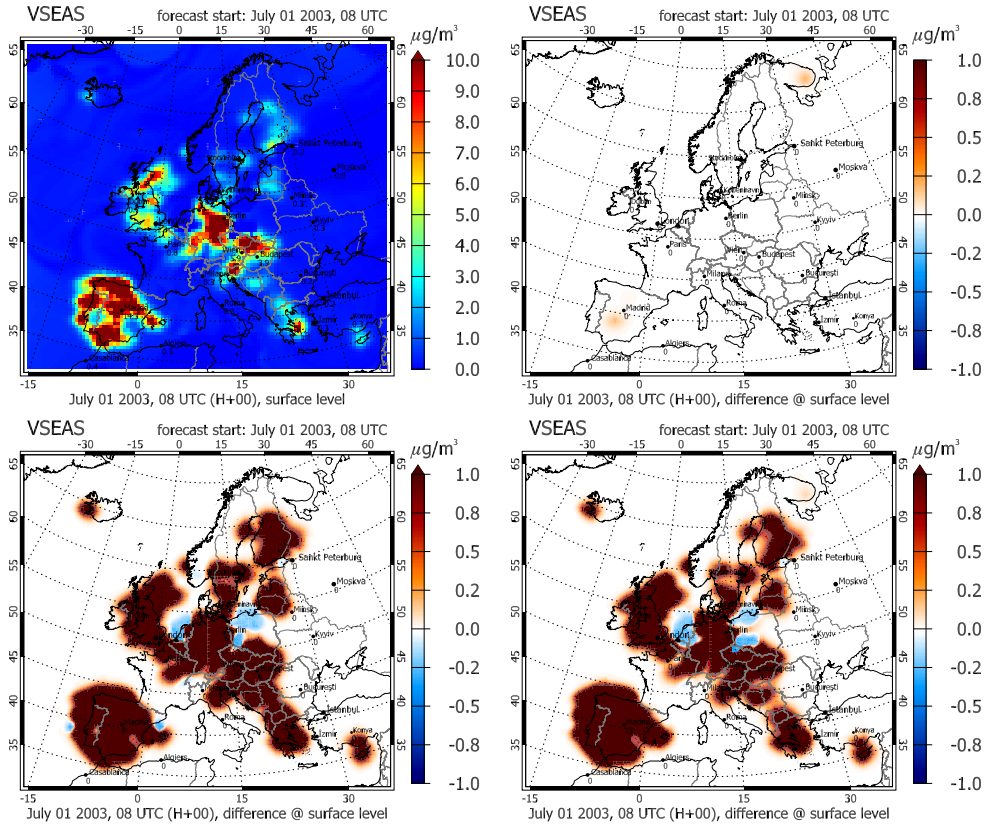


**Figure 5.13:** Surface layer coarse mode sea salt (VSEAS) on July 1, 2003 at 8 UTC. Analysis field of the SYNAER & EEA experiment (top left), and analysis increments (Analysis - Background) of the SYNAER only (top right), EEA only (bottom left), and SYNAER & EEA (bottom right) experiments.

plumes northwest of Switzerland and west of Sicily are not a result of data assimilation but soil dust from Spain generated by the dust emissions module.

**Particulate Matter  $PM_{10}$ :** Finally,  $PM_{10}$  has been plotted in Figure 5.15. Here, too, the supplementary character of the assimilation of SYNAER-retrievals can clearly be observed. Since  $PM_{10}$  is the most common measurement parameter for aerosols this plot shows the extent of the influence of aerosol 4D-var particularly well.

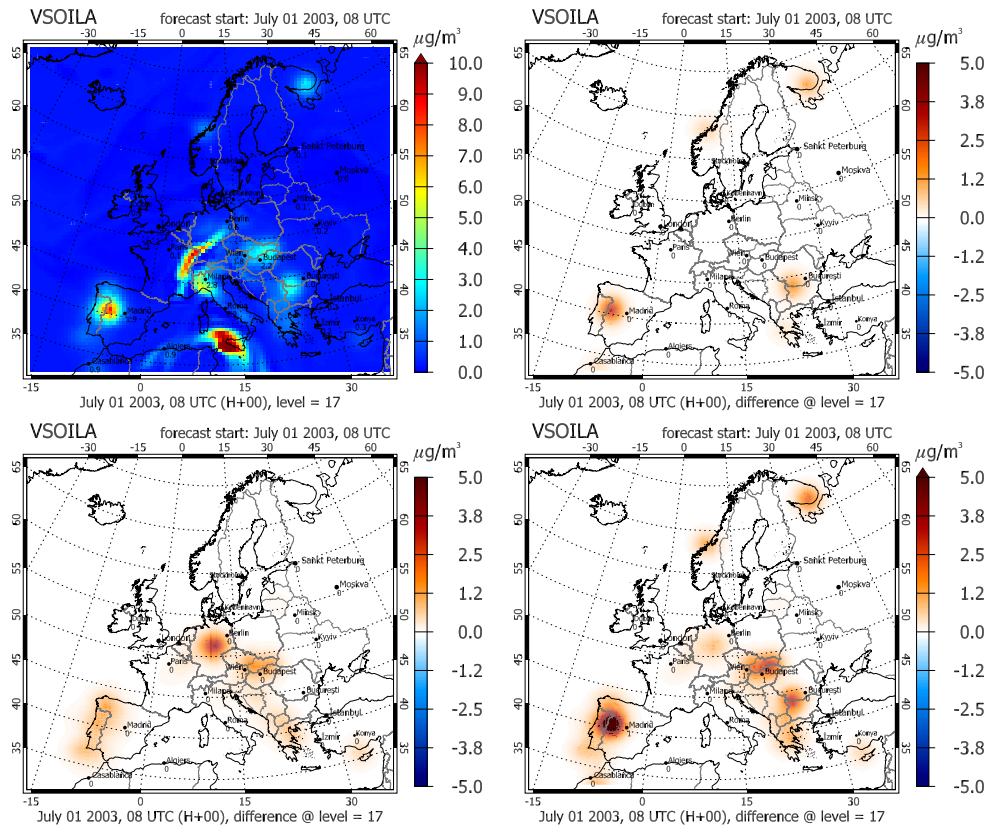


**Figure 5.14:** Coarse mode mineral dust (VSOILA) in layer 17, a height above ground of approximately 3 km on July 1, 2003 at 8 UTC. Analysis field of the SYNAER & EEA experiment (top left), and analysis increments (Analysis - Background) of the SYNAER only (top right), EEA only (bottom left), and SYNAER & EEA (bottom right) experiments.

### 5.1.5 Summary

It can be stated that assimilation of  $PM_{10}$  and SYNAER retrievals, especially WASO and SOOT, in general works very well. Increased aerosol loads over the Iberian Peninsula as well as in the eastern parts of Europe could be reproduced by the assimilation system. It also has been demonstrated that it is well possible to introduce long range transported mineral dust into the model, as far as there is a sufficient number of observations. Introducing a weighting factor for DUST did on the one hand enable the adaption to high mineral dust loads in regions where there had not been any before. But, on the other hand this sometimes distorted the assimilation by overweighting mineral dust in a way

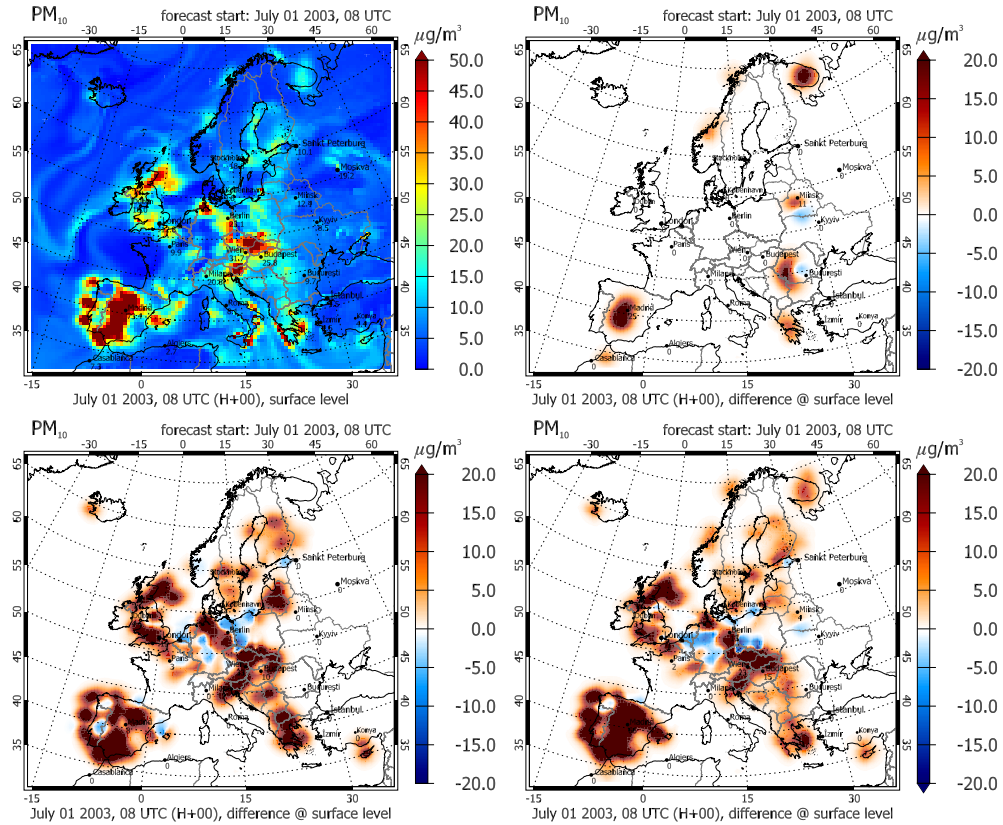


**Figure 5.15:** Surface layer  $PM_{10}$  on July 1, 2003 at 8 UTC. Analysis field of the SYNAER & EEA experiment (top left), and analysis increments (Analysis - Background) of the SYNAER only (top right), EEA only (bottom left), and SYNAER & EEA (bottom right) experiments

that a proper assimilation of other species was hampered. Since the ignorance of elevated mineral dust aerosols is a lack of knowledge of the model, the proper procedure would have been to adjust the model's error, i.e. the background error, instead of decreasing the observational error. Thus, the formation of very large gradients could have been avoided because the tangent-linear approximation is no longer valid in these cases. But, this would also have meant a major effort to induce this extra information into the model, like for example an additional model variable flagging a special status for certain species. The method chosen is not ideal, but it was a satisfying straight-forward attempt. A similar problem can be observed inspecting *INSO* and *SEAS*. Here, the sources of the respective EURAD-IM species lie within the model domain and their emissions can be generated. Nevertheless, the discrepancies between model

equivalents and observations sometimes are still very large, with factors of occasionally up to 500. The reason is, as with elevated mineral dust, that the model simulates clean air conditions for these values and. In these cases the observation error is often much higher than the equivalent background error with the result that the analysis adheres close to the background. Though this is valid for assimilation of in-situ  $PM_{10}$ , too, there is still the large number of observations that facilitates a deviation from the initial values. These clean air condition simulated by the model bring forth another effect. Species that have the same background error receive the same increment when assimilating  $PM_{10}$ . All model species have a minimum error which is equal for the coarse mode species of sea salt (*SEAS*), mineral dust (*SOILA*), and anthropogenic aerosols (*ANTHA*). Thus, the increment plots for these species look very similar for the first day. Altogether, it can be found that the influence of assimilation can last several days at least under stable meteorological conditions prevailing in this episode. The second inherent difference between *SYNAER* retrievals and in-situ measurements, the vertical extent, does only have a visible effect in layers above approximately 3000 m. Due to efficient vertical exchange within the mixing layer no noticeable differences in terms of vertical distribution can be found between the two types of observations.

As a general result it can be stated that aerosol 4D-var has proven to significantly enhance the aerosol forecast skill of EURAD-IM on a 2-day basis. With the *SYNAER* retrieval delivering aerosol loads of higher layers, an impact on distant measurement sites could be observed. The results displayed in this section clearly show the strengths and limitations of the current aerosol 4D-var system of EURAD-IM on the coarse European grid with a spatial resolution of 45 km.

## 5.2 ZEPTEP-2 Campaign 2008

The ZEPTEP-2 campaign has been conducted from October 17 to November 8, 2008. A Zeppelin NT (“New Technology”) has been specially prepared as an instrument platform for an extensive measurement campaign investigating photo chemistry, chemical composition, and particle properties of the lower troposphere over areas with different land use in the region around Lake Constance, southern Germany. A special forecast was set up to guide flight planning and to facilitate the determination of places-of-interest for the scientific staff.

Depending on meteorological conditions and different scientific objectives, 25 flights were carried out during this episode. Subject to technical limitations, the overall weight limiting the maximum altitude, different cabin layouts (dif-

ferent instrument setups) were designated. Among devices to measure photolysis rates or concentration of gas-phase species like  $O_3$ ,  $CO$ ,  $NO_x$ ,  $HCHO$ ,  $HONO$ , and  $HO_2$ , a condensation particle counter (CPC) was mounted during 12 flights to measure particle number densities ( $PND$ ).

**Table 5.2:** List of ZEPTER-2-flights. *CPC* indicates that particle number densities have been measured. **Bold printed flights** have been used for assimilation.

| Flight    | Date          | Start        | End          | Characteristics                      |            |
|-----------|---------------|--------------|--------------|--------------------------------------|------------|
| 01        | Oct 17        | 17:20        | 19:32        | Lake Constance                       |            |
| 02        | Oct 18        | 09:45        | 14:08        | Lake Constance                       |            |
| 03        | Oct 18        | 14:11        | 17:45        | Lake Constance                       |            |
| 04        | Oct 19        | 08:45        | 13:25        | Ravensburg, Forest of Altdorf        |            |
| 05        | Oct 19        | 13:42        | 17:36        | Ravensburg, Forest of Altdorf        |            |
| 06        | Oct 20        | 04:43        | 10:50        | Lake Constance                       |            |
| 07        | Oct 20        | 11:26        | 17:18        | Lake Constance                       |            |
| 08        | <i>Oct 24</i> | <i>14:38</i> | <i>18:08</i> | <i>Lake Constance</i>                | <i>CPC</i> |
| 09        | Oct 25        | 13:20        | 16:44        | Lake Constance                       |            |
| 10        | Oct 26        | 12:40        | 17:01        | Forest of Altdorf                    |            |
| 11        | Oct 26        | 17:40        | 20:45        | Forest of Altdorf                    |            |
| 12        | Oct 27        | 06:20        | 06:58        | Forest of Altdorf                    |            |
| <b>13</b> | <b>Oct 31</b> | <b>15:04</b> | <b>17:54</b> | <b>Lake Constance</b>                | <b>CPC</b> |
| <b>14</b> | <b>Nov 02</b> | <b>11:02</b> | <b>14:31</b> | <b>Forest of Tett nang</b>           | <b>CPC</b> |
| <b>15</b> | <b>Nov 02</b> | <b>15:15</b> | <b>17:57</b> | <b>Forest of Tett nang</b>           | <b>CPC</b> |
| <b>16</b> | <b>Nov 03</b> | <b>10:07</b> | <b>13:40</b> | <b>Ravensburg, Forest of Altdorf</b> | <b>CPC</b> |
| <b>17</b> | <b>Nov 03</b> | <b>14:10</b> | <b>17:37</b> | <b>Ravensburg, Forest of Altdorf</b> | <b>CPC</b> |
| <b>18</b> | <b>Nov 03</b> | <b>18:01</b> | <b>20:59</b> | <b>Ravensburg, Forest of Altdorf</b> | <b>CPC</b> |
| <b>19</b> | <b>Nov 05</b> | <b>10:44</b> | <b>14:31</b> | <b>Major traffic routes</b>          | <b>CPC</b> |
| <b>20</b> | <b>Nov 05</b> | <b>15:50</b> | <b>20:28</b> | <b>Lake Constance</b>                | <b>CPC</b> |
| <b>21</b> | <b>Nov 07</b> | <b>09:09</b> | <b>13:25</b> | <b>Major traffic routes</b>          | <b>CPC</b> |
| <b>22</b> | <b>Nov 07</b> | <b>15:07</b> | <b>16:40</b> | <b>Major traffic routes</b>          | <b>CPC</b> |
| <b>23</b> | <b>Nov 07</b> | <b>17:27</b> | <b>20:55</b> | <b>Major traffic routes</b>          | <b>CPC</b> |
| 24        | Nov 08        | 11:09        | 14:14        | Major traffic routes                 |            |
| 25        | Nov 08        | 14:33        | 17:19        | Lake Constance                       |            |

With the exception of Flight 8, the CPC was mounted on flights carried out in

the second half of the episode. Thus, the first part from October 17 through 30 was taken to evaluate the aerosol assimilation system on nested grids, while on the remaining nine days the focus was set on the assimilation of *PND*. Table 5.2 lists the flights, a short description of the environmental characteristics, and CPC use. Flights displayed in bold print have been taken into account for the assimilation of airborne *PND*.

### 5.2.1 Model configuration

The forecast consists of a sequence of three recursively nested grids embedded in a coarse mother grid amply covering Europe. Table 5.3 lists the key data. In the follow-up of the campaign nests *N0* to *N2* have been used for data assimilation. Nest *N3* was excluded due to extreme computing times of a factor of about 8 times the value of Nest 2. Extension and geographical location of the nests used for assimilation are displayed in Figure 5.17.

**Table 5.3:** Configuration of the Zepter-2 nested grids. Computing time refers to a 72-hour forecast.

|                      | Europe     | Central-Europe | Zepter-2 N2 | Zepter-2 N3 |
|----------------------|------------|----------------|-------------|-------------|
| Abbr.                | <i>EUR</i> | <i>CEN</i>     | <i>ZP2</i>  | <i>ZP3</i>  |
| Nest                 | N0         | N1             | N2          | N3          |
| Resolution [km]      | 45         | 15             | 5           | 1           |
| Grid Cells W-E       | 107        | 70             | 97          | 236         |
| Grid Cells N-S       | 97         | 76             | 88          | 146         |
| Time step [s]        | 600        | 240            | 120         | 60          |
| Computing time [min] | 34         | 38             | 110         | 885         |

### 5.2.2 Assimilation configuration

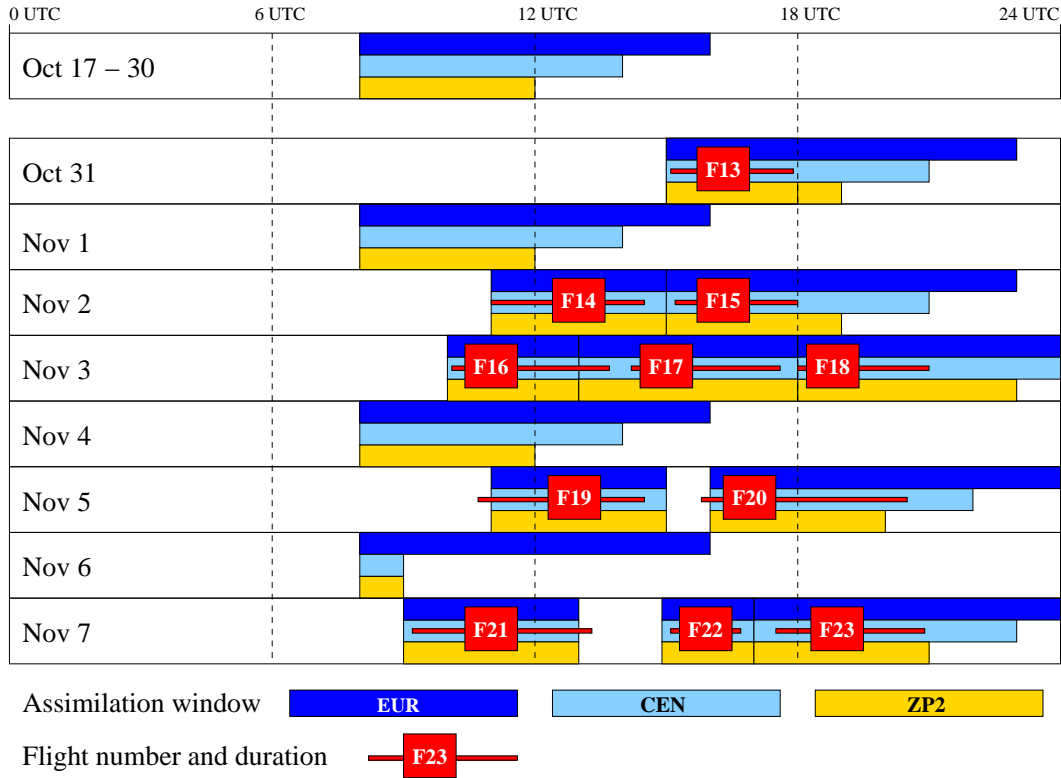
In addition to the description on nesting given in section 3.3), the nesting strategy for assimilation has to be explained. The child grid assimilation run inherits its boundary values from the parent grid's First Guess Run for the same period. Here, the parent grid analysis is already available but this brings

**Table 5.4:** Data assimilation configuration used on the nested grids during the ZEPTEP-2 campaign

|                              | <i>EUR</i> | <i>CEN</i> | <i>ZP2</i> |
|------------------------------|------------|------------|------------|
| No. Normalisation iterations | 500        |            |            |
| No. Minimisation iterations  | 10         |            |            |
| Correlation Length [km]      |            |            |            |
| Model top (Layer 23)         | 150        | 90         | 60         |
| Top mixing layer (Layer 15)  | 90         | 60         | 30         |
| Surface                      | 60         | 40         | 20         |

along the hazard to repeatedly assimilate the same measurements. The initial values are taken from an Analysis Run on the same grid. In the absence of airborne observations the main assimilation window has been set to start at 8 UTC for all nests. The length of the assimilation window has been reduced with increasing resolution. This has been due to either meteorological reasons, on windy occasions the information was in the meantime transported out of the domain, or numerical reasons, because the gradients turned out to become unstable on long temporal ranges, and to keep computational effort low. Figure 5.16 shows the assimilation windows chosen with respect to date and nest during the whole campaign. The assimilation windows have been selected such that they cover either most of the available SYNAER retrievals or, if available, the ZEPTEP-2 flights as accurate as possible. On days with *CPC* observations one assimilation window has been set up for each flight.

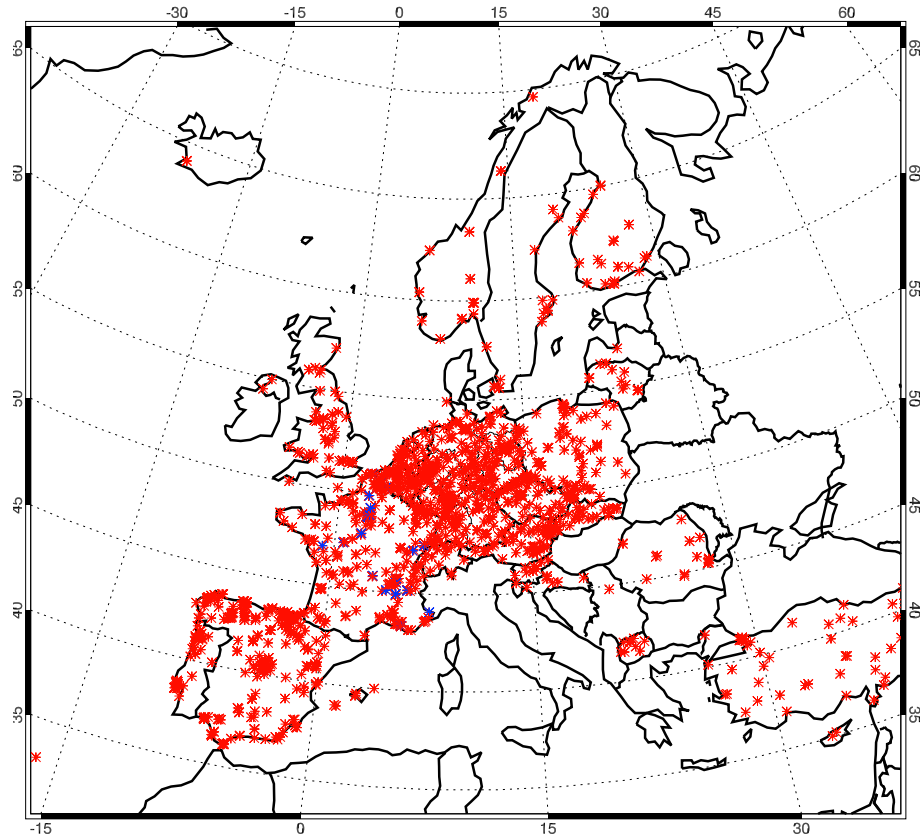
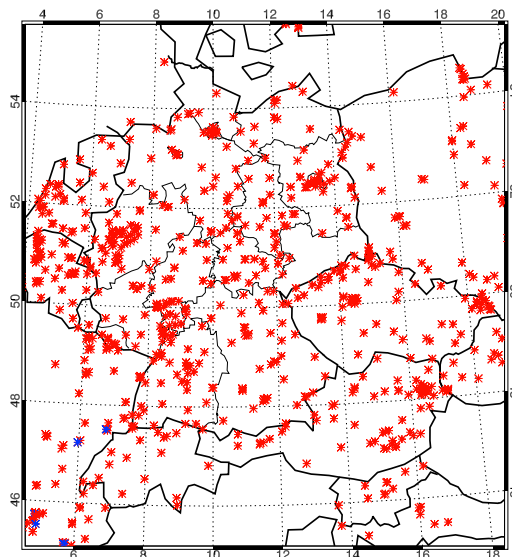
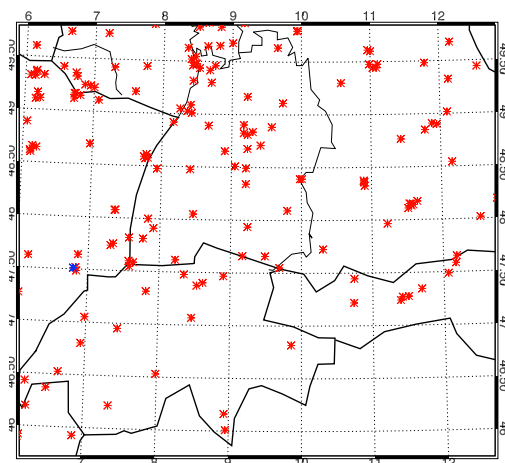
For the determination of the height depending horizontal correlation lengths an annual average for  $PM_{10}$  correlation lengths in the layers 1, 15, and 23 has been computed using the NMC method (see 4.2.3). This average has been built taking annual fields of the year 2009 for the domains *EUR* and *CEN*. Values for domain *ZP2* are only available for this very campaign episode. To provide a remedy the correlations have been taken from another 5 km domain covering the German federal state of North-Rhine-Westfalia (NRW). Although the orographic conditions of NRW are different - it is far away from being a high mountain area - it can still be used for the southern part of Germany which is a hilly area as well. Here, most of the observations are located. Furthermore, the correlation lengths generated that way are just a reasonable estimate. Table 5.4 lists the relevant settings chosen for assimilation.



**Figure 5.16:** Schedule of assimilation windows for each domain. Red bars indicate flight duration. Only assimilated flights are displayed.

### 5.2.3 Available observations

The assimilation of AOT from operational SYNAER retrievals and in-situ  $PM_{10}$  has already been demonstrated in the preceding chapter. Both data types are also used in this campaign. However, due to large cloud coverage, there are only few retrievals available. Additionally,  $PM_{2.5}$  (Particulate Matter with a diameter of less than or equal to  $2.5\mu m$ ) from French in-situ observation sites and, as a novel data source,  $PND$  from the CPC mounted aboard the Zeppelin NT. This  $PND$  is given as the *number of particles with diameter within a range from  $0.005\mu m$  to  $3.0\mu m$  per  $m^3$* . The available in-situ measurements are depicted in Figure 5.17, where the red crosses indicate  $PM_{10}$  and the blue crosses  $PM_{2.5}$ . The set of in-situ measurements is composed of values from EEA’s Airbase data archive supplemented by data from environmental institutions of Austria, France, and Switzerland. A summary of available observations is given in Tables B.1 through B.3.

(a) 45km domain *EUR*(b) 15km domain *CEN*(c) 5km domain *ZP2*

**Figure 5.17:** Domains used for assimilation in the ZEPTEP-2 campaign: 45 km domain Europe (a), 15 km domain Central Europe (b), and 5 km domain ZEPTEP-2 Nest 2 (c). Crosses display in-situ observations for  $PM_{10}$  (red) and  $PM_{2.5}$  (blue).

### 5.2.4 Assimilation performance

In terms of the ratio *Analysis costs/First Guess costs* as a measure for the performance of the assimilation system, it can be stated that assimilation performs well on each of the investigated grids. In Figures 5.18 and 5.19 the performances separated by grid and type of observation are displayed. Upon inspection of the ground data ( $PM_{10}$  and  $PM_{2.5}$ ) cost reduction, one can see that in the first part of the campaign there is a rather constant performance with a larger reduction on the coarser grids. The explanation is an already improved First Guess as a result of the better resolution of the nests and optimised boundary values. Thus, the costs of the First Guess are reduced and the remaining cost reduction is not as large as on the coarser grids. Figure 5.24 illustrates this phenomenon. On days containing airborne *PND* measurements the  $PM_x$  cost reduction is slightly larger on the finer grids. This can be explained by the large number of *PND* measurements. A larger number of minimisation iterations might well be a remedy. The very large number of *PND* observations leads to a drastical decrease in *PND* observational costs because they are mostly being corrected in the same direction. SYNAER retrieval assimilation minimises moderately on the *EUR* grid, though there are only few pixels available. On smaller scales only a small number is at hand for assimilation and therefore, statistics have to be treated with some caution. The reason why the average SYNAER reduction on the *EUR* grid is equal to 1 is a set of twenty very costly *DUST* pixels on November 1, which could not be assimilated properly. The cost reduction on November 1 is by far the worst of all non-*PND* assimilations. This is also the reason why in the Total Overall costs plot in Figure 5.19 the reduction on the *EUR* grid is only moderate by 67%.

Figure 5.20 shows a comparison of reduction of both  $PM_{2.5}$  and  $PM_{10}$  for the whole campaign and Figure 5.21 displays a timeseries of the observations for October 27, 2008 at Montbeliard, France, the only  $PM_{2.5}$  measurement site within the *ZP2* domain. This site, like all French in-situ sites observing  $PM_{2.5}$ , is a twin-measurement site, e.g.  $PM_{2.5}$  and  $PM_{10}$  are measured at the same location. As shown in the time series of Figure 5.21 the values for  $PM_{2.5}$  are slightly overestimated while at the same time  $PM_{10}$  is underestimated. Both integrated aerosol concentration values are treated as being independent in the assimilation scheme, although there should rather be an additional constraint like the treatment of  $PM_{2.5-10}$  (the mass concentration of particles of a diameter between 2.5 and 10  $\mu m$ ) instead of  $PM_{10}$  here. In this case, the gradients for the aerosol model species are opposing. Still, a very small improvement in costs of about 5% can be found for both. Since the station of Montbeliard is unique for  $PM_{2.5}$  within the *ZP2* domain, the information is too sparse to

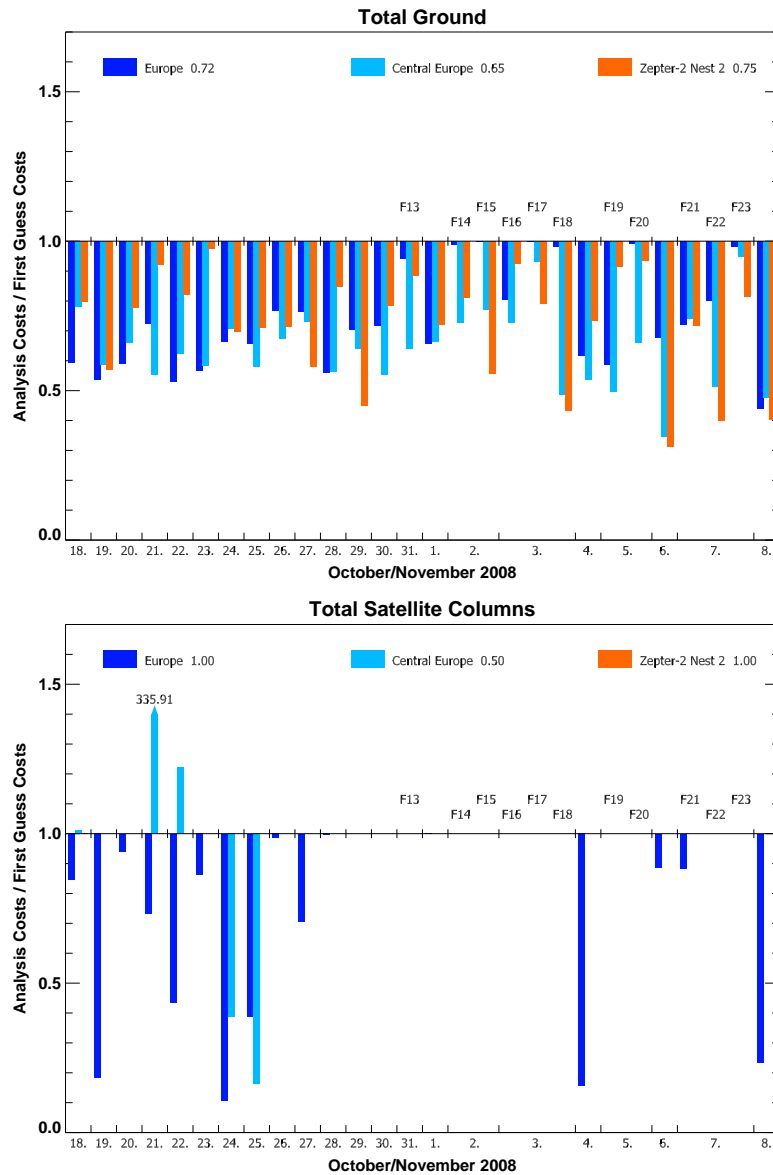


**Figure 5.18:** Relative cost reduction displayed as Analysis costs/First Guess costs. Statistics are displayed for each assimilation window for EUR (dark blue), CEN (light blue), and ZEPTER-2 Nest2 (orange). Assimilations including airborne PND observations are marked with a flight number. The panels display total ground-station observation costs ( $PM_x$ , top) and total satellite columns from SYNAER retrievals (bottom). Values behind the domain descriptors show the average reduction.

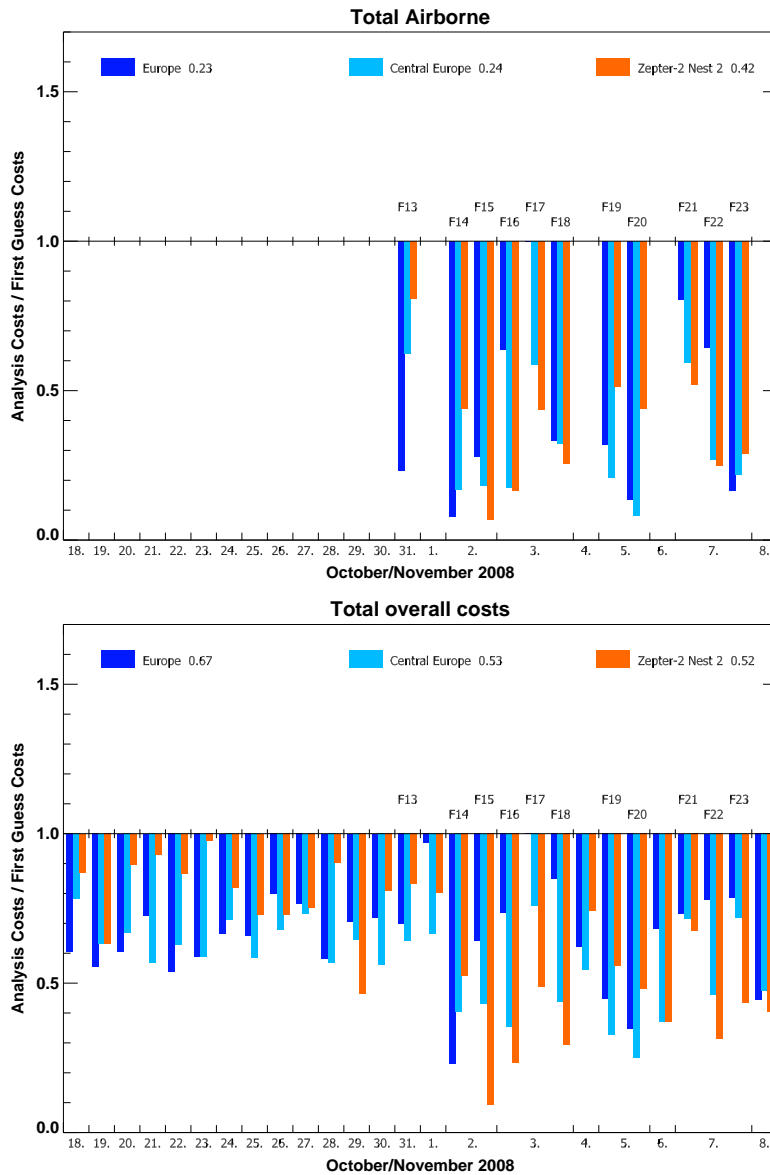


**Figure 5.19:** Relative cost reduction displayed as Analysis costs/First Guess costs. Statistics are displayed for each assimilation window for EUR (dark blue), CEN (light blue), and ZEPTEP-2 Nest2 (orange). Assimilations including airborne PND observations are marked with a flight number. The panels display total airborne observation costs (PND, top) and the overall costs, including background costs (bottom). Values behind the domain descriptors show the average reduction.

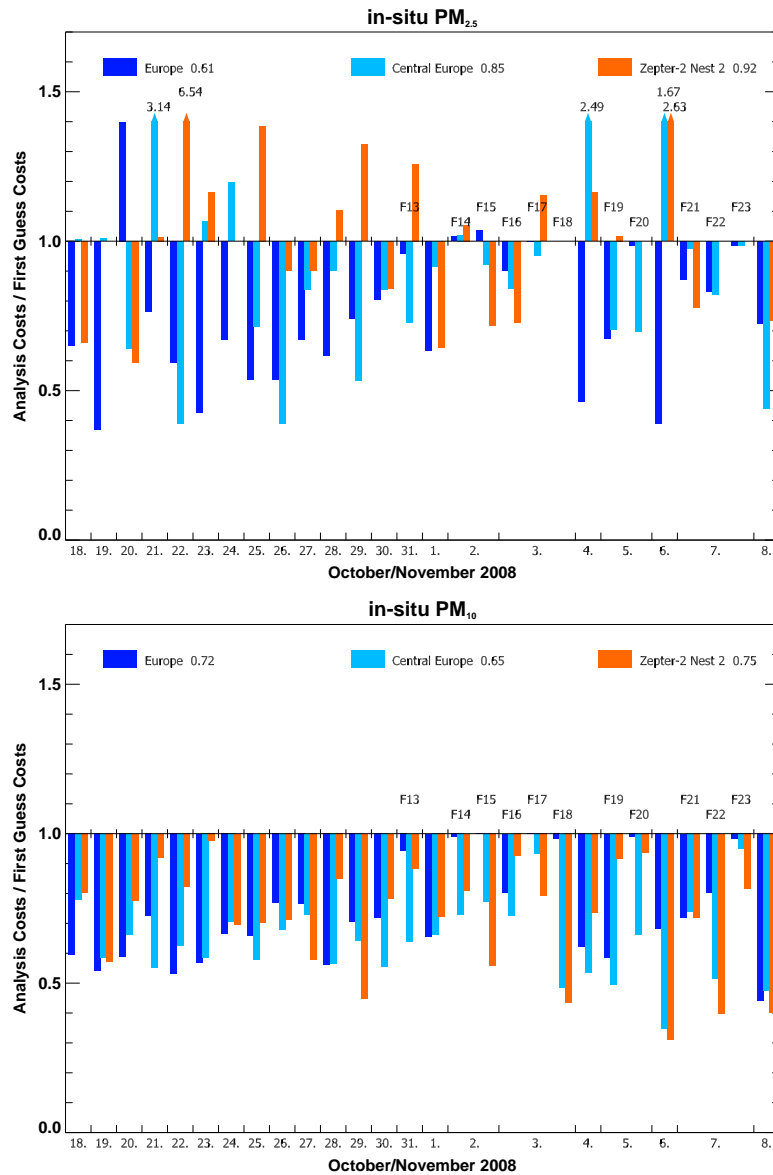


**Figure 5.20:** Comparison of assimilation performance of in-situ  $PM_{10}$  and  $PM_{2.5}$ . Top row: Relative cost reduction displayed as Analysis costs/First Guess costs. Statistics are displayed for each assimilation window for EUR (dark blue), CEN (light blue), and ZEPTER-2 Nest2 (orange). Assimilations including airborne PND observations are marked with a flight number. Total  $PM_{2.5}$  cost reduction (top) and total  $PM_{10}$  costs reduction (bottom). Values behind the domain descriptors show the average reduction.

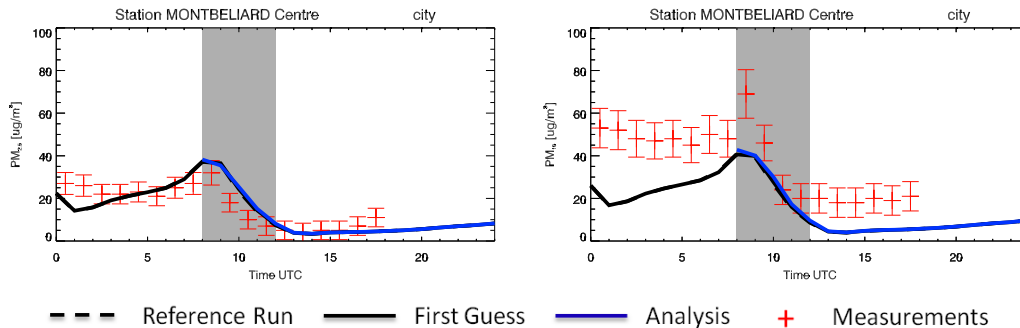


**Figure 5.21:** Time series for  $PM_{2.5}$  (left) and  $PM_{10}$  (right) at the Montbeliard site on October 27, 2008. The grey shaded area indicates the assimilation window.

produce reliable statistics here. On the coarser grids a general cost reduction and, thus, a successful  $PM_{2.5}$  assimilation can be stated.

## 5.2.5 Forecast performance

A comparison of First Guess Run and Reference Run costs for  $PM_{10}$  is taken to measure the beneficial impact of assimilation on the forecast. The ratios of the costs and the RMSE of both is plotted in Figure 5.22 for each day of the campaign and for each grid. These plots have a quite inhomogeneous appearance. While the first days (up to October 20) show a large improvement of the  $PM_{10}$  forecast, a reduction of up to 15% of the RMSE and between 20 and 40 % of costs. On October 21 at about 0 UTC a very broad cold front extending from the Iberian peninsula to northern Finland crossed continental Europe from the north-west. Frontal precipitation washed out almost all of the aerosol on its way southeast. Thus, assimilation information was lost for the affected observation sites, leading to a drastic decrease of forecast improvement. Another cold front of similar characteristics crossed the area from the morning of October 26, lasting until October 31, allowing only small forecast enhancement. During the following days widespread rainfall occurred over Europe excluding the Central European domain. This led to the remarkable situation, that there was a moderate improvement in the *CEN* region, while there was almost no gain for the surrounding *EUR* mother domain.

Steady southerly winds during the period from October 31 to November 6 also prohibited a successful improvement of the forecast for the *ZP2* domain, simply because south of the Alps there were no observations available for the

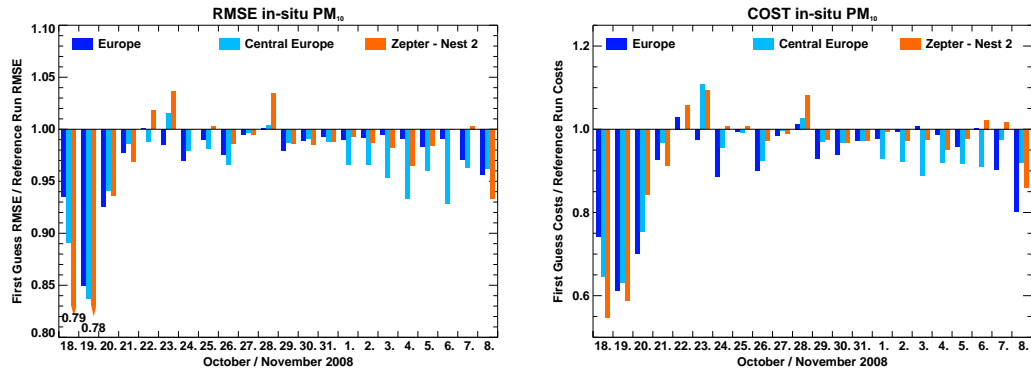


**Figure 5.22:** Forecast performance measured as  $PM_{10}$  First Guess RMSE / Reference Run RMSE (left) and First Guess costs / Reference Run costs (right).

whole campaign episode. This is displayed in Figure 5.17. With an extension of only 440 km in north - south direction, any assimilation information from Austria and Switzerland have crossed this area after several hours. Figure 5.28 gives an impression of how fast information is propagated under these conditions. Another remarkable issue is the decrease in forecast skill for three days in October. On the October 22 and 23, there was an already strong overestimation of  $PM_{10}$  in the area of Luxembourg, which was aggravated by a positive analysis increment. In this case the simulated PBL was very low (50 m, the minimum value) during the whole night. In combination with an analysis increment of approximately  $5\mu g/m^3$  and standard emissions at low winds,  $PM_{10}$  values accumulated to up to  $120\mu g/m^3$ , while, at the same time, measurements only showed aerosol concentrations of  $20 - 40\mu g/m^3$ . This effect degraded the analysis performance significantly. The effect on October 28 was quite similar, except that here, positive analysis increments on the *CEN* domain lead to enhanced overestimation of  $PM_{10}$  induced via increased boundary values. Here, the washout in the parental grid has probably been underestimated resulting in boundary values that were too high. This effect can be observed in a broad belt covering the regions from Nancy and Strasbourg to Mannheim.

Additionally, the daily average Bias of  $PM_{10}$  for each domain is displayed in Figure 5.23. In contrast to the very dry episode of July 2003 discussed in section 5.1, the improvement of the Bias is rather moderate, although there is a broader coverage in terms of surface area concerning  $PM_x$  observations. While there was a relative reduction of about 30% in the 2003 episode, there is a reduction of only about 10 – 20% in 2008. This is mainly due to the more variable meteorological situation, the effect of which is reflected best in the

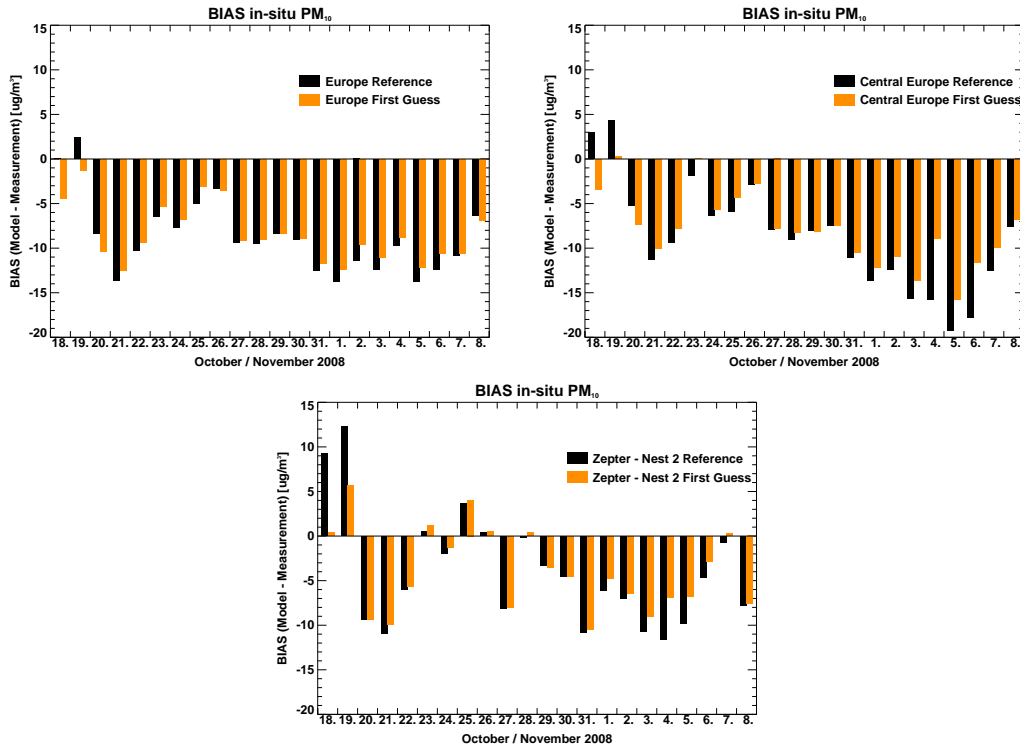


**Figure 5.23:** Daily average  $PM_{10}$  Bias of the Reference Run (black) and the First Guess Run (orange) for the domains EUR (top left), CEN (top right), and ZP2 (bottom).

*EUR* domain Bias. There is a constant small to none reduction, while there is a moderate reduction in the *CEN* and *ZP2* domains on days with favorable weather conditions, which prevailed between November 1 and 6. In general, one assumes that the Bias should decrease with resolution, i.e. from the *EUR* down to the *ZP2* domain. This is the case on the first days until October 24, where meteorological conditions are more or less equal for each domain. The reason why the Bias is lower on the *EUR* domain in the second half of the campaign are comparably low aerosol concentrations in the rest of Europe and since the model generally underestimates aerosols, consequently there is a lower average Bias in this period.

To further illustrate the effect of assimilation on nested grids a comparison of the model systems behavior around two rather similar  $PM_{10}$  sites is displayed in Figure 5.24. The two sites chosen are Istanbul-Aksaray and Munich-Stachus. Both are considered *traffic* sites, i.e. they are located near a major road. The images in the top row show the direct comparison of  $PM_{10}$  assimilation and

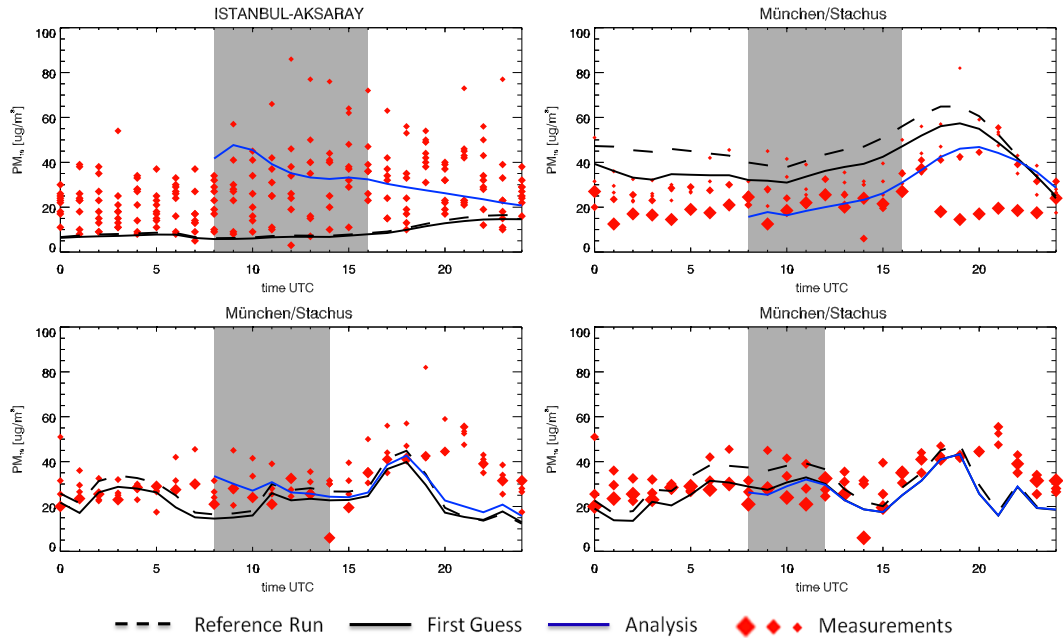


**Figure 5.24:** Comparison of two  $PM_{10}$  city-sites on October 19, 2008. The images display Reference Run, First Guess, Analysis Run, and Observations. The size of the diamonds indicates the reciprocal error of the respective measurement. The grey shaded area denotes the assimilation window. Top left: Istanbul-Aksaray (EUR domain, 9 sites/grid cell). Top right: Munich-Stachus (EUR domain, 5 sites/grid cell). Bottom left: Munich-Stachus (CEN domain, 4 sites/grid cell). Bottom right: Munich-Stachus (ZP2 domain, 3 sites/grid cell).

forecast on October 19, 2008 in the grid cells the respective sites are located in. The first and most conspicuous feature is that there are many very different measurements inside a single grid cell, nine in Istanbul and five in Munich. The model, of course, only provides one representative value per grid cell, and here, it is obvious, that the representativity of one value for a  $45 \times 45 km^2$  is limited. In both cases, there is a clear shift between Analysis Run and First Guess Run showing a much more realistic course. On second sight another phenomenon becomes apparent. While Munich is located quite in the center of the mother domain *EUR* surrounded by a dense net of observations, Istanbul is located in an area with only sparse measurements. This is reflected in the First Guess (black solid line) at both sites. On the one hand there is a considerable shift of  $5 - 10 \mu g/m^3$  towards the measurements between Reference and First Guess Run in Munich, because there is almost no beneficial influence from an earlier assimilation in Istanbul. Furthermore, inspecting the

simulations in the daughter domains for Munich reveals that both, Reference Run and First Guess Run, are already much closer to the observations and that there is only a small correction necessary on the *CEN* domain and almost none on the *5km ZP2* grid. (The reason for the different sizes of the diamonds for the same measurement on different nests is that the error of representativity for each observation is depending on the resolution of the grid).

### 5.2.6 Optimised Particle Number Densities

The novel assimilation of particle number densities will be discussed in detail here and flight 14 has been chosen as a representative example. Its track along with the observed  $PND_3$  (number density of particles with a diameter between  $5\text{ nm}$  and  $3\text{ }\mu\text{m}$ ) is shown in Figure 5.25. A set of time series of this flight for each of the three domains is plotted in Figure 5.26. Each of the three plots shows the same observations (red crosses). But, not only do the background values differ due to distinct resolutions. Also the model layer in which the instrument is located at a certain time can deviate.

Due to the complex meteorological conditions described above, there is no influence from preceding assimilation instances that day and, thus, there is no difference between the First Guess and the Reference Run (black solid line) here, i.e. the First Guess is in compliance with the Reference Run. Assimilation on the *EUR* grid (upper left) shows a clear overestimation of  $PND_3$  by a factor of about two (averaged over the whole period of the flight). This large deviation is mainly an effect of the vertical mismatch of the model.

While the accumulation mode particle number densities do not vary very much within the boundary layer, one can find a strong variation in the Aitken mode, whose particles are mostly formed near surface by emissions of biogenic or combustion processes. This is principally due to aerosol aging, i.e. particle growth by condensation and coagulation, thus reducing the amount of Aitken mode particles rather quickly. Since  $PND_3$  has a large contribution from the Aitken mode particles it is

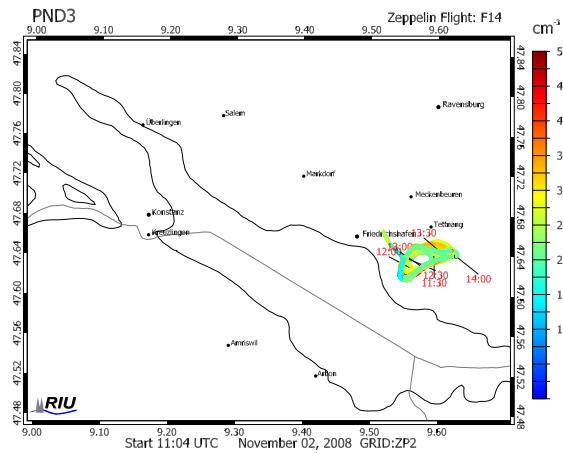


**Figure 5.25:** Measured  $PND_3$  along the track of flight F14 on November 2, 2008 over the forest of Tettwang.

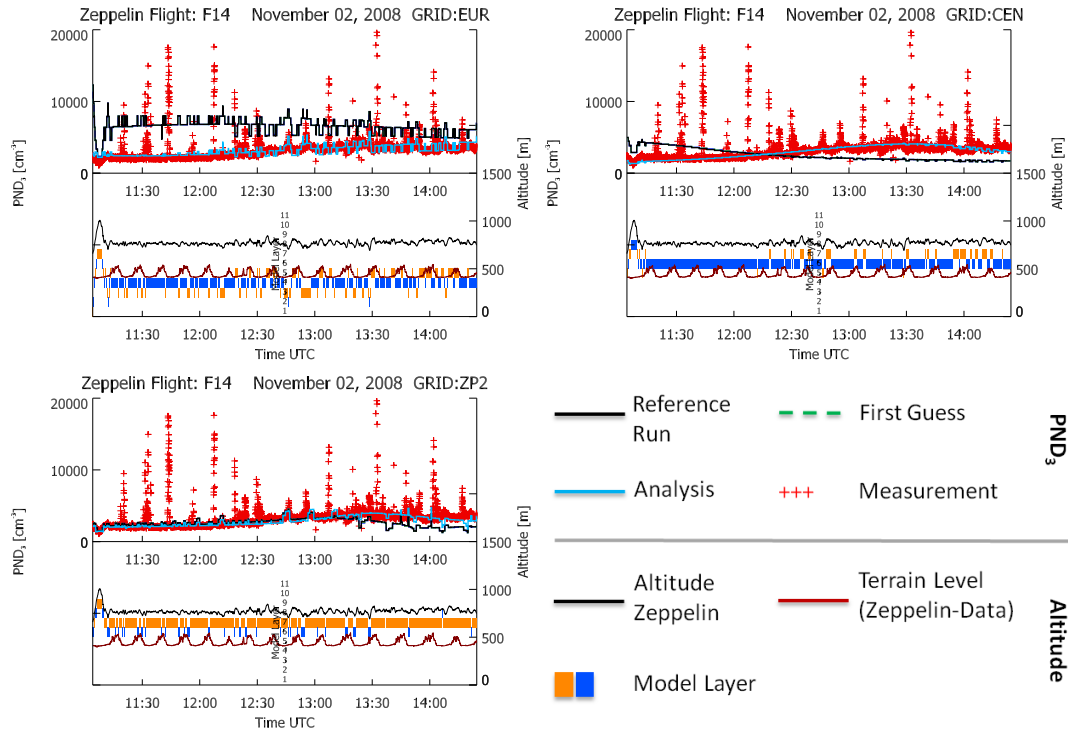


**Figure 5.26:** Particle Number Densities  $PND_3$  of flight F14 assimilated from 11 to 15 UTC on November 2, 2008, on the different domains EUR (top left), CEN (top right), and ZP2 (lower left). Orange and blue bars in the lower half denote model layer of the Zeppelin. The layer number is given in the centered column.

also subject to aerosol aging. This strong height dependence is also reflected in the obvious strong anti-correlation between the model layer (orange/blue bars) and the Reference Run  $PND_3$  (black solid line) on the EUR domain, where the Zeppelin is located mainly in model layer three and four (approx. 110m a.g.) because the terrain level is an average over an area of  $45 \times 45 km^2$  which, here, is 700m a.s.. In the CEN domain the model already represents the proper magnitude though still one layer to low (mostly layer six, approx. 260m a.g.) and with a misfit in the curve (model values decrease, while measurements increase). This misfit is almost removed on the ZP2 domain with its higher resolution of 5km. Here, the observations are mainly located in model layer seven (approximately 350m a.g.) which is quite exactly the height given as the difference between the altitude of the Zeppelin (black solid line in lower part of the plots) and the terrain-height (dark red solid line). Although there were very different conditions on the different domains, the assimilation system

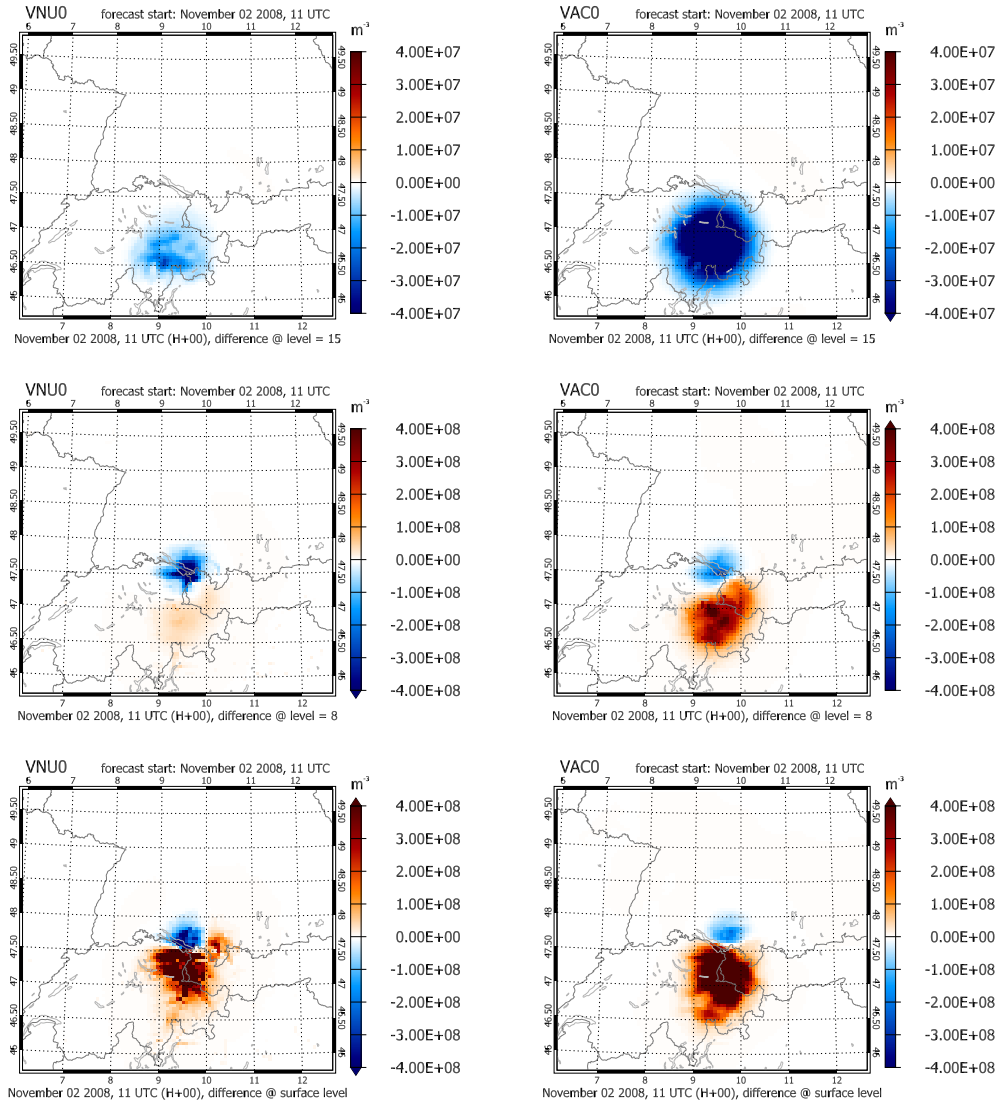


**Figure 5.27:** Analysis increments of particle number densities for Aitken (left panels) and accumulation mode (right panels) from ZP2 domain assimilation. Top row: Layer 15 (1900m). Center row: Layer 8 (450m). Bottom row: Surface Layer.

managed to reproduce the observed values very well on each single grid (blue solid line) with only one concession: The peaks in the measurements that are related to plumes from traffic emissions could not be reproduced. This is due to their small spatial and temporal extension.

Figure 5.27 shows the analysis increment on the ZP2 domain for flight 14.

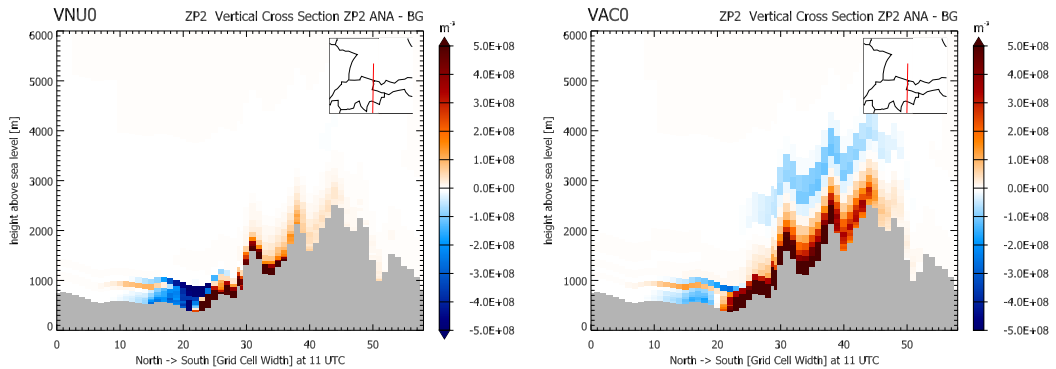


**Figure 5.28:** Vertical cross section of analysis increments of particle number densities for Aitken (left panel) and accumulation mode (right panel) from assimilation of flight 14 on November 2, 2008, 11 UTC. Cross section is made along the red line in the small map inlay from north to south. Terrain height is plotted in grey. Left: Aitken mode number density. Right: Accumulation mode number density.

Values are presented for Aitken and accumulation mode in three different layers: The surface layer, layer 8 (approx. 450m a.g.), and layer 15 (approx. 1900m a.g.). The small negative increments in layer 15 (the scale is reduced by a factor of five in comparison to the plots of the other layers) apparently derive from the small negative correction that can be observed before 13 UTC in the *ZP2* plot displayed in Figure 5.26. The same accounts for the negative increments in the other layers. The larger positive increments affect the air masses which are passed by the Zeppelin after 13 UTC, when there is a positive correction compared to the model in *PND*.

In this case, it is easy to see where the air masses that influence the model at time and location of a measurement come from. Figure 5.28 gives an insight of the vertical distribution of increments. Here, negative increments can be found in the Lake Constance area and in elevated layers over the Alps, where stronger winds are prevailing. These negative increments at 11 UTC have a maximum backward travel-time of two hours because afterwards there is an underestimation of the simulation (the black solid line in the lower left panel in Figure 5.26). Inspecting the total spread of the layer 15 negative increments compound (upper row in Figure 5.27) reveals that its southernmost extensions have already crossed the boundaries of the *ZP2* domain. This means that in terms of initial value optimisation all this information is lost. Even more, gradients from the second half of flight 14 do not have any influence on the simulation anymore. The initial values that had to be optimised are situated in northern Italy.

### 5.2.7 Summary

In general, this second episode showed that aerosol assimilation on grids with higher resolution brings much additional gain. Especially, with regard to the very complex meteorological situation. Assimilation proved stable on limited assimilation timescales (four hours on the *ZP2* domain) and at least a moderate improvement of forecast could be achieved for most of the days of the episode chosen.

Assimilation of *PND* in general can be considered as valuable. Although these observations were very many within a small period of time and resolving features on a very small spatial scale, the assimilation system proved to be capable of reproducing almost all of them. Here, the necessity of simulating on high resolution grids became most obvious. In the region around Lake Constance a 5 km *ZP2* terrain is needed to reasonably well represent its special orography. The prevalence of assimilated *PND*<sub>3</sub> could only in parts be verified. Due to the spatial limitations of the flight track only simulations of subsequent flights on the same day could be expected to be affected by previous assimilation. The First Guess Runs for flights 15 and 23 exhibited a small influence and for flights 20 and 22 a very small impact could be proven. This low influence of assimilation on observations of subsequent flights can be explained with the fact that most often the effects of assimilation had already been transported out of the region. Plots for all flights can be found in appendix C.

## CHAPTER 6

---

### Conclusions and Outlook

---

A 4D-var system for aerosols has been implemented as an extension to the existing gas-phase assimilation system. Along with the aerosol assimilation system some new observations came up very different in nature. On the one side type resolved aerosol optical thicknesses with large footprints, on the other side spatially and temporally extremely high resolved particle number densities. Altogether, they stood the test in two, also, very different episodes.

At first, the episode of July 2003 was selected, because there were a lot SYNAER retrievals available. The remote sensing instruments benefited from a very hot period which was mainly cloud free. This, at the same time brought along the subject of interest: A heavy aerosol burden from dry soil and large wildfires over wide areas of Europe. Here, the assimilation of the type-resolved SYNAER retrievals has been tested. The large amounts of aerosols from the wildfires were represented by the analysis very well. Especially the assimilation of *SOOT* and *WASO* was very successful. These were the species where the background values were approximately of the magnitude of the measurements. Another success was the assimilation of long-range transported mineral dust (*DUST*) in elevated layers above the mixing layer. Here, a special difficulty occurred. The measured values were much higher than the simulated ones which was not unrealistic, because the places of origin, the Saharan desert, lay outside of the model domain and thus could not be simulated. The chosen remedy to reduce the observation error in order to give it more weight worked fine on the one side, but on the other sometimes inhibited a proper assimilation

of other species. A little bit less successful was the assimilation of *INSO* and *SEAS*. This was mainly due to being too far away from the background values. In the case of *SEAS* it was also even difficult to evaluate the improvement induced by assimilation, since there were so few observations available.

Summarising this part it has to be stated, that the results are satisfying, but a few problems are still to overcome. On some episode days an overestimation of *WASO* over water was accompanied by an underestimation of the same air parcel over land. Here, it is possible, that this is due to two different retrieval algorithms that are used. Furthermore, as proposed by *Holzer-Popp* [2011], a bias correction should be applied to all SYNAER retrieval values. To further address the problem of adequately assimilating mineral dust, it would be interesting to observe the models behavior on a larger grid where the sources of dust in northern Africa are included. Another approach would be to introduce a flag variable for cases where the model has a “lack of knowledge”. This flag variable would have to be implemented into the forward and backward model code similar to a tracer species. This way, numerical stability could be ensured for the minimisation, since, opposing to the method chosen in this study, the background error could be increased instead of decreasing the observation error. This would lead to a better conditioning of the system.

The ZEPTEP-2 episode was a pure measurement campaign and, therefore, scheduled in advance. The meteorological conditions were sometimes extreme concerning data assimilation. Often, the information was literally washed away by the rain. Nevertheless, this episode brought a lot of interesting understanding. First of all, before being able to assimilate particle number densities from the CPC, the model itself was put to a test concerning Aitken mode number densities. They turned out to be much too high. The reason is, that measurements of very small particles have just become available recently and the standard values were only reasonable estimates. Afterwards, assimilation of *PND* appeared to be very effective, although it quickly became obvious that an assimilation window of four hours was too long for measurements gathered in higher model layers. Their information had already been transported out of the model domain. This leads to another phenomenon. Taking a look at the flight plots shows the differences of the layers in which the measurements are situated depending on the model domain. It turned out that the 5 km grid terrain elevation is in a good accordance to the elevations measured on board the Zeppelin and that its model values resemble the observations most.

A further insight is that nesting into higher resolved grids does improve the aerosol forecast. This could be observed on most of the sites within the nested domains when comparing the simulations on different grids.

In general, it has to be stated that, besides the innovations concerning new types of measurements, the aerosol 4D-var system yields a significant improvement for the forecast of aerosols. This is also due to the dense net of  $PM_{10}$  measurements spread over Europe.

For future research, the opposing predictions for the available  $PM_x$  observations (underestimation of  $PM_{10}$  and at the same time and place an overestimation of  $PM_{2.5}$ ) indicate, that a deeper look should be taken on the separation of background aerosol mass concentrations between the modes. Additionally, it would be helpful to have another comprehensive dataset of species resolved aerosol observations for validation.



# APPENDIX A

---

## Vertical Grid Structure

---

**Table A.1:** The vertical structure of the model grid, defined by terrain following  $\sigma$  coordinates. Pressures and heights are valid for a surface pressure of 1013.25 hPa at U.S. standard atmosphere.

| Layerindex | $\sigma$<br>value | Pressure<br>[hPa] | Height<br>[m] |
|------------|-------------------|-------------------|---------------|
| surface    | 1.000             | 1013.25           | 0             |
| 1          | 0.995             | 1008.68           | 38            |
| 2          | 0.990             | 1004.12           | 76            |
| 3          | 0.985             | 999.55            | 115           |
| 4          | 0.980             | 994.99            | 153           |
| 5          | 0.970             | 985.85            | 231           |
| 6          | 0.960             | 976.72            | 309           |
| 7          | 0.945             | 963.02            | 427           |
| 8          | 0.930             | 949.32            | 546           |
| 9          | 0.910             | 931.06            | 708           |
| 10         | 0.890             | 912.79            | 872           |
| 11         | 0.865             | 889.96            | 1081          |
| 12         | 0.840             | 867.13            | 1294          |

---

| Layerindex | $\sigma$<br>value | Pressure<br>[hPa] | Height<br>[m] |
|------------|-------------------|-------------------|---------------|
| 13         | 0.810             | 839.73            | 1556          |
| 14         | 0.780             | 812.34            | 1825          |
| 15         | 0.740             | 775.81            | 2196          |
| 16         | 0.700             | 739.28            | 2581          |
| 17         | 0.600             | 647.95            | 3615          |
| 18         | 0.500             | 556.63            | 4775          |
| 19         | 0.400             | 465.30            | 6101          |
| 20         | 0.300             | 373.98            | 7658          |
| 21         | 0.200             | 282.65            | 9560          |
| 22         | 0.100             | 191.33            | 12064         |
| 23         | 0.000             | 100.00            | 16179         |

## APPENDIX B

---

### Available ZEPTER-2 Measurements

---

A brief summary on all available Observations is given in the following tables.

**Table B.1:** Number of available EEA in-situ stations and total number of  $PND_3$  and SYNAER AOT observations for the 45 km EUR grid.

|        |     | Assim.<br>window | $PND_3$ | $PM_{10}$ | $PM_{2.5}$ | WASO | INSO | SOOT | SEAS | DUST |
|--------|-----|------------------|---------|-----------|------------|------|------|------|------|------|
| Oct 18 |     | 08 - 16          |         | 1516      | 26         | 54   | 37   | 9    | 1    | 4    |
| Oct 19 |     | 08 - 16          |         | 1504      | 26         | 117  | 76   | 45   | 5    | 1    |
| Oct 20 |     | 08 - 16          |         | 1512      | 26         | 77   | 38   | 38   | 4    | 3    |
| Oct 21 |     | 08 - 16          |         | 1510      | 26         | 45   | 25   | 13   | 4    | 6    |
| Oct 22 |     | 08 - 16          |         | 1517      | 26         | 66   | 50   | 17   | 4    | 1    |
| Oct 23 |     | 08 - 16          |         | 1521      | 26         | 58   | 30   | 23   | 3    | 1    |
| Oct 24 | F08 | 08 - 16          | 59      | 1522      | 26         | 28   | 27   | 4    |      |      |
| Oct 25 |     | 08 - 16          |         | 1519      | 26         | 13   | 11   | 5    | 1    |      |
| Oct 26 |     | 08 - 16          |         | 1505      | 26         | 66   | 29   | 34   | 6    | 5    |
| Oct 27 |     | 08 - 16          |         | 1524      | 26         | 52   | 41   | 18   |      | 2    |
| Oct 28 |     | 08 - 16          |         | 1523      | 26         | 8    | 4    | 5    |      | 1    |
| Oct 29 |     | 08 - 16          |         | 1525      | 26         |      |      |      |      |      |
| Oct 30 |     | 08 - 16          |         | 1519      | 26         |      |      |      |      |      |
| Oct 31 | F13 | 15 - 23          | 4907    | 1519      | 26         |      |      |      |      |      |
| Nov 01 |     | 08 - 16          |         | 1511      | 26         | 46   | 9    | 20   | 11   | 20   |
| Nov 02 | F14 | 11 - 15          | 6013    | 1504      | 26         |      |      |      |      |      |
|        | F15 | 15 - 23          | 4496    |           |            |      |      |      |      |      |
| Nov 03 | F16 | 10 - 13          | 5273    | 1517      | 26         |      |      |      |      |      |
|        | F17 | 13 - 18          | 7185    |           |            |      |      |      |      |      |
|        | F18 | 18 - 24          | 4632    |           |            |      |      |      |      |      |
| Nov 04 |     | 08 - 16          |         | 1518      | 26         |      |      |      |      |      |
| Nov 05 | F19 | 11 - 15          | 6141    | 1525      | 26         |      |      |      |      |      |
|        | F20 | 16 - 24          | 8018    |           |            |      |      |      |      |      |
| Nov 06 |     | 08 - 16          |         | 1533      | 25         |      |      |      |      |      |
| Nov 07 | F21 | 09 - 13          | 6034    | 1532      | 25         |      |      |      |      |      |
|        | F22 | 15 - 17          | 2458    |           |            |      |      |      |      |      |
|        | F23 | 17 - 24          | 5964    |           |            |      |      |      |      |      |

**Table B.2:** Number of available EEA in-situ stations and total number of  $PND_3$  and SYNAER AOT observations for the 15 km CEN grid.

|        |     | Assim.<br>window | $PND_3$ | $PM_{10}$ | $PM_{2.5}$ | WASO | INSO | SOOT | SEAS | DUST |
|--------|-----|------------------|---------|-----------|------------|------|------|------|------|------|
| Oct 18 |     | 08:00 - 14:00    |         | 729       | 4          | 8    | 6    | 1    |      | 1    |
| Oct 19 |     | 08:00 - 14:00    |         | 727       | 4          |      |      |      |      |      |
| Oct 20 |     | 08:00 - 14:00    |         | 729       | 4          |      |      |      |      |      |
| Oct 21 |     | 08:00 - 14:00    |         | 729       | 4          | 1    | 1    |      |      |      |
| Oct 22 |     | 08:00 - 14:00    |         | 733       | 4          | 21   | 14   | 11   | 1    | 1    |
| Oct 23 |     | 08:00 - 14:00    |         | 733       | 4          |      |      |      |      |      |
| Oct 24 | F08 | 08:00 - 14:00    | 59      | 733       | 4          | 4    | 4    | 3    |      |      |
| Oct 25 |     | 08:00 - 14:00    |         | 732       | 4          | 4    | 4    | 3    |      |      |
| Oct 26 |     | 08:00 - 14:00    |         | 730       | 4          |      |      |      |      |      |
| Oct 27 |     | 08:00 - 14:00    |         | 732       | 4          |      |      |      |      |      |
| Oct 28 |     | 08:00 - 14:00    |         | 734       | 4          | 3    |      | 2    |      | 1    |
| Oct 29 |     | 08:00 - 14:00    |         | 738       | 4          |      |      |      |      |      |
| Oct 30 |     | 08:00 - 14:00    |         | 735       | 4          |      |      |      |      |      |
| Oct 31 | F13 | 15:00 - 21:00    | 4907    | 736       | 4          |      |      |      |      |      |
| Nov 01 |     | 08:00 - 14:00    |         | 733       | 4          |      |      |      |      |      |
| Nov 02 | F14 | 11:00 - 15:00    | 6013    | 734       | 4          |      |      |      |      |      |
| Nov 02 | F15 | 15:00 - 21:00    | 4496    | 734       | 4          |      |      |      |      |      |
| Nov 03 | F16 | 10:00 - 13:00    | 5273    | 738       | 4          |      |      |      |      |      |
| Nov 03 | F17 | 13:00 - 18:00    | 7185    | 738       | 4          |      |      |      |      |      |
| Nov 03 | F18 | 18:00 - 24:00    | 4632    | 738       | 4          |      |      |      |      |      |
| Nov 04 |     | 08:00 - 14:00    |         | 733       | 4          |      |      |      |      |      |
| Nov 05 | F19 | 11:00 - 15:00    | 6141    | 736       | 4          |      |      |      |      |      |
| Nov 05 | F20 | 16:00 - 22:00    | 7928    | 736       | 4          |      |      |      |      |      |
| Nov 06 |     | 08:00 - 09:00    |         | 749       | 4          |      |      |      |      |      |
| Nov 07 | F21 | 09:00 - 13:00    | 6034    | 750       | 4          |      |      |      |      |      |
| Nov 07 | F22 | 15:00 - 17:00    | 2458    | 750       | 4          |      |      |      |      |      |
| Nov 07 | F23 | 17:00 - 23:00    | 5964    | 750       | 4          |      |      |      |      |      |

**Table B.3:** Number of available EEA in-situ stations and total number of  $PND_3$  and SYNAER AOT observations for the 5 km ZP2 grid.

|        |     | Assim.<br>window | $PND_3$ | $PM_{10}$ | $PM_{2.5}$ | WASO | INSO | SOOT | SEAS | DUST |
|--------|-----|------------------|---------|-----------|------------|------|------|------|------|------|
| Oct 18 |     | 08:00 - 12:00    |         | 146       | 1          | 8    | 6    | 1    |      | 1    |
| Oct 19 |     | 08:00 - 12:00    |         | 146       | 1          |      |      |      |      |      |
| Oct 20 |     | 08:00 - 12:00    |         | 146       | 1          |      |      |      |      |      |
| Oct 21 |     | 08:00 - 12:00    |         | 146       | 1          |      |      |      |      |      |
| Oct 22 |     | 08:00 - 12:00    |         | 149       | 1          |      |      |      |      |      |
| Oct 23 |     | 08:00 - 12:00    |         | 149       | 1          |      |      |      |      |      |
| Oct 24 | F08 | 08:00 - 12:00    |         | 149       | 1          |      |      |      |      |      |
| Oct 25 |     | 08:00 - 12:00    |         | 149       | 1          |      |      |      |      |      |
| Oct 26 |     | 08:00 - 12:00    |         | 149       | 1          |      |      |      |      |      |
| Oct 27 |     | 08:00 - 12:00    |         | 149       | 1          |      |      |      |      |      |
| Oct 28 |     | 08:00 - 12:00    |         | 150       | 1          |      |      |      |      |      |
| Oct 29 |     | 08:00 - 12:00    |         | 151       | 1          |      |      |      |      |      |
| Oct 30 |     | 08:00 - 12:00    |         | 150       | 1          |      |      |      |      |      |
| Oct 31 | F13 | 15:00 - 19:00    | 4907    | 151       | 1          |      |      |      |      |      |
| Nov 01 |     | 08:00 - 12:00    |         | 151       | 1          |      |      |      |      |      |
| Nov 02 | F14 | 11:00 - 15:00    | 6013    | 151       | 1          |      |      |      |      |      |
| Nov 02 | F15 | 15:00 - 19:00    | 4496    | 151       | 1          |      |      |      |      |      |
| Nov 03 | F16 | 10:00 - 13:00    | 5154    | 151       | 1          |      |      |      |      |      |
| Nov 03 | F17 | 13:00 - 18:00    | 5949    | 151       | 1          |      |      |      |      |      |
| Nov 03 | F18 | 18:00 - 21:00    | 4632    | 151       | 1          |      |      |      |      |      |
| Nov 04 |     | 08:00 - 12:00    |         | 150       | 1          |      |      |      |      |      |
| Nov 05 | F19 | 11:00 - 15:00    | 6121    | 151       | 1          |      |      |      |      |      |
| Nov 05 | F20 | 16:00 - 20:00    | 7260    | 151       | 1          |      |      |      |      |      |
| Nov 06 |     | 08:00 - 09:00    |         | 156       | 1          |      |      |      |      |      |
| Nov 07 | F21 | 09:00 - 13:00    | 5915    | 156       | 1          |      |      |      |      |      |
| Nov 07 | F22 | 15:00 - 17:00    | 2458    | 156       | 1          |      |      |      |      |      |
| Nov 07 | F23 | 17:00 - 21:00    | 5964    | 156       | 1          |      |      |      |      |      |

## APPENDIX C

---

ZEPTER-2 Flights

---

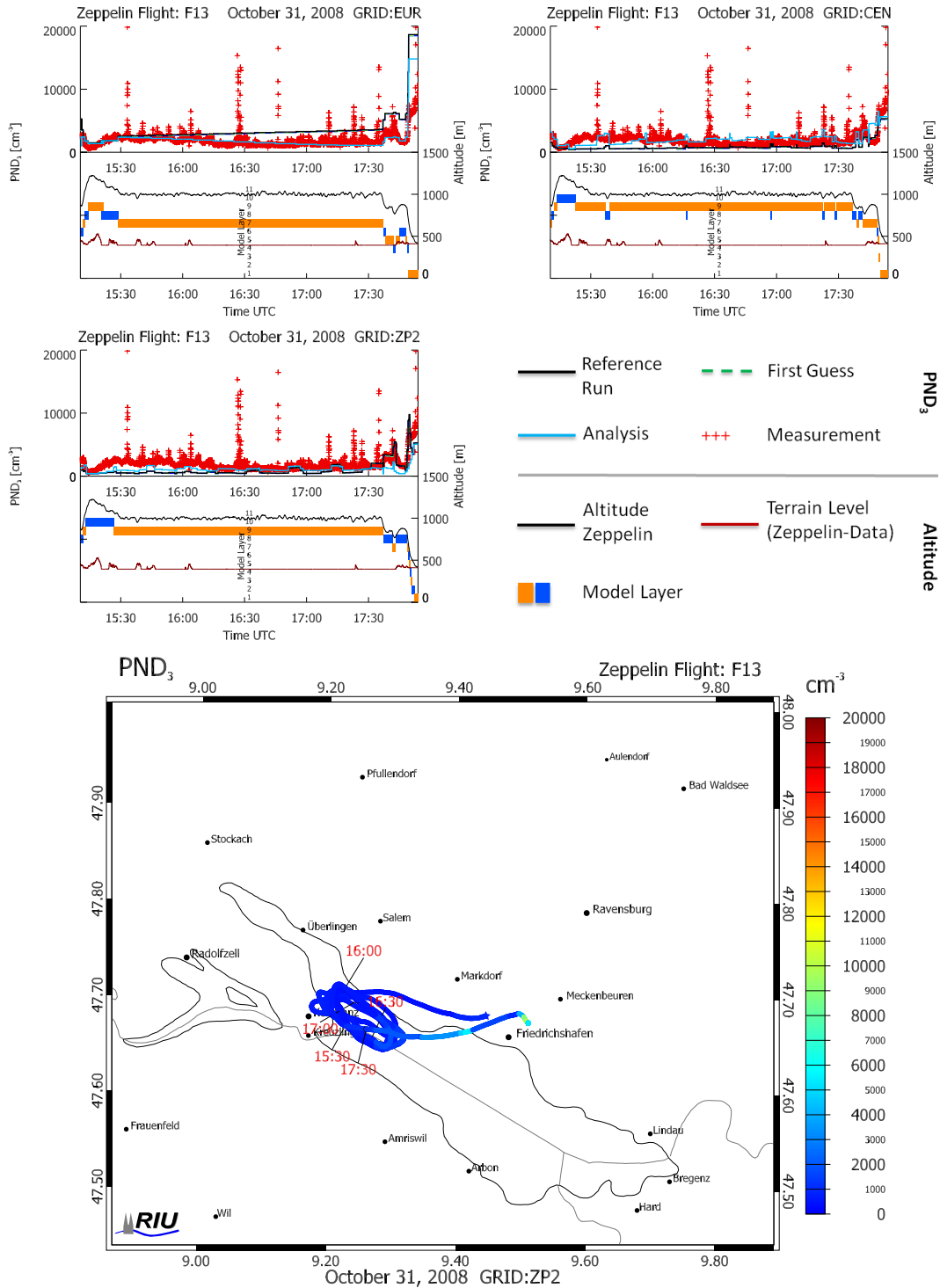
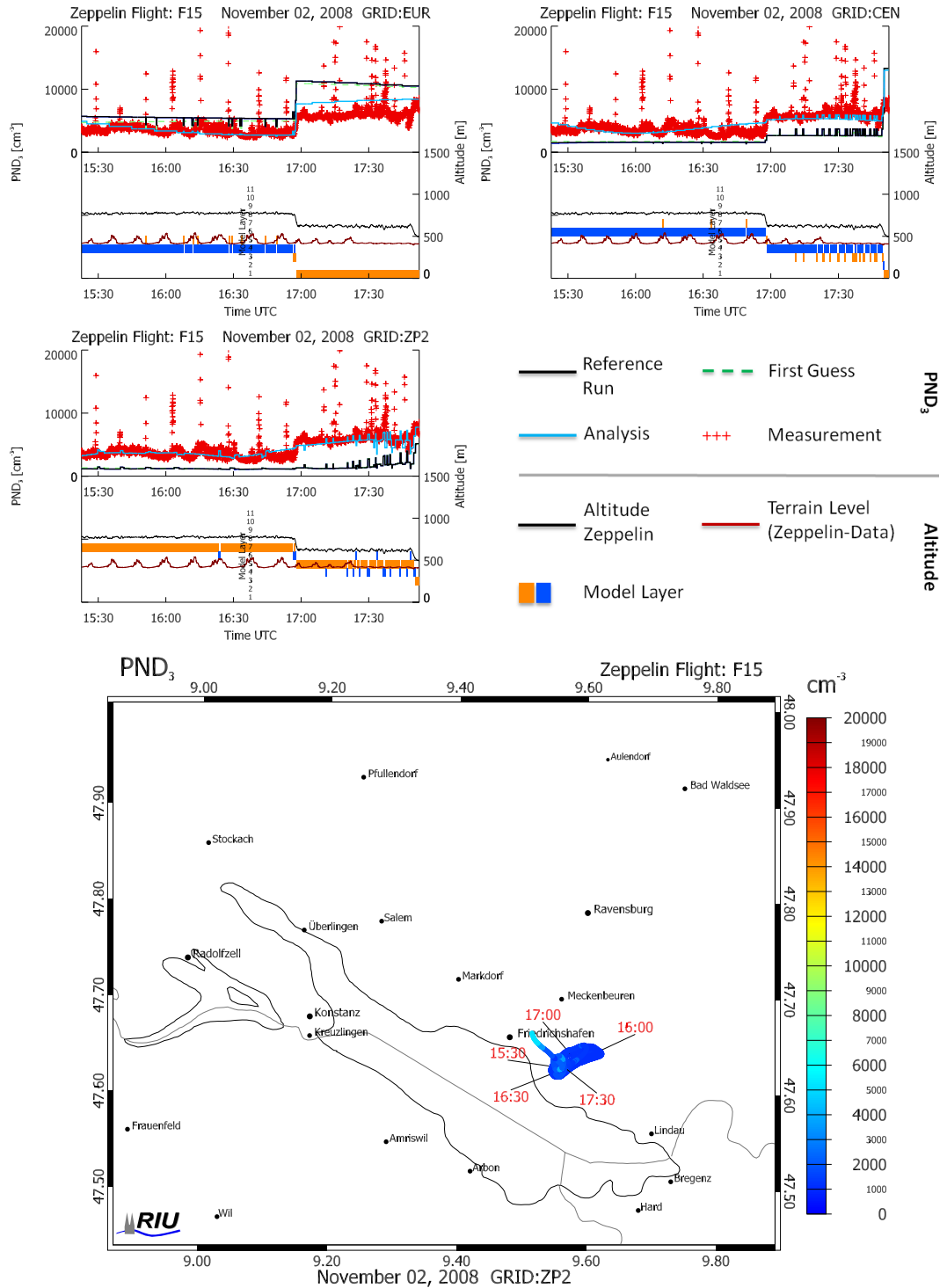
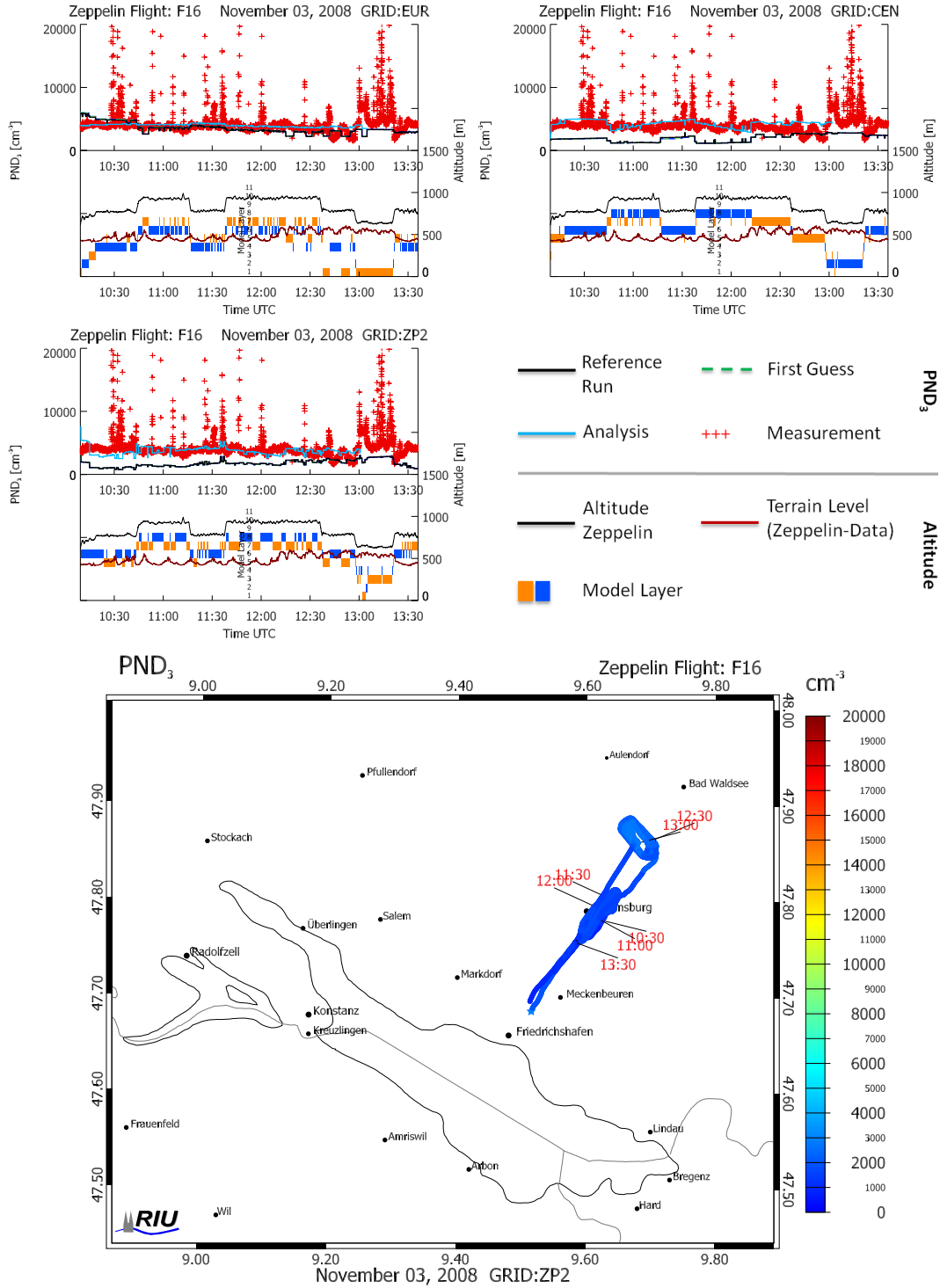


Figure C.1: Particle Number Densities  $PND_3$  of flight F13 assimilated on October 31, 2008, on the different domains EUR (top left), CEN (top right), ZP2 (center left), and flight track with ZP2  $PND_3$  (bottom).



**Figure C.2:** Particle Number Densities  $PND_3$  of flight F15 assimilated on November 2, 2008, on the different domains EUR (top left), CEN (top right), ZP2 (center left), and flight track with ZP2  $PND_3$  (bottom).



**Figure C.3:** Particle Number Densities  $PND_3$  of flight F16 assimilated on November 3, 2008, on the different domains EUR (top left), CEN (top right), ZP2 (center left), and flight track with ZP2  $PND_3$  (bottom).

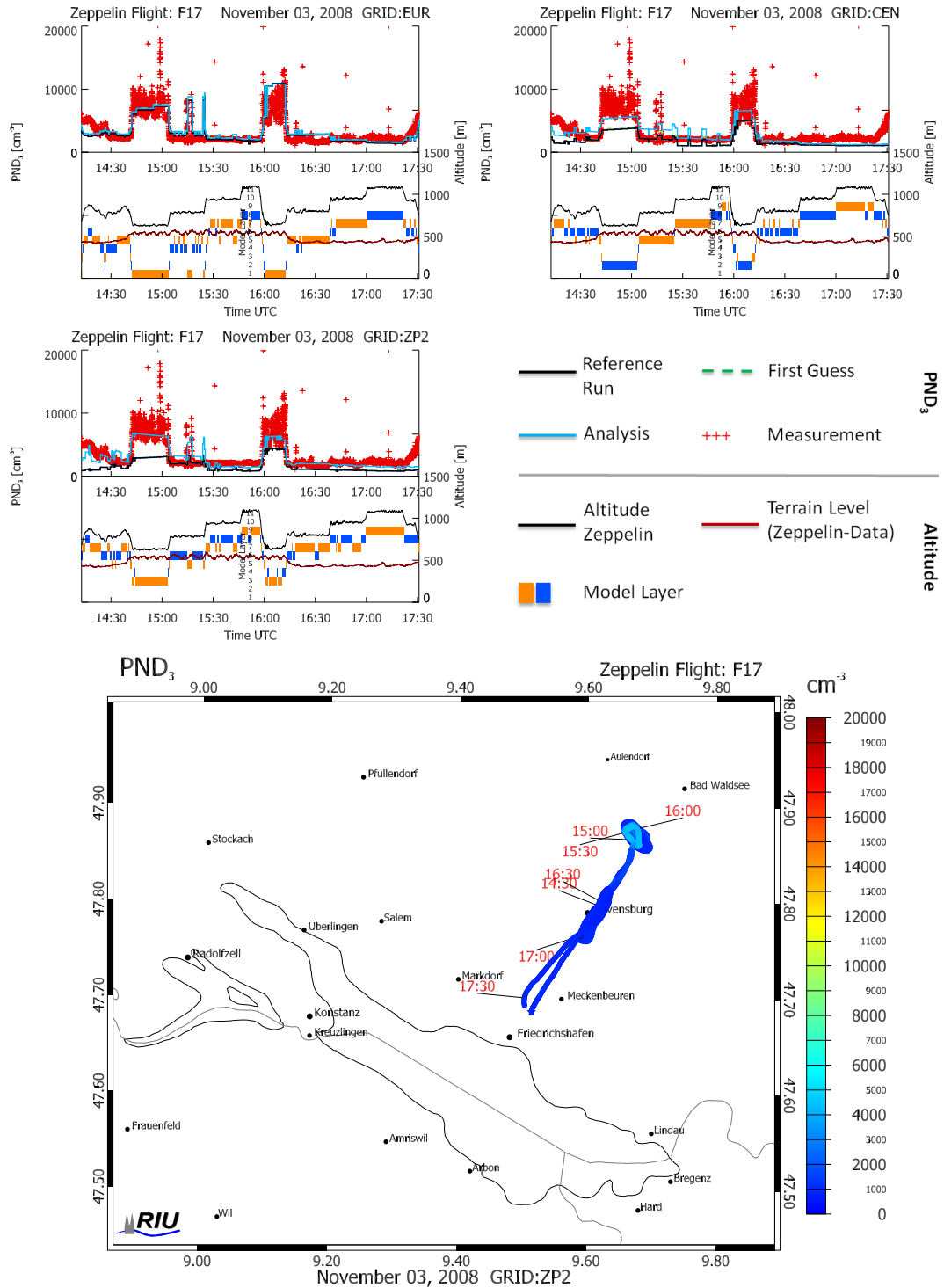


**Figure C.4:** Particle Number Densities  $PND_3$  of flight F17 assimilated on November 3, 2008, on the different domains EUR (top left), CEN (top right), ZP2 (center left), and flight track with ZP2  $PND_3$  (bottom).

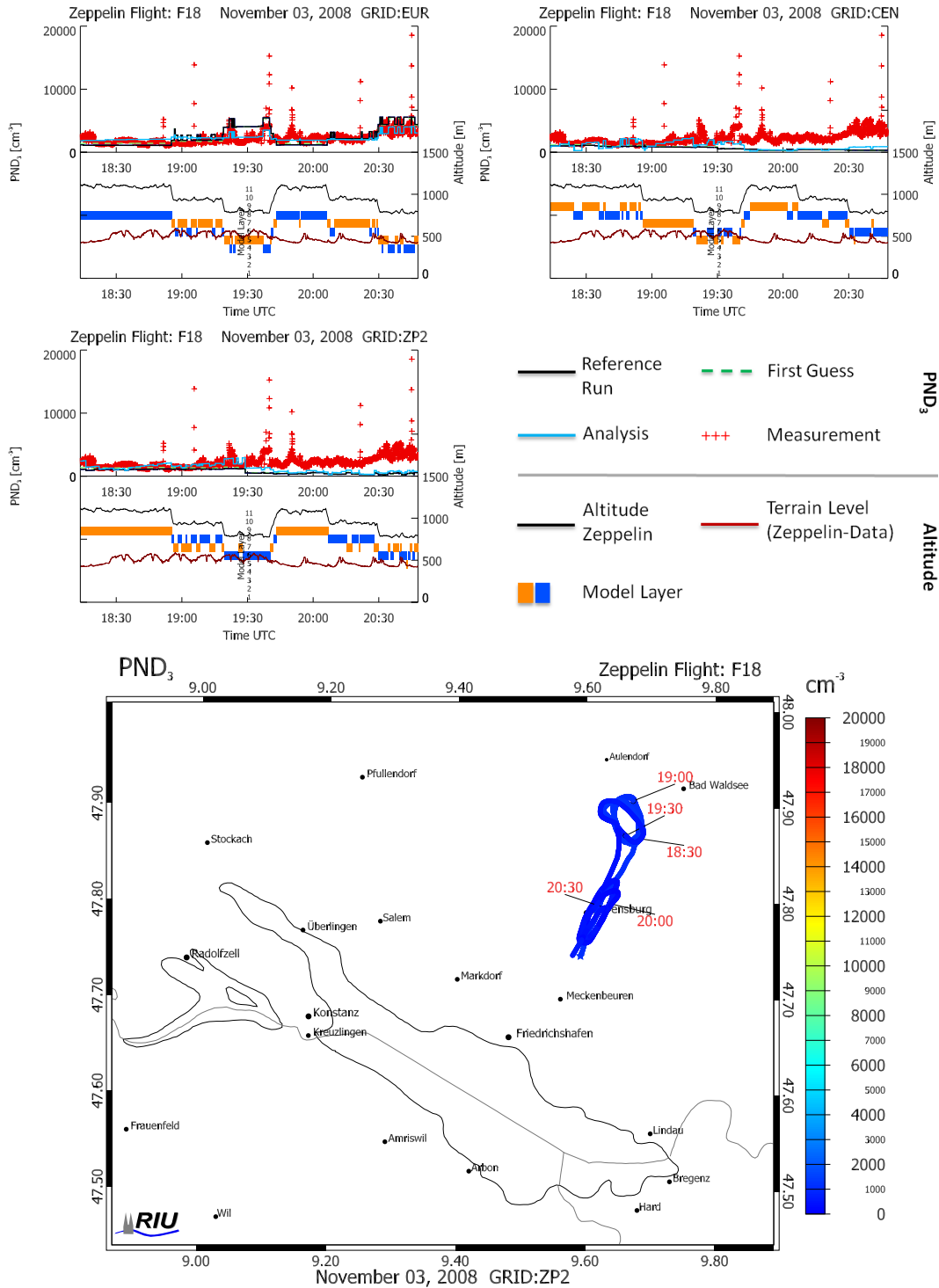
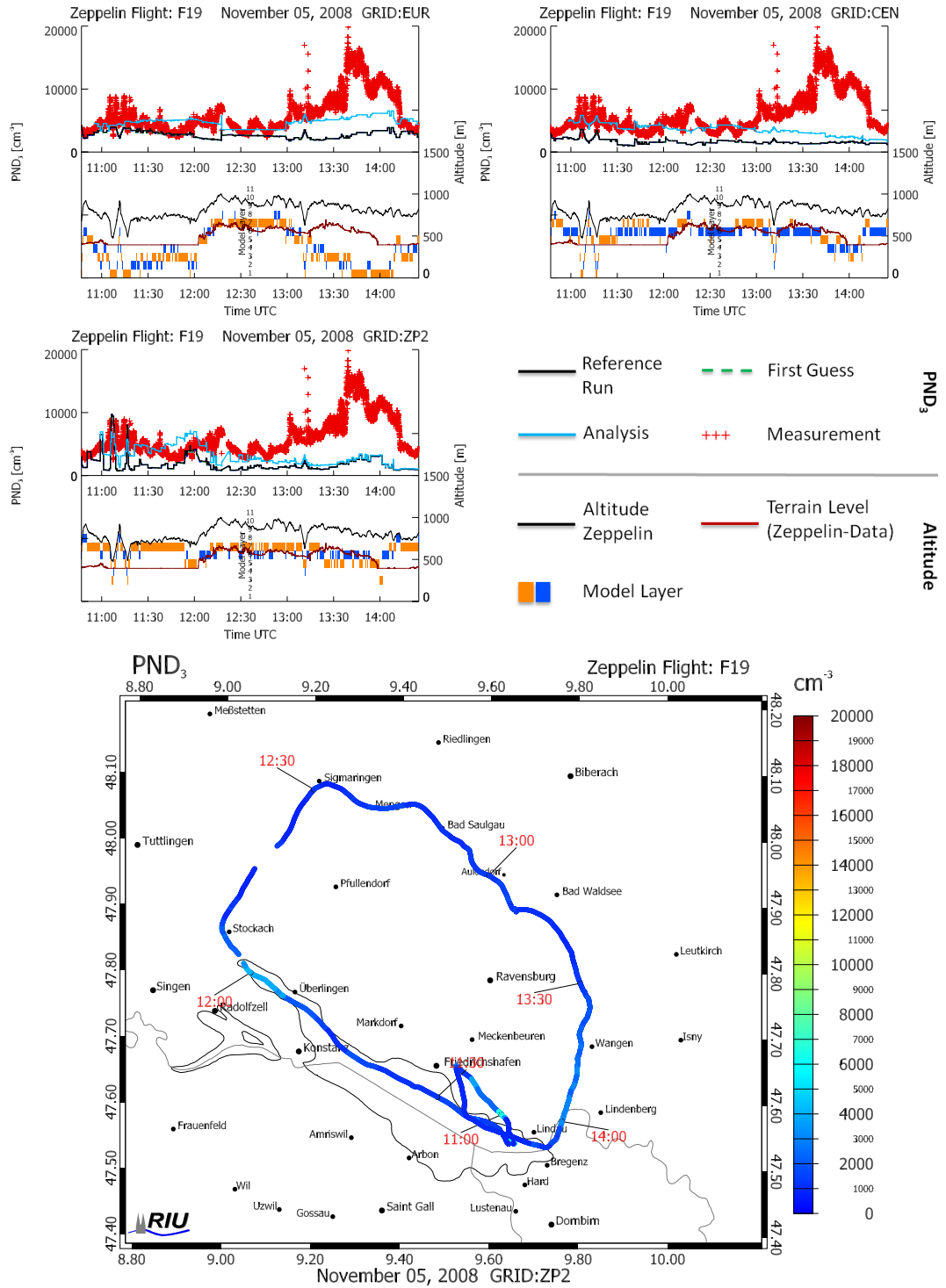


Figure C.5: Particle Number Densities  $PND_3$  of flight F18 assimilated on November 3, 2008, on the different domains EUR (top left), CEN (top right), ZP2 (center left), and flight track with ZP2  $PND_3$  (bottom).



**Figure C.6:** Particle Number Densities  $PND_3$  of flight F19 assimilated on November 5, 2008, on the different domains EUR (top left), CEN (top right), ZP2 (center left), and flight track with ZP2  $PND_3$  (bottom).

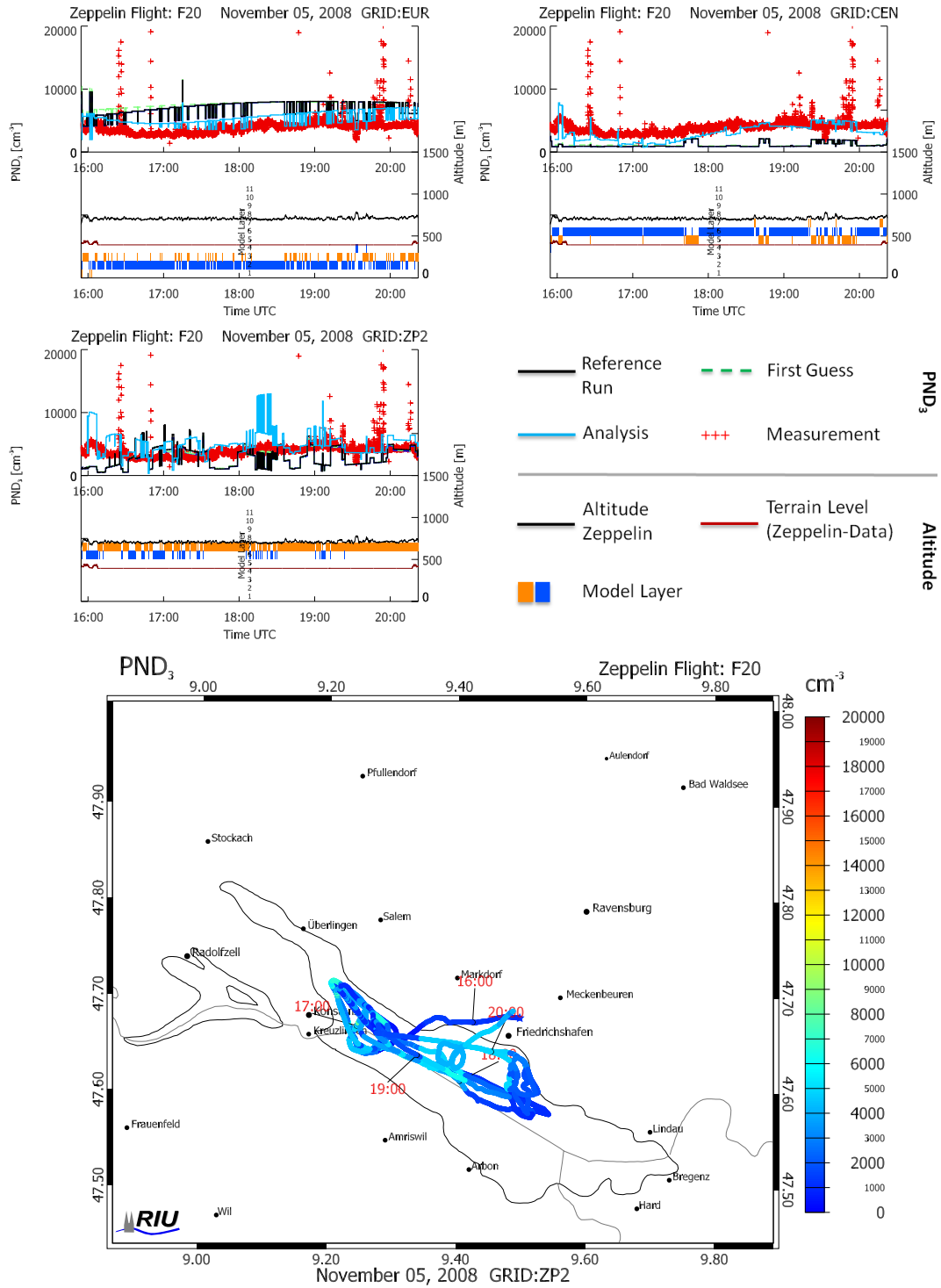
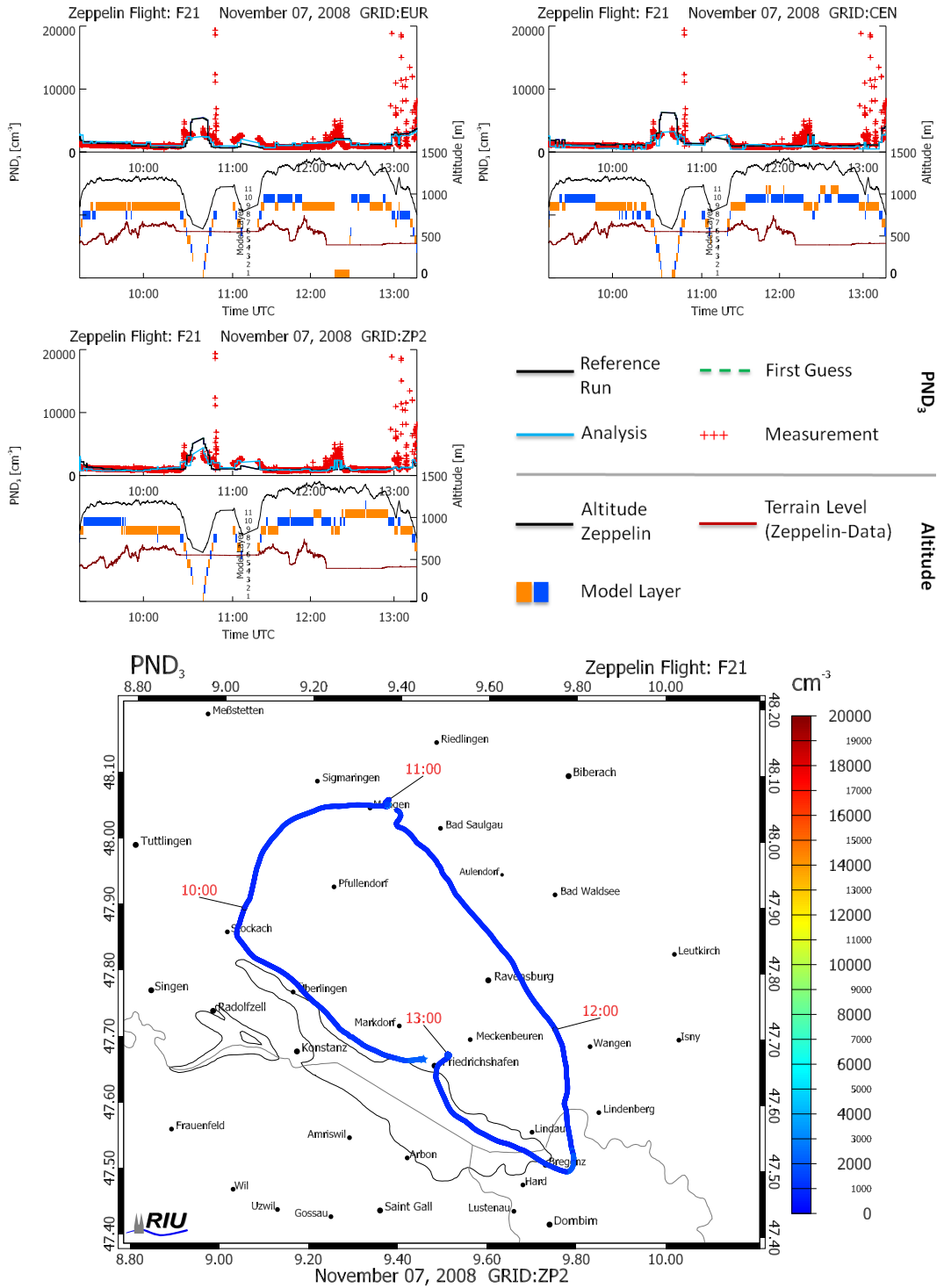
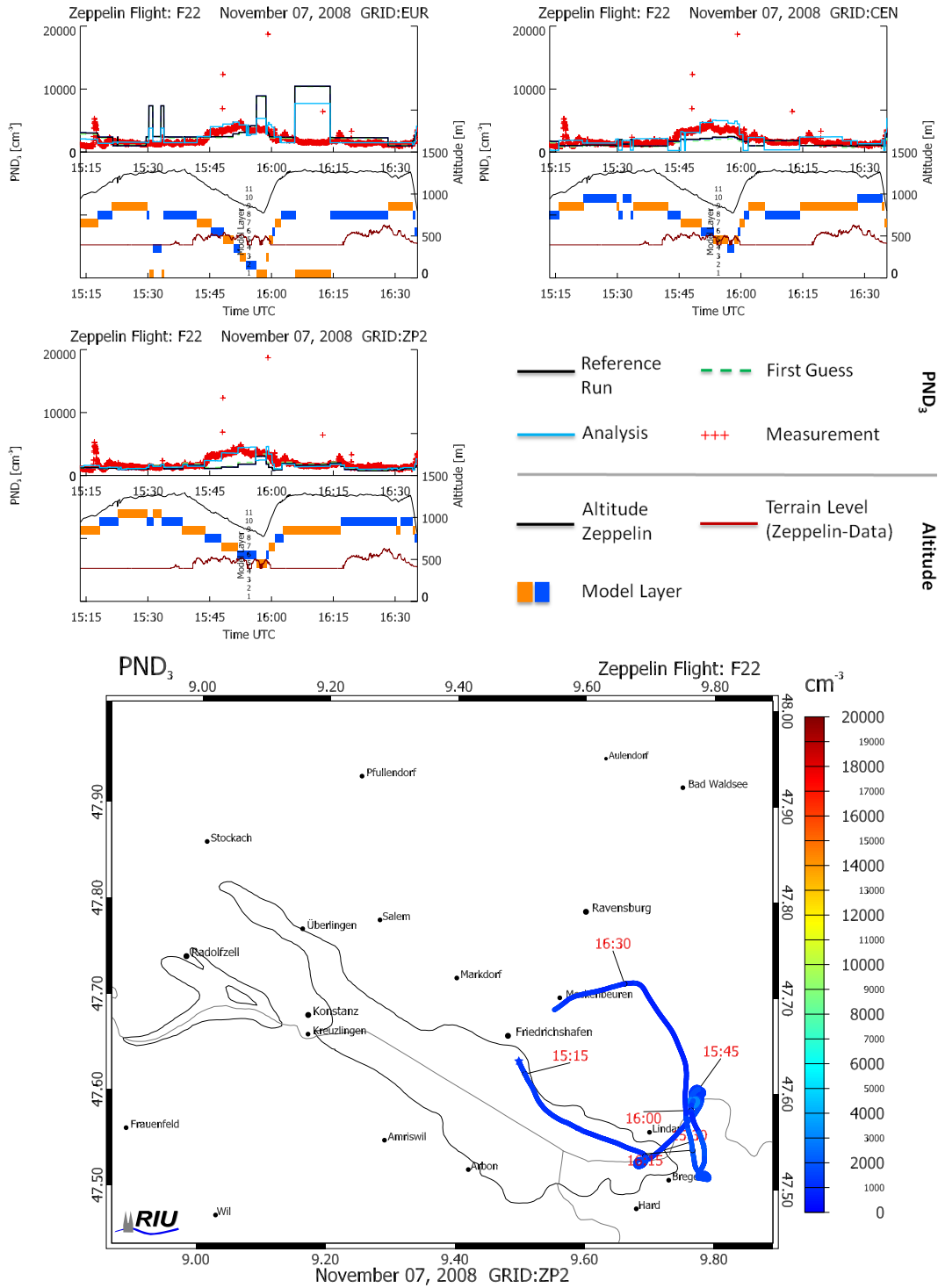


Figure C.7: Particle Number Densities  $PND_3$  of flight F20 assimilated on November 5, 2008, on the different domains EUR (top left), CEN (top right), ZP2 (center left), and flight track with ZP2  $PND_3$  (bottom).



**Figure C.8:** Particle Number Densities  $PND_3$  of flight F21 assimilated on November 7, 2008, on the different domains EUR (top left), CEN (top right), ZP2 (center left), and flight track with ZP2  $PND_3$  (bottom).



**Figure C.9:** Particle Number Densities  $PND_3$  of flight F22 assimilated on November 7, 2008, on the different domains EUR (top left), CEN (top right), ZP2 (center left), and flight track with ZP2  $PND_3$  (bottom).

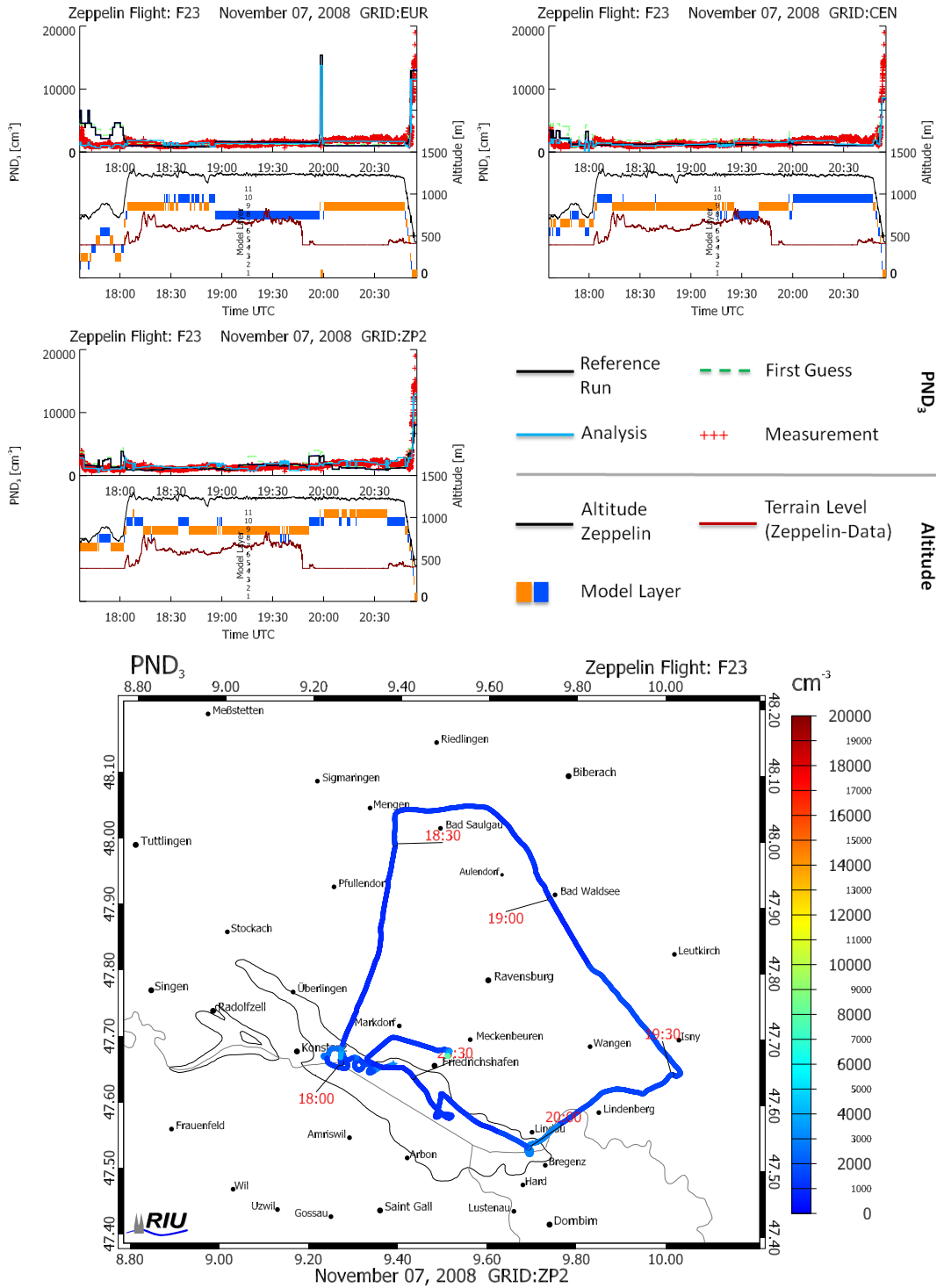


**Figure C.10:** Particle Number Densities  $PND_3$  of flight F23 assimilated on November 7, 2008, on the different domains EUR (top left), CEN (top right), ZP2 (center left), and flight track with ZP2  $PND_3$  (bottom).



---

## Bibliography

---

- Ackermann, I. J.**, *MADE: Entwicklung und Anwendung eines Aerosol-Dynamikmodells für dreidimensionale Chemie-Transport-Simulationen in der Troposphäre*, Ph.D. Thesis, Institut für Geophysik und Meteorologie der Universität zu Köln, 1997.
- Ackermann, I. J., H. Hass, M. Memmesheimer, A. Ebel, F. S. Binkowski and U. Shankar**, Modal aerosol dynamics model for Europe: Development and first applications, *Atmos. Environ.*, *32*, 2981–2999, 1998.
- Arakawa, A. and V. R. Lamb**, Computational design for the basic dynamical processes of UCLA general circulation model, *Meth. Comp. Phys.*, *17*, 174–264, 1977.
- Benedetti, A., J.-J. Mcrette, O. Boucher, A. Dethof, R. J. Engelen, M. Fisher, H. Flentje, N. Huneus, L. Jones, J. W. Kaiser, S. Kinne, A. Mangold, M. Razinger, A. J. Simmons and M. Suttie**, Aerosol analysis and forecast in the European Centre for Medium-Range Weather Forecasts Integrated Forecast System: 2. data assimilation, *J. Geophys. Res.*, *114*, (D13205), 2009.
- Binkowski, F. S. and U. Shankar**, The regional particulate matter model 1. Model description and preliminary results, *J. Geophys. Res.*, *100*, (D12), 26191–26209, 1995.
- Bott, A.**, A positive definite advection scheme obtained by nonlinear renormalization of the advective fluxes, *Month. Weath. Rev.*, *117*, (5), 1006–1015, 1989.

- Brimblecombe, P. and R. L. Maynard**, *The urban atmosphere - Air pollution reviews*, vol 1, Imperial College Press, 2001.
- Chang, J. S., R. A. Brost, I. S. A. Isaksen, S. Madronich, P. Middleton, W. R. Stockwell and C. J. Walcek**, A three-dimensional Eulerian acid deposition model: physical concepts and formulation, *J. Geophys. Res.*, *92*, (14), 618–700, 1987.
- Clegg, S. L., K. S. Pitzer and P. Brimblecombe**, Thermodynamics of multicomponent, miscible, ionic-solutions. 2. Mixtures including unsymmetrical electrolytes, *J. Phys. Chem.*, *96*, (23), 9470–9479, 1992.
- Collins, W., P. Rasch, B. Eaton, B. Khattatov, J.-F. Lamarque, and C. Zender**, Simulating aerosols using a chemical transport model with assimilation of satellite aerosol retrievals: Methodology for INDOEX, *J. Geophys. Res.*, *106*, (D7), 7313–7336, 2001.
- Daley, R.**, *Atmospheric Data Analysis*, Cambridge Univ. Press, 1991.
- Ebel, A., H. Hass, H. J. Jakobs and M. Memmesheimer**, Complex chemical transport modelling, its evaluation and application to air pollution episodes, in *Air Pollution*, edited by P. Z. et al., Elsevier, 1993.
- Ebel, A., H. Elbern, H. Feldmann, H. J. Jakobs, C. Kessler, M. Memmesheimer, A. Oberreuter and G. Piekorz**, *Air pollution studies with the EURAD model system (3)*, vol 120, Mitteilungen aus dem Institut für Geophysik und Meteorologie der Universität zu Köln, 1997.
- Elbern, H. and H. Schmidt**, A four-dimensional variational chemistry data assimilation scheme for Eulerian chemistry transport modeling, *J. Geophys. Res.*, *104*, (D15), 18,583–18,598, 1999.
- Elbern, H. and H. Schmidt**, Ozone episode analysis by four-dimensional variational chemistry data assimilation, *J. Geophys. Res.*, *D4*, (106), 3569 – 3590, 2001.
- Elbern, H. and A. Strunk**, Chemical weather analysis optimisation with emission impact estimation using nested four-dimensional variational chemistry data assimilation, in *Air, Water and Soil Quality Modelling for Risk and Impact Assessment*, edited by A. Ebel and T. Davitashvili, 315–325, Springer, 2007.
- Elbern, H., H. Schmidt and A. Ebel**, Variational data assimilation for tropospheric chemistry modeling, *J. Geophys. Res.*, *102*, (D13), 15,967–15,985, 1997.

- Elbern, H., H. Schmidt, O. Talagrand and A. Ebel**, 4D-variational data assimilation with an adjoint air quality model for emission analysis, *Environ. Model. and Software*, *15*, 539–548, 2000.
- Elbern, H., A. Strunk, H. Schmidt and O. Talagrand**, Emission rate and chemical state estimation by 4-dimensional variational inversion, *Atmos. Chem. Phys.*, *7*, 1–59, 2007.
- European Commission**, CAFE - Clean Air For Europe, technical report, EC, 2005.
- Evensen, G.**, Sequential data assimilation with a nonlinear quasi-geostrophic model using monte-carlo methods to forecast error statistics, *J. Geophys. Res.*, *99*, (C5), 10143–10162, 1994.
- Friese, E. and A. Ebel**, Temperature dependent thermodynamic model of the system  $\text{H}^+$  -  $\text{NH}_4^+$  -  $\text{Na}^+$  -  $\text{SO}_4^{2-}$  -  $\text{NO}_3^-$  -  $\text{Cl}^-$  -  $\text{H}_2\text{O}$ , *J. Phys. Chem. A*, *114*, 11595–11631, 2010.
- Geiger, H., I. Barnes, I. Bejan, T. Benter and M. Spittler**, The tropospheric degradation of isoprene: an updated module for the regional atmospheric chemistry mechanism, *Atmos. Environ.*, *37*, (11), 1503–1519, 2003.
- Grell, G. A., J. Dudhia and D. R. Stauffer**, A description of the fifth-generation Penn State/NCAR mesoscale model MM5, technical report, National Center for Atmospheric Research, 1994.
- Hass, H.**, *Description of the EURAD Chemistry-Transport-Model version2 (CTM2)*, vol 83, Mitteilungen aus dem Institut für Geophysik und Meteorologie der Universität zu Köln, 1991.
- Hass, H., H. J. Jakobs and M. Memmesheimer**, Analysis of a regional model (EURAD) near surface gas concentration predictions using observations from networks, *Met. Atmos. Phys.*, *57*, 173–200, 1995.
- Henze, D., J. H. Seinfeld, W. Liao, A. Sandu and G. R. Carmichael**, Inverse modeling of aerosol dynamics: Condensational growth, *J. Geophys. Res.*, *109*, (D14201), 2004.
- Holzer-Popp, T.**, personal communication, 2011.
- Holzer-Popp, T., M. Schroedter and G. Gesell**, Retrieving aerosol optical depth and type in the boundary layer over land and ocean from simultaneous GOME spectrometer and ATSR-2 radiometer measurements - 2. Case study application and validation, *J. Geophys. Res.*, *107*, (D24), 2002a.

- Holzer-Popp, T., M. Schroedter and G. Gesell**, Retrieving aerosol optical depth and type in the boundary layer over land and ocean from simultaneous GOME spectrometer and ATSR-2 radiometer measurements, 1, Method description, *J. Geophys. Res.*, *107*, (D21), 4578, 2002b.
- Holzer-Popp, T., M. Schroedter-Homscheidt, H. Breitkreuz, D. Martynenko and L. Klueser**, Improvements of synergetic aerosol retrieval for ENVISAT, *Atmos. Chem. Phys.*, *8*, (24), 7651–7672, 2008.
- Intergovernmental Panel on Climate Change**, Climate change 2001, technical report, IPCC, 2001.
- Jacobson, M. Z.**, Numerical techniques to solve condensational and dissolutional growth equations when growth is coupled to reversible aqueous reactions, *Aerosol Sci. Technol.*, *27*, 491–498, 1997.
- Jakobs, H. J., H. Feldmann, H. Hass and M. Memmesheimer**, The use of nested models for air pollution studies: An application of the EURAD model to a SANA episode, *J. Appl. Meteor.*, *34*, (6), 1301–1319, 1995.
- Kahnert, M.**, On the observability of chemical and physical aerosol properties by optical observations: Inverse modelling with variational data assimilation, *Tellus*, *61*, (5), 747–755, 2009.
- Kalnay, E.**, *Atmospheric Modeling, Data Assimilation and Predictability*, Cambridge Univ. Press, 2003.
- Kim, Y. P., J. H. Seinfeld and P. Saxena**, Atmospheric gas–aerosol equilibrium I. Thermodynamic model, *Aerosol Sci. Technol.*, *19*, 157–181, 1993.
- Kulmala, M., A. Laaksonen and L. Prijola**, Parametrizations for sulfuric acid/water nucleation rates, *J. Geophys. Res.*, *103*, (D7), 8301–8307, 1998.
- Lahoz, W. A., B. Khattatov and R. Menard**, *Data Assimilation: Making Sense of Observations*, Springer, Berlin, 2010.
- Liu, D. C. and J. Nocedal**, On the limited memory BFGS method for large scale optimization, *Math. Programming*, *45*, 503–528, 1989.
- Lorenc, A. C.**, Analysis methods for numerical weather prediction, *Q. J. R. Meteorol. Soc.*, *112*, 1177–1194, 1986.

- McRae, G. J., W. R. Goodin and J. H. Seinfeld**, Numerical solution of the atmospheric diffusion equation for chemically reacting flows, *J. Comp. Phys.*, *45*, 1–42, 1982.
- Memmesheimer, M., J. Tippke, A. Ebel, H. Hass, H. J. Jakobs and M. Laube**, On the use of EMEP emission inventories for European scale air pollution modelling with the EURAD model, in *Proceedings of the EMEP workshop on photooxidant modelling for long range transport in relation to abatement strategies*, edited by J. Pankrath, 307–324, UBA, Berlin, 1991.
- Memmesheimer, M., E. Friese, A. Ebel, H. J. Jakobs, H. Feldmann, C. Kessler and G. Piekorz**, Long-term simulations of particulate matter in Europe on different scales using sequential nesting of a regional model, *Int. J. Environm. and Pollution*, *22*, (1-2), 108–132, 2004.
- Nieradzik, L. P.**, Application of a high dimensional model representation on the atmospheric aerosol module MADE of the EURAD-CTM, Diploma Thesis, Institut für Geophysik und Meteorologie der Universität zu Köln, 2005.
- Pagowski, M., G. A. Grell, S. A. McKeen, S. E. Peckham and D. Devenyi**, Three-dimensional variational data assimilation of ozone and fine particulate matter observations: some results using the Weather Research and Forecasting - Chemistry model and Grid-point Statistical Interpolation, *Q. J. R. Meteorol. Soc.*, *136*, (653, Part b), 2013–2024, 2010.
- Parrish, D. and J. Derber**, The national meteorological centre’s spectral statistical-interpolation analysis system, *Month. Weath. Rev.*, *120*, 1747–1763, 1992.
- Rabier, F., H. Jarvinen, E. Klinker, J. F. Mahfouf and A. Simmons**, The ecmwf operational implementation of four-dimensional variational assimilation. i: Experimental results with simplified physics, *Q. J. R. Meteorol. Soc.*, *126*, (564), 1143–1170, 2000.
- Rabitz, H. and O. Alis**, General foundations of high-dimensional model representations, *J. Math. Chem.*, *25*, (2-3), 197–233, 1999.
- Rabitz, H., O. Alis, J. Shorter and K. Shim**, Efficient input-output model representations, *Comp. Phys. Comm.*, *117*, (1-2), 11–20, 1999.
- Sandu, A., W. Liao, G. R. Carmichael, D. K. Henze and J. H. Seinfeld**, Inverse modeling of aerosol dynamics using adjoints: Theoretical and numerical considerations, *Aerosol Sci. Technol.*, *39*, (8), 677–694, 2005.

- Saxena, P., A. B. Hudischewskyj and C. Seigneur**, A comparative study of equilibrium approaches to the chemical characterization of secondary aerosols, *Atmos. Environ.*, *20*, 1471–1483, 1986.
- Schell, B.**, Zu den Rand- und Anfangswertbedingungen des EURAD Chemie-Transport-Modells Version2 (CTM2): Erstellung eines Szenarios auf der Basis von Messdaten, Master Thesis, Institut für Geophysik und Meteorologie der Universität zu Köln, 1996.
- Schell, B., I. J. Ackermann, H. Hass and A. Ebel**, SORGAM — a secondary organic aerosol module for comprehensive air quality models, in *Proceedings of EUROTRAC Symposium 2000*, Springer, 2001.
- Schutgens, N. A. J., T. Miyoshi, T. Takemura and T. Nakajima**, Applying an ensemble Kalman filter to the assimilation of AERONET observations in a global aerosol transport model, *Atmos. Chem. Phys.*, *10*, (5), 2561–2576, 2010.
- Seinfeld, J. H. and S. N. Pandis**, *Atmospheric chemistry and physics*, Wiley-Interscience, 1998.
- Shorter, J., P. Ip and H. Rabitz**, An efficient chemical kinetics solver using high dimensional model representation, *J. Phys. Chem., A* *103*, (36), 7192–7198, 1999.
- Shorter, J., P. Ip and H. Rabitz**, Radiation transport simulations by means of a fully equivalent operational model, *Geophys. Res. Lett.*, *27*, (21), 3485–3488, 2000.
- Stockwell, W. R., F. Kirchner, M. Kuhn and S. Seefeld**, A new mechanism for regional atmospheric chemistry modeling, *J. Geophys. Res.*, *102*, (D12), 25847–25879, 1997.
- Strunk, A.**, *Tropospheric Chemical State Estimation by Four-Dimensional Variational Data Assimilation on Nested Grids*, Ph.D. Thesis, Institut für Geophysik und Meteorologie der Universität zu Köln, 2006.
- Talagrand, O.**, Assimilation of observations, an introduction, *J. Meteor. Soc. Japan*, *75*, (1B), 191–209, 1997.
- Weaver, A. and P. Courtier**, Correlation modelling on the sphere using a generalized diffusion equation, *Q. J. R. Meteorol. Soc.*, *127*, 1815–1846, 2001.

- 
- Whitby, K. T.**, The physical characteristics of sulfur aerosols, *Atmos. Environ.*, *12*, 135–159, 1978.



---

## Acknowledgements

---

First of all, I want to express my gratitude to Prof. Dr. Dr. h.c. Adolf Ebel who gave me the opportunity to write the thesis at hand in the friendly environment at RIU. He has always been a good advisor on things concerning work and life.

I kindly thank Prof. Dr. Andreas Wahner for agreeing to act as a referee for this thesis.

I especially want to thank Dr. Hendrik Elbern for a lot of fruitful discussions, helpful advice, and good ideas. He always had a useful suggestion when I was struggling with a problem. His wide knowledge on the field of data assimilation was a great support for me.

For software and discussion on the SYNAER retrieval and its radiative transfer model I want to extend my thanks to Thomas Holzer-Popp and Marion Schrödter-Homscheid at DLR-DFD in Oberpfaffenhofen.

I am very grateful to Elmar Friese, Jörg Schwinger, and Achim Strunk for the many discussions about data assimilation, forward modelling, programming hinds, the MM5, and/or aerosol chemistry. Without you guys this would have lasted twice as long!!!

I also want to thank Georg Piekorz who has taken care of the system at RIU. He did everything to keep it running and he always made concessions on special technical desires.

A large part of the simulations were conducted on JUCEDA which is operated at the ZAM in Jülich. Special thanks to Peter Niessen for solving problems on the short-way.

Many thanks to the various proof-readers of this thesis, be it only two pages: Hendrik Elbern, Elmar Friese, Nadine Goris, Michael Memmesheimer, Andrea Pauly, Jörg Schwinger, Annika Steuer, and Achim Strunk.

In addition to those mentioned above I want to thank all my colleagues who made this time an enjoyable time. Thank you!

The data that has been used in this thesis was provided by Thomas Holzer-Popp (DLR-DFD), Thomas Mentel (Research Centre Jülich), the EEA, and various national environmental agencies that shall be acknowledged herewith.

Finally, I want to sincerely thank Andrea Pauly for enduring the ups and, especially, the downs during this era, my parents for being patient and for believing in me, and all of my friends who I might have neglected sometimes. Thank you very much!

This work was funded by the German Science Foundation (DFG) under grant EL 238/1-1 and EL 238/1-2. This support is gratefully acknowledged.

## Erklärung

Ich versichere, dass ich die von mir vorgelegte Dissertation selbständig angefertigt, die benutzten Quellen und Hilfsmittel vollständig angegeben und die Stellen der Arbeit – einschließlich Tabellen, Karten und Abbildungen –, die anderen Werken im Wortlaut oder dem Sinn nach entnommen sind, in jedem Einzelfall als Entlehnung kenntlich gemacht habe; dass diese Dissertation noch keiner anderen Fakultät oder Universität zur Prüfung vorgelegen hat; dass sie –abgesehen von unten angegebenen Teilpublikationen– noch nicht veröffentlicht worden ist sowie, dass ich eine solche Veröffentlichung vor Abschluss des Promotionsverfahrens nicht vornehmen werde. Die Bestimmungen der Promotionsordnung sind mir bekannt. Die von mir vorgelegte Dissertation ist von Prof. Dr. Dr. h.c. A. Ebel betreut worden.

## Teilpublikationen

**Elbern, H., A. Strunk, E. Friese, L. Nieradzic**, Assessment of Source-Receptor Relations by Inverse Modelling and Chemical Data Assimilation, in *Persistent Pollution - Past, Present and Future*, M. Quante, R. Ebinghaus, G. Flöser (Eds.), Springer, 2011

**Elbern, H., A. Strunk, L. Nieradzic**, Data assimilation, in *The remote sensing of tropospheric composition from space*, J. Burrows, U. Platt, P. Borrell (Eds.), Springer, 2010

**Strunk, A., A. Ebel, H. Elbern, E. Friese, N. Goris und L. Nieradzic**, Four-dimensional Variational Assimilation of Atmospheric Chemical Data – Application to Regional Modelling of Air Quality, in *Large-Scale Scientific Computing: 7th International Conference*, I. Lirkov, S. Margenov, J. Wasniewski (Hrsg.), 4.-8. Juni 2009, Sozopol, Bulgarien, ISBN 978-3-642-12534-8, Springer 2010

**Elbern, E., A. Strunk, E. Friese, N. Goris, K. Kasradze und L. Nieradzic**, IMACCO: Inverse Modelling of the Atmospheric Chemical Composition, in *NIC Symposium 2010*, G. Münster, D. Wolf, M. Kremer (Hrsg.), 24.-25. Februar 2010, Jülich, Germany, IAS Series Volume 3, Jülich, 2010

**Elbern, H., A. Strunk, L. Nieradzik**, Inverse modelling and combined state-source estimation for chemical weather, in *Data Assimilation: Making sense of observations*, Springer, W. Lahoz, B. Khattatov, R. Menard (Eds.), invited, 2010

**Elbern, H., A. Strunk, L. Nieradzik, E. Friese**, Chemical Data Assimilation with Multiscale Emission Inversion, *Proceedings of the 5th WMO Symposium on Data Assimilation*, Melbourne, 2009

**Nieradzik, L. and H. Elbern**, Variational assimilation of combined satellite retrieved and in situ aerosol data in an advanced chemistry transport model, *Proceedings of the ESA Atmospheric Science Conference*, Frascati, ESRIN, 2006